INFORMATION TO USERS

This manuscript has been reproduced from the microfilm master. UMI films the text directly from the original or copy submitted. Thus, some thesis and dissertation copies are in typewriter face, while others may be from any type of computer printer.

The quality of this reproduction is dependent upon the quality of the copy submitted. Broken or indistinct print, colored or poor quality illustrations and photographs, print bleedthrough, substandard margins, and improper alignment can adversely affect reproduction.

In the unlikely event that the author did not send UMI a complete manuscript and there are missing pages, these will be noted. Also, if unauthorized copyright material had to be removed, a note will indicate the deletion.

Oversize materials (e.g., maps, drawings, charts) are reproduced by sectioning the original, beginning at the upper left-hand corner and continuing from left to right in equal sections with small overlaps.

Photographs included in the original manuscript have been reproduced xerographically in this copy. Higher quality 6" x 9" black and white photographic prints are available for any photographs or illustrations appearing in this copy for an additional charge. Contact UMI directly to order.

ProQuest Information and Learning
300 North Zeeb Road, Ann Arbor, MI 48106-1346 USA
800-521-0600

INNER-SHELL ELECTRON ENERGY LOSS SPECTROSCOPY

AND

GENERALIZED OSCILLATOR STRENGTHS AT

HIGH MOMENTUM TRANSFER

By

IULIA GABRIELA EUSTATIU, M. Sc.

A Thesis

Submitted to the School of Graduate Studies

in Partial Fulfillment of the Requirements

for the Degree

Doctor of Philosophy

McMaster University

March 2000

Spectroscopy and Oscillator Strengths at High Momentum Transfer

To my parents,

for who I am, for what I will be.

DOCTOR OF PHILOSOPHY (1999) **McMaster University**

(Chemical Physics) **Hamilton, Ontario**

TITLE: Inner-Shell Electron Energy Loss Spectroscopy and Generalized Oscillator Strengths at High Momentum Transfer

AUTHOR: Iulia Gabriela Eustatiu, M. Sc. (Université Laval)

SUPERVISOR: Professor Adam P. Hitchcock, Ph. D, F.C.I.C.

NUMBER OF PAGES: xvii, 196.

Abstract

Detailed information about the energies of the electronically excited and ionized states of atoms and molecules is of central importance to the understanding of the interaction of energetic radiation with matter. Such data permits a more complete understanding of various processes taking place in physics, chemistry or biology, with important areas of application including electron and X-ray microscopy, space physics and chemistry or any other area where energetic radiation is used.

This work documents the improvements and performance of a variable scattering angle energy loss spectrometer used to investigate inner-shell electronic spectroscopy of gases and to map generalized oscillator strengths. Wide ranges of impact energy and scattering angle are used to study both electric dipole and non-dipole transitions. New spectroscopic studies include: (i) the observation of the non-dipole "B-state" in SF_6 S $2p$ edge at very high scattering angle (62°) and at 1550 eV impact energy, where it dominates the spectrum; (ii) the first experimental observation of the C $1s \rightarrow \sigma_g^*$ transition in CO_2. Generalized Oscillator Strength (GOS) profiles were mapped systematically for a collection of molecules: in SF_6, the GOS for S $2p$ and S $2s$ were extended up to very high momentum transfer, while the GOS for F $1s$ was mapped here for the first time. GOS curves were also obtained for all edges in CO_2, COS and CS_2, some of them revealing their shapes for the first time. Where available, the results were compared to theoretical calculations. This work greatly extends previous reported studies of GOS for inner-shell excitation.

Acknowledgements

I would like to express my most sincere gratitude and appreciation to my supervisor, Dr. Adam Hitchcock for his knowledge, constant interest and guidance, support and belief in me. His unfailing encouragement, insights and supervision made this thesis, and all the related projects, possible.

I would also wish to thank Dr. Tolek Tyliszczak for his infinite patience in answering questions ranging from technical and scientific advice to any car-related topics.

I also wish to show appreciation to the members of my supervisory committee, Dr. Harold Haugen, Dr. Joseph Laposa and Dr. David Venus for great support and guidance as well as encouragement to keep the Chemical Physics program alive.

Special thanks are also addressed to all the lab people, Dr. Cassia Turci, Dr. Stephen Urquhart, Peter Brodersen, Jeff Aubry, John Lehmann, Laura Ennis, Dr. John Neville, Robert Lessard and more recently Cynthia Morin, Eiman Al-Hassan and Dr. Ivo Koprinarov for all the good laughs and friendship.

Special thanks are due to my parents; their presence in person or in mind was always a source of great support. I could not end the acknowledgments without mentioning my husband Adrian who, with constant love, enthusiasm, faith and patience over this sometimes difficult period, was my strongest supporter.

THESIS OUTLINE

Figure Captions

List of Tables

List of Abbreviations and Symbols

β	constant
c	Speed of Light in Vacuum
DCS	Differential Cross Section
$E_{\perp}$	Normal Component to the Electric Field **E**
$E_{\parallel}$	Parallel Component to the Electric Field **E**
E_0	Impact Energy
E_n	Excitation Energy
E_l	Residual Energy
EELS	Electron Energy-Loss Spectroscopy
FBA	First Born Approximation
Γ	Natural Linewidth
GOS	Generalized Oscillator Strength
$\hbar$	Planck's Constant
IP	Ionization Potential
ISEELS	Inner Shell Electron Energy Loss Spectroscopy
K	Momentum Transfer
k_0	Momentum of Incident Electron
k_l	Momentum of Scattered Electron
McVAHRES	McMaster Variable Angle High Resolution Electron Spectrometer
MO	Molecular Orbital
OOS	Optical Oscillator Strength
PES	Photoelectron Spectroscopy
θ	Scattering Angle
τ	Excited State's Lifetime
v	Particle's Velocity
VUV	Vacuum Ultraviolet
XAS	X-ray Absorption Spectroscopy
XPS	X-ray Photoelectron Spectroscopy

Chapter 1

INTRODUCTION

This chapter presents a general introduction to Electron Energy Loss Spectroscopy (EELS) and to Inner-Shell Electron Excitation. Through the virtual photon model, an "Electrons versus Photons" comparison is made. The concept of Generalized Oscillator Strength (GOS) and its importance and a few practical applications sets the stage for this thesis. An outline of the thesis chapters closes this first chapter.

Accurate information for representative species over the entire spectrum of energies is essential for the development and testing of new quantum mechanical procedures for calculating electronic state energies and the associated cross sections for the processes involved. Furthermore, adequate answers to questions about the effects of radiation can only be given if the associated cross sections are known. Such information not only permits a safer society, but also facilitates the development and use of radiation for worthwhile humanitarian purposes in a needy world.

1.1. Introduction to Electron Energy Loss Spectroscopy (EELS)

Electron spectroscopy is a generic name given to a set of techniques based on the analysis of velocities of electrons following a collision between an electron as the impacting particle and an atom, molecule or solid as the target. It deals with changes in the distribution of electrons within a molecule. Thus, when electrons enter a molecular field, they interact with the molecule through electrostatic (Coulomb) forces. As a result, some electrons are scattered; the direction of their momentum is changed and in many cases they transfer an appreciable amount of energy to the molecule.

The technique of electron-impact energy loss spectroscopy is based on the fact that excitation from an occupied molecular level to an unoccupied level, separated by energy E_n, may occur and is necessarily accompanied by an energy loss in the energy of the incident electron.

It is convenient to divide the scattering into two broad categories: *elastic* and *inelastic*. *Elastic scattering* is by definition the process where no change is observed in the kinetic energy of the scattered electron after the collision. By contrast, *inelastic scattering* defines a process where both the incident electron and the target - atoms or molecules - trade energy and momentum. This type of collision is accompanied by a change in the internal state of the colliding entities, which may consist in the excitation, or ionization of atoms or molecules, the excitation or disintegration of nuclei, etc.

In EELS an incident beam of monoenergetic electrons of energy E_0, produced by acceleration from an electron source through a potential difference, is passed through a sample. The electrons scatter elastically and inelastically after the collision with an atom

or a molecule in a field-free region. The energy spectrum of the outgoing scattered electrons is measured. As an alternative, the energy of the incident beam could be varied, while the counting rate for scattered electrons of a particular energy is monitored. Either way an energy loss spectrum results with a peak at each allowed energy.

The basic electron energy loss process can be represented as:

$$e^-(E_0) + M \rightarrow M^*(E_n) + e^-(E_1) \tag{1.1}$$

where e^- is the colliding electron of initial energy E_0 and residual energy E_1 after collision with the target species M. M represents the initial state of the target and M^* represents the target after a transition to an excited final state occurred as a result of interaction with the incident electron.

Momentum is conserved:

$$\overrightarrow{K} = \overrightarrow{k_0} - \overrightarrow{k_1} \tag{1.2a}$$

$$K^2 = |\overrightarrow{K}|^2 = |\overrightarrow{k_0} - \overrightarrow{k_1}|^2 = k_0^2 + k_1^2 - 2k_0k_1\cos\theta \tag{1.2b}$$

where $\overrightarrow{k_0}$ is the wavevector of the incident electron with momentum $\hbar|k_0|$, $\overrightarrow{k_1}$ is the wavevector of the outgoing electron scattered through an angle θ with momentum $\hbar|k_1|$, and $\hbar\overrightarrow{K}$ is the resultant momentum transfer (fig. 1.1).

The technique has the great advantage of allowing dipole forbidden and/or spin forbidden transitions under conditions of significant momentum transfer, in contrast to one photon photoabsorption, which is subject to *dipole selection rules*.

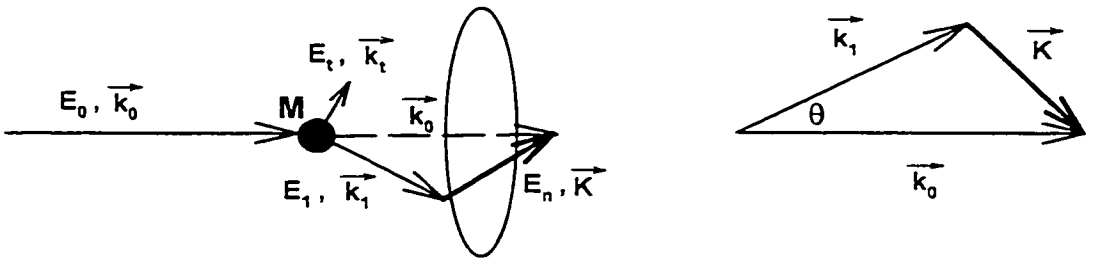

Figure 1.1 Schematic diagram of scattering kinematics in a typical EELS process involving nonzero momentum transfer $\hbar K$ to a molecular target M, where t stands for the translation process – see chapter 2. (after [YDM&93])

The characteristic concept describing a collision of two particles is the differential *cross section*. In general, the cross section for a certain type of event in a given collision is equal to the number of events of this type per unit time per unit flux of particles incident on target. The cross section is a fundamental property of a molecule which is related to the molecular wavefunctions for the two states between which a transition is induced [BH81]. Thus, cross sections have contributions that arise from purely kinematic quantities such as the impact energy of the electron beam and others that depend only on the properties of the molecule.

Not more than 25 years ago analysis of the scientific literature indicated that very little quantitative information (i.e., cross sections or dipole oscillator strengths) existed for valence-shell (E_n < 50 eV) electronic processes, while information about energy levels, let alone cross sections, for molecular inner-shell processes (E_n > 50 eV) was

practically non-existent. Today the situation has much improved, as the influx of new data is a direct result of the increasing accessibility and use of novel experimental techniques involving either tunable synchrotron radiation or the dipole "*virtual photon*" – fast electron – source. It is in this context that the work presented by this thesis brings new spectroscopic data and an important collection of oscillator strength profiles for selected molecules.

Historically, the energy loss of electrons passing through gases was studied as early as 1914 by Franck and Hertz [FH14]. They first confirmed the energy quantization in excitation processes by inelastic electron scattering on mercury atoms. These experiments are often used in physics textbooks to explain the different nature of electron versus photon interaction with atoms. In 1930 Bethe [B30] showed that under certain conditions the electron energy-loss cross section could be directly related to the X-ray or optical absorption cross section, where the energy loss of the electron during the collision event is equivalent to the photon energy. This equivalence is easy to understand since energy loss in one case and photoabsorption in the other furnish the energy required to excite an atom from the initial state to the final state. If the energy loss of the electron during the collision event is small compared to its kinetic energy, the interaction between the electron and the atom can be treated in lowest order and a first-order perturbation approximation to the differential cross-section, called the *first Born approximation* (FBA), can be used, (see chapter 2 for details).

The further development of the EELS technique was relatively slow until the early 1960's when technical advances in the areas of vacuum and electrostatic electron

energy analyzers provided the basis for a rapid growth in all areas of electron spectroscopy.

1.2. Inner-Shell Electron Excitation

Although currently X-ray absorption spectroscopy (XAS) is the technique of choice for the study of inner shell excitation processes, the detailed understanding of such spectra is largely due to *inner shell electron energy loss spectroscopy* (ISEELS).

ISEELS of gases has been carried out for about twenty-five years with the goal of investigating the electronic structure of matter and electron-induced processes. One reason for the dominance of ISEELS in investigating molecules lies in the long-time unavailability of highly monochromatic, intense tunable photon radiation in the 250–1000 eV range. Another important reason is experimental easy accessibility of ISEELS since the spectrometers are relatively inexpensive and home-based. Furthermore, the energy resolution of ISEELS spectrometers is constant over the energy range, while the energy resolution of X-ray monochromators varies with the photon energy.

A major advantage of ISEELS relative to XAS is the capability of identifying non-electric dipole transitions via variable angle studies. The selection rules for inelastic electron scattering at high impact energy can be discussed in terms of momentum transfer dependent, generalized oscillator strength (GOS). Its relation to the measured differential cross section will be discussed in the next chapter. This type of experiment has the central stage of this thesis.

In a typical inelastic electron scattering process, the transfer of energy and momentum from the incident electron to the atomic or molecular target can be used to produce both dipole and non dipole excitations.

In conditions of small angle scattering and impact energies above 1 keV the ISEEL spectra are dominated by spin conserving, electric-dipole transitions. When the impact energy is reduced to values only fractionally larger than the threshold for the specific loss process, exchange between the incident and target electron can occur and thus, the spin of the molecule can change. A good spatial overlap of the core hole and the excited electron is needed to produce a sizeable exchange contribution to the state energy.

The features appearing in core excitation spectra arise from electronic transitions between the ground state and core excited states of a molecule, where a *state* is described by a wavefunction, a mathematical concept that contains information about the location and motion of all electrons in the molecule. At a fundamental level, any electronic transition is a process involving all electrons in a molecule, and the state picture is strictly correct. However, the one-electron picture is a convenient description, which is adequate for many core excitation transitions.

One-electron transitions are classified in terms of the character of the final electronic level, which includes "*valence excitations*" (i.e., core$\rightarrow\pi^*$ and core$\rightarrow\sigma^*$ transitions) and "*Rydberg transitions*" - *atomic like* features (core $\rightarrow$ Rydberg transitions). The dominant features of molecular core excitation spectra are resonant valence excitations, where a core electron is excited to an unoccupied valence level.

Resonant core excitations occur at energies relatively near the energy of the core ionization potential (IP).

Features that occur below the IP are referred to as *bound* or *discrete* resonances, while resonant features that occur above the IP are referred to as *unbound* or *shape* resonances. Double excitation processes also contribute weakly, typically in the first 20 eV of the core ionization continuum [H90].

Final state molecular orbitals are typically antibonding and these levels are referred to as π^* and σ^* molecular orbitals (e.g., C 1*s* $\rightarrow$ π^* transition). In general, π^* resonances are intense and narrow. The natural width of these resonances (in the absence of instrumental broadening) is determined by the lifetime of the core excited state and the vibrational motion of the molecule. Most core $\rightarrow$ σ^* transitions occur above the IP, although some core $\rightarrow$ σ^* states can occur below the IP [IMH&87]. Core $\rightarrow$ σ^* resonances that occur below and above the IP are attributed to different physical mechanisms. Thus, transitions to resonant states *below* the ionization potential can be described as transitions to unoccupied molecular orbitals. For transitions to states *above* the ionization potential the transition is viewed as a two step, one-electron processes: excitation from a core orbital to an unoccupied molecular orbital, followed by the emission of a photoelectron [T83].

In contrast to valence-shell excitation, the initial orbital for an inner-shell transition can usually be identified easily on an energetic basis since, for excitation energies larger than approximately 50 eV, the spectral structures associated with different types of inner-shell (core) levels are well separated. Below 50 eV, features arising from

promotions of different valence orbitals frequently overlap which can make spectral identification difficult.

The discrete structure observed in molecular inner-shell excitation spectra provides useful information about the virtual levels of the target. Coulomb, centrifugal or exchange barriers in the molecular potential [D72, DD75, DD76] diminish the intensity of transitions of Rydberg states and enhance those to valence-type core-excited states by excluding spatially extended orbitals and localizing compact orbitals.

There are also limitations to inner-shell excitation studies. When a core electron has been promoted, the resulting highly excited state decays rapidly and thus has a very short lifetime. According to the Heisenberg uncertainty principle, this lifetime is reflected in an uncertainty in the energy of such state which is given by:

$$\Gamma \geq \frac{\hbar}{\tau} \tag{1.3}$$

where Γ is the energy uncertainty (i.e., the natural linewidth) and τ is the lifetime of the excited state.

1.3. Electrons versus Photons

If one compares optical spectroscopy (i.e., visible, UV and vacuum-UV absorption spectroscopy) and electron spectroscopy, there are selection rules operating in optical spectroscopy which forbid certain transitions. These selection rules are less rigorous for electron impact, and by varying the incident energy and/or the scattering angle, it is possible to observe transitions not observed in optical spectroscopy. Thus,

when the incident electron is highly energetic (large E_0) and is scattered through a small angle, the momentum transferred to the target from the colliding electron is very small. The resulting interaction between this electron and the target is weak and the electric dipole process dominates. Under conditions where E_0 approaches the energy loss E_1 and/or the scattering angle becomes large ($>$ 10°), the momentum transferred to the target from the incident electron during the collision becomes larger. This leads to a relaxation of the electric dipole selection rules.

For photon and dipole-dominated energy loss transitions, the initial and final states of the target are coupled by the *electric dipole transition moment*, which reflects the reorganization of the molecular electronic charge distribution during a transition and defines the correct symmetry of the final state, and thus the selection rules necessary for a transition to occur. Therefore, optical selection rules are often referred to as *dipole* selection rules and the corresponding transitions are called *electric dipole allowed*. Thus, allowed transitions are those for which the *dipole transition matrix element* is non-vanishing. For example, an atomic transition where the electron starts in an *s* orbital (l = 0) and undergoes a transition to a *p* orbital (l = 1) is formally allowed optically. In the case of (non-diatomic) molecules where the straight forward angular momentum consideration is lost, the selection rules result from orbital symmetry considerations according to group theory.

Atomic transitions where the overall change in angular momentum is 0 or 2 are known as *quadrupole* transitions. Such transitions are *forbidden optically*, due to the fact that the electromagnetic field of the photons induces only dipole transition moments.

There are also higher order transitions, connected by octupole, etc. transitions moments that are also optically forbidden.

The absolute intensity of dipole-allowed transitions is conveniently expressed in terms of f_0, the *optical oscillator strength* (OOS). This quantity is related to the absorption coefficient and also to the cross section for absorption or emission of radiation.

If the impacting particles are photons, since a photon must be annihilated by the process of excitation, this will result in a *resonant* process ($h\nu = E_n$) (i.e., the photons are absorbed – complete loss of energy – or transmitted unabsorbed). On the other hand, the process of electron impact is *non-resonant* ($E_0 > E_n$) (i.e., energetic electrons are able to lose *any* amount of their energy while interacting with the target).

1.3.1. The *Virtual Photon* Model – Semi-classical Treatment

Consider a structureless charged particle of mass M, charge ze and velocity v passing at a distance b (impact parameter) from a molecule at a point P and separate the time dependence of the electric field vector $\vec{E}$ created by its motion, into two components, the normal ($\vec{E_\perp}$) and the parallel ($\vec{E_\parallel}$). **Figure 1.2** illustrates the process. The following derivation is based on that given by Christophourou [C71a].

Suppose that the particle passes closest to P at time $t = 0$. If we assume that the velocity of the particle is non-relativistic and that the impact parameter is large compared to the dimensions of the molecule, the collision is called "glancing", and the electric field at any time is essentially uniform throughout the molecule at P. The electric field

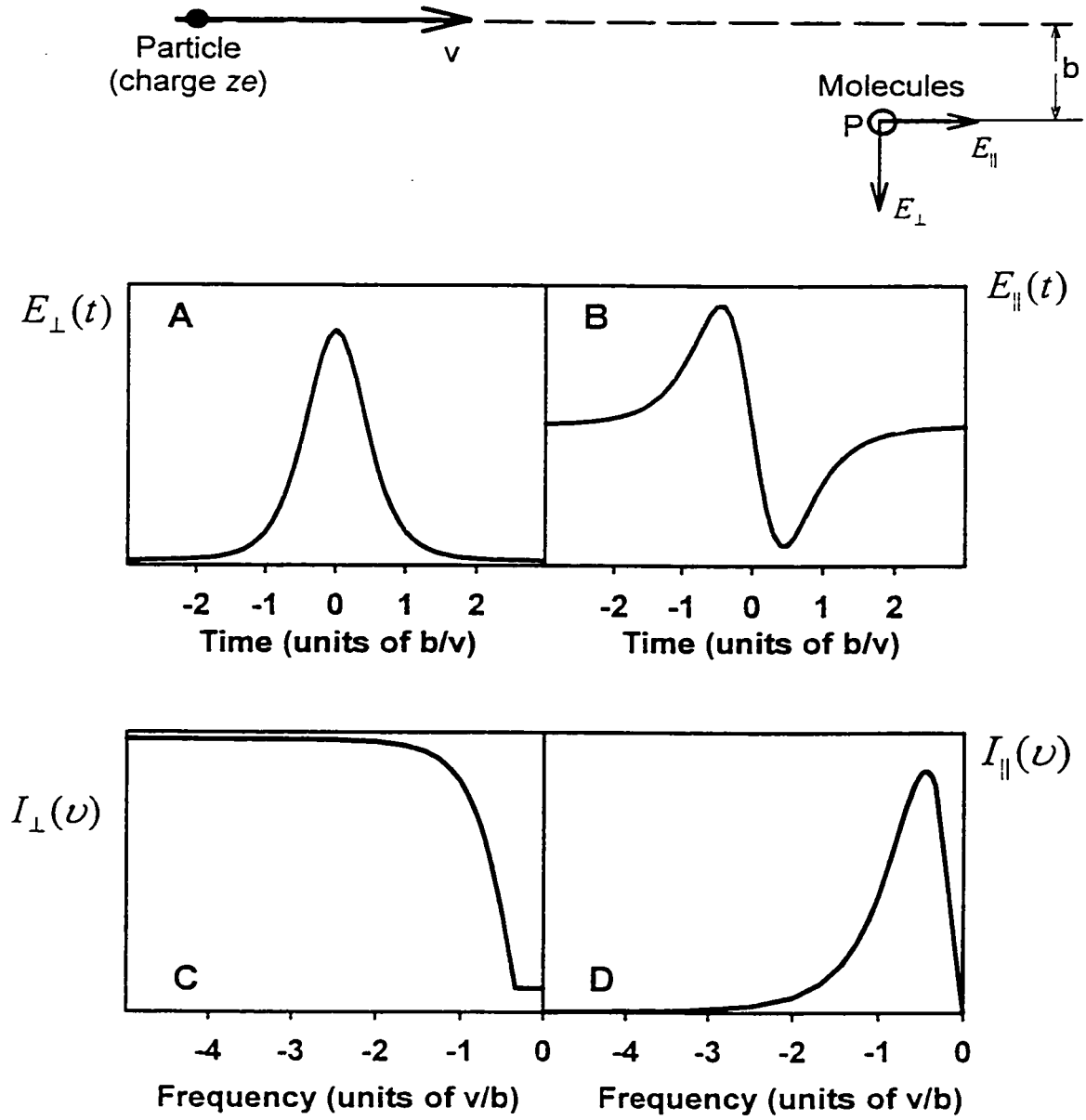

Fig. 1.2 A distant collision between a swiftly-moving charged particle and a molecule at point P; (A) and (B) variations of the two electric field intensity components during collision; (C) and (D) spectrum of "virtual photons". (after [C71a])

experienced by the molecule at P is independent of the mass of the particle M and is appreciable for only a short period of time. The two components of the electric field, perpendicular and along the direction of the charged particle are:

$$E_{\perp} = \frac{zeb}{\left(v^2 t^2 + b^2\right)^{3/2}} \tag{1.4a}$$

and

$$E_{\parallel} = \frac{ze v t}{\left(v^2 t^2 + b^2\right)^{3/2}} \tag{1.4b}$$

Because $\overline{E}_{\parallel}(t) = -\overline{E}_{\parallel}(-t)$ the only momentum change is that due to the $\overline{E}_{\perp}$ component. The time dependence of $\overline{E}_{\perp}$ and $\overline{E}_{\parallel}$ is shown in fig. 1.2 (A and B).

Either field component ($\overline{E}_{\parallel}$ or $\overline{E}_{\perp}$) can be represented mathematically as a unique sum of contributions (integrals), each of which is a purely harmonic function of time. Each of the individual contributions $E_{\omega}(t)$ is equivalent to the electric field experienced by the molecule when it is traversed by a light wave of frequency $\nu = \omega/2\pi$. Therefore, the effect of collision of a charged particle on the molecule is equivalent to that sustained by the molecule if it were traversed by a beam of photons, often referred to as "virtual photons". To find the frequencies of these "virtual photons" we take Fourier components of the $E_{\perp}(t)$

$$E_{\omega\perp} = \frac{1}{2\pi} \int_{-\infty}^{\infty} E_{\perp}(t) e^{i\omega t} dt \tag{1.5}$$

therefore,

$$E_{\omega\perp} = \frac{ze}{\pi b \vee}\left[\frac{\omega b}{\vee} K_1\left(\frac{\omega b}{\vee}\right)\right] \tag{1.6}$$

where $K_1(x)$ is a modified Bessel function of the second kind; $K_1(x) \rightarrow 1/x$ for $x \rightarrow 0$. Hence,

$$E_{\omega\perp} \cong \frac{ze}{\pi b \vee} \tag{1.7a}$$

for $\omega << v/b$, and

$$E_{\omega\perp} = 0 \tag{1.7b}$$

for $\omega >> v/b$.

The intensities $I(\nu)$ of the "virtual photons" corresponding to the field components $\overline{E}_\perp$ and $\overline{E}_\parallel$ are plotted in Figs. 1.2(D) and 1.2(E), respectively, as a function of the frequency multiplied by b/v. It is seen that for $I_\perp(\nu)$ the energy of the photons per unit frequency-interval is a constant from zero frequency up to about the "cut-off" frequency $\nu_{max} = v/b$ and it declines sharply to zero as ν approaches v/b. On the other hand, $I_\parallel(\nu)$ is less intense and has a peaked intensity distribution. Hence, $I(\nu) \cong I_\perp(\nu)$ is essentially constant thus the white light analogy is still maintained [C71a].

1.4. Generalized Oscillator Strength (GOS) Experiments

There are *two* general topics into which work in energy electron impact spectroscopy can be divided. The first is *spectroscopy*. In this application, the emphasis is mainly on the determination of spectral line positions as opposed to intensities. The second general area of application, *spectrometry*, has to do with the measurement of

precise spectroscopic *intensities* and their use to obtain information about the target system. Since the First Born Approximation (FBA) provides us with a simple direct connection with atomic and molecular properties of the target systems, perhaps it is this last area which best defines EELS relative to other areas of electron scattering spectroscopy.

The concept of oscillator strength was developed from the classical picture of the atom in which the electrons were considered to be in free oscillation at given frequencies about an equilibrium position with respect to the massive nucleus. The oscillator strength was defined as the number of electrons in free oscillation at a given frequency and was thus, considered to be related to the intensity of absorption at a given frequency. Subsequently, the quantum theory of atomic structure emerged, giving a description of the atom involving both bound (discrete) and continuum (ionized) states. A very large number of transitions can occur between these states – far more than the number of atomic electrons. Nevertheless, the historical oscillator strength terminology has been retained in assigning an absolute scale for the probability of transition between two energy states.

Optical Oscillator Strengths (OOS) have traditionally been measured by optical absorption. measurements that are restricted to those regions of the electromagnetic spectrum where suitable exciting photon sources are available. Thus, relatively few measurements have been made in the Vacuum Ultraviolet (VUV) and soft X-ray regions since sufficiently intense tunable (continuum) light sources have not generally been available, at least above 20 eV. It is now apparent that the electron storage rings supply

sufficiently intense continuum radiation to allow a wide range of such measurements to be made [BH81].

A growing number of quantitative fast-electron-impact experiments have been used in recent years as an alternative method of obtaining OOS. Using the Born approximation, Bethe [B30] laid the theoretical background to the Bethe-Born theory. This theory describes the response of a target species to fast electron impact in terms of momentum-transfer dependent GOS. This concept represents the cross section of the scattering process, which involves the kinematics of the electron before and after the collision, and the transition probability of the resulting excitation of the target. Under appropriate scattering conditions (i.e., within the FBA which is usually satisfied whenever E_0 is several times the energy loss), that part of the GOS expression representing the target electrons can be expanded in a form which includes contributions from dipole and higher order multipole transition matrix elements weighted by increasing powers of the momentum transfer as it will be shown in chapter 2. In the limit of zero momentum transfer, the GOS reduces to the OOS, which thus allows one to simulate photoabsorption using EELS. By increasing the momentum transfer, however, the contribution to the GOS from quadrupole, octupole and higher order non-dipole transition matrix elements becomes significant. In this manner, one can use EELS to access transitions that are forbidden optically based on consideration of angular momentum selection rules and the symmetries of the initial and final states.

Table 1.1 presents a summary of experimental GOS studies employing high

Table 1.1 Summary of experimental and theoretical GOS studies

Molecule	Edge	Method	E_0 (eV)	angle (°)	E_n (eV)	Reference
$CClF_3$	C 1*s*	E	2500	0.5-10	285-330	YL94
CCl_2F_2	C 1*s*	E	2500	0.5-10	285-330	YL94
CCl_3F	C 1*s*	E	2500	0.5-10	285-330	YL94
CF_4	C 1*s*	E	2500	0.5-10	285-330	YL94
COS	C 1*s*	E	1300	4-28	280-315	ETH&00
CO_2	C 1*s*	E,T	1290	2-14	260-380	BBS91
		T		0-15	290.7	MB93
		T	1290	2-14	291	FCM&96
		E	1300	4-36	285-330	ETH&99
CS_2	C 1*s*	E	1300	4-28	280-310	ETH&00
C_2H_2	C 1s	E,T	1290	2-18	280-292	MBB&94
$CClF_3$	Cl 2*p*,2*s*	E	2500	0.5-10	195-240	YL94
CCl_2F_2	Cl 2*p*,2*s*	E	2500	0.5-10	195-240	YL94
CCl_3F	Cl 2*p*,2*s*	E	2500	0.5-10	195-240	YL94
CCl_4	Cl 2*p*,2*s*	E	2500	0.5-10	195-240	YL94
SF_6	F 1*s*	E	1500	4-28	675-720	EFT&99
NO	N 1*s*	T	3400	2-20	400	RO85
		E			400	CFP&87
N_2	N 1*s*	T	1400/3400	2-20	400	RO85
		E			401	CFP&87
		T			402	BNH92
		E			150-650	BIB93
N_2O	N 1*s*	T			400	RO85
		E	1400/3400	2-20	401	CFP&87
COS	O 1*s*	E	1300	4-20	520-560	ETH&00
CO_2	O 1*s*	T		0-15	535.4	MB93
		E	1300	4-28	520-580	ETH&99
COS	S 2*p*,2*s*	E	1300	4-24	155-205	ETH&00
CS_2	S 2*p*,2*s*	E	1300	4-28	160-185	ETH&00
SF_6	S 2*p*,2*s*	E	2500	0.5-3.5	160-210	YML93
		E	1500	4-16	165-210	TFT&95
		T	2500	0.5-3.5	170-185	FCM96
		E	1500	4-12	165-260	HEF&98
		E	1300	4-36	165-260	EFT&99

impact energy for the inner-shell of various molecules to date.

This thesis presents major advances in the study of GOS for a few molecules: SF_6 (chapter 5), CO_2 (chapter 6), COS and CS_2 (chapter 7).

The limiting behavior of the GOS has historically been used to derive optical properties from electron impact experiments either by extrapolating GOS measurements made at a series of momentum transfers to $K = 0$ or by using sufficiently high impact energies and small scattering angles such that $K \rightarrow 0$.

Therefore, electron-impact spectra obtained at non-zero scattering angles furnish valuable spectroscopic information about dipole-forbidden (quadrupole and/or singlet-triplet) electronic transitions.

These ideas remained essentially unexplored up until about 1959 when they were applied by Lassettre [L59] to the determination of optical (dipole) oscillator strengths for discrete atomic and molecular transitions. In a series of experiments [LS74, L74] Lassettre and his co-workers measured the GOS for a number of transitions as a function of K^2 by varying the scattering angle at moderately high (300 - 500 eV) impact energy.

The intensities were extrapolated to zero momentum transfer and in general gave highly accurate values for the dipole (optical) oscillator strength (see chapter 2 for details). Similar studies were carried out by Hertel and Ross [HR68, HR69] for alkali atoms, but this time the momentum transfer was varied by changing the impact energy. Such extrapolations were tedious and not open to widespread application, especially in the continuum.

Meanwhile, Boersch and Geiger had shown [BGR68] that the direct use of very high electron impact energy (33 keV) at $\theta = 0°$ gave discrete electron energy loss excitation spectra that were overwhelmingly dominated by dipole-allowed transitions. However, this work was not extended to the routine measurement of oscillator strengths, a development that was to be pioneered by M. J. Van der Wiel [V70, V71]. Van der Wiel, using his so-called "poor man's synchrotron", elegantly and convincingly showed how EELS could be used sufficiently close to the $|K|^2 \rightarrow 0$ optical limit to directly obtain dipole oscillator strengths for atomic photoabsorption in the noble gases.

Momentum transfer experiments where the impact energy is fixed and the scattering angle is varied can be labeled as *variable scattering angle* or *angle resolved* studies. Under these conditions, the GOS concept applies if the FBA is valid (E_0 is sufficiently large and the scattering angles are sufficiently small).

Determination of the GOS for a particular electronic transition (or range of transitions) as a function of momentum transfer (K, or K^2 usually in a.u.$^{-2}$) generates the so-called *GOS profile*. Examination of the shape of a GOS profile offers information on the qualitative nature of the transition of interest and gives insights into the nature of the underlying interactions. In particular, the GOS profiles for dipole-allowed transitions display a decrease in magnitude with increasing momentum transfer, whereas transitions with significant quadrupole component display the opposite effect up to $K^2 \sim 10$–15 a.u.$^{-2}$, decaying after that value. Thus, GOS profiles can aid in spectral assignments. One of the first uses of GOS profiles was in determination of absolute OOS values from EEL results by extrapolation of the momentum transfer to zero [LS74, BBS91]. A detailed

methodology for obtaining GOS profiles from EELS spectra will be described in chapter 4 of this thesis.

1.4.1. Spin Exchange and Triplet States

There is also the consideration of spin angular momentum. Formally, for low Z species (i.e., within the L-S coupling scheme), optical transitions accompanied by a change of spin are forbidden and thus a singlet initial state will result in a singlet final state after undergoing an electronic transition. It is possible to relax this selection rule and produce triplet excited states using EEL techniques.

When the energy of the incident electron approaches the energy of a particular induced electronic transition in the target, the FBA is no longer valid. Under such scattering conditions one must consider a system where the incident and target electrons can lose their identity in the resulting slow collision, thereby exchanging.

Shaw *et al.* in 1982 [SKR&82] reported the first inner shell forbidden transition. They observed the spin forbidden, singlet-to-triplet N $1s \rightarrow \pi\ 2p$ transition in N_2 at an impact energy less than 600 eV (compared to the 400 eV energy loss). Since then, singlet-triplet $1s \rightarrow \pi^*$ transitions have been observed in CO, COS and CS_2 [UT83, HK86, HK87]. In the case of CO, the impact energy was as low as 8 eV above the excitation threshold [HK86].

This type of scattering experiment where spin forbidden transitions are induced can be labeled as a *variable impact energy* study, as the necessary momentum transfer is generated via lowering E_0.

1.4.2. Bethe Surfaces

One of the most challenging and interesting experiments that requires both variable impact energy and variable scattering angle instrumental capability is the construction of the so-called *Bethe surfaces* [IIT71]. The dependence of the absolute GOSs of the individual electronic transitions on the energy loss and momentum transfer can be summarized in a Bethe surface plot. The Bethe surface contains important information about the inelastic electron process within the FBA, and is particularly useful for analyzing such quantities as stopping power, total inelastic scattering cross section and polarizability [I71].

Energy loss spectra are acquired at a series of momentum transfers, and a 3D representation is constructed using the energy loss, momentum transfer and GOS as the coordinates. Inokuti, who discussed the Bethe surface of the H atom in detail [IIT71], gave an informative treatment. Other examples for the inner shells in the literature include the Bethe surfaces for the N 1*s* edge of NH_3 [LDW79, LDW&80], the C 1*s* edge of CO_2 and the S 2*p* edge in SF_6 [TFT&95].

1.5. Practical Applications

A variety of fields benefit from these results [CCB91, CCG&92]. These include astrophysics, atmospheric chemistry, laser development, lithography and radiation physics. For example, the absolute oscillator strength data derived for Ne has been used to re-evaluate the abundance of Ne in B stars [AM73]. In addition, information about

energy levels and absolute oscillator strengths of Ne-like systems is aiding in the development of soft X-ray lasers [E90].

Perhaps one of the most interesting and useful of all applications came with the launching in August 1999 of the most sophisticated X-ray observatory ever built. Chandra is designed to detect and observe X-rays sources from high energy regions of the universe, such as hot gas in the remnants of exploded stars, that are billions of light years away. It produces images twenty-five times sharper than the best previous X-ray telescope. There are plans to explore the composition and chemistry of interstellar clouds by absorption spectroscopy, using the X-ray continuum from more distant stars as a source. The rarefied environment of interstellar clouds is very likely to contain metastable states which can dipole couple to the same final states observed in non-dipole EELS.

Also, momentum transfer studies on chlorofluorocarbons are of great interest. This is primarily due to the participation of these species in the depletion of the ozone layer. These types of EELS studies can identify the nature of specific electronic transition [YML&93, YL94]. Such information can help determine how the molecules dissociate, which may subsequently lead to ozone-depleting reactions. The study of dipole forbidden transitions at large momentum transfer, in addition to those which are dipole allowed provides a more complete understanding of the electronic structure of atoms and molecules than can be obtained from photoabsorption techniques.

1.6. Outline of Thesis Chapters

Chapter 2 outlines the theory and the basic principles behind EELS. In addition, the Bethe-Born theory is examined in some detail.

Chapter 3 documents the design and construction of the McMaster Variable Angle High Resolution Spectrometer (McVAHRES) instrument.

Chapter 4 presents the experimental procedures for GOS studies and data analysis. Data processing for quantitative GOS shapes is presented in detail including the *energy-scan* versus *angle-scan*, spectra normalization, multi-line fit analysis, the new geometric correction and the reason for using it, the kinematic correction, the relative GOS and the conversion factor (N) needed to determine the absolute GOS and error treatment.

The GOS profiles of $T_{1u}(a_{1g})$, $A(t_{1u})$, $B(t_{1u})$, $T_{1u}(t_{2g})$ and $T_{1u}(e_g)$ features in S $2p$ spectra, $A_{1g}(a_{1g})$, $T_{1u}(t_{1u})$, $T_{2g}(t_{2g})$ and $E_g(e_g)$ features in S $2s$ spectra and $T_{1u}(a_{1g})$, $T_{1u}(t_{1u})$, $T_{1u}(t_{2g})$ and $T_{1u}(e_g)$ features in F $1s$ (first time determination) spectra of SF_6 were determined by using McVAHRES. These results are presented in chapter 5 together with new spectroscopic results in the S $2p$ and S $2s$ edges. Papers based on this work have been published [HEF&98, ETH99] or are under review [EFT&99].

Chapter 6 presents new spectroscopic results and GOS studies in CO_2. A paper based on this work has been recently accepted for publishing in Physical Review A [ETH&99].

Chapter 7 shows a GOS study in the closely related molecules COS and CS_2. A paper based on this work is in preparation and will be submitted to Physical Review A [ETH&00].

Suggestions for future developments are discussed in chapter 8.

Chapter 2

THEORY OF ELECTRON ENERGY LOSS SPECTROSCOPY

In this chapter, the basic elements of theory of EELS are reviewed. The Bethe-Born Theory description leads to the concept of GOS. The Theoretical Model for Interpretation of Spectral Intensities is presented along with considerations about the shape of GOS profiles, the Lassettre Series and Origin and Labeling of states and molecular orbitals.

2.1. Basic Theory of Electron Energy Loss Spectroscopy

Theoretical treatments of inelastic collision of charged structureless particles with atoms and molecules may be classified into two kinds: those concerned with *fast* collisions and those concerned with *slow* ones, where fast or slow refers to the velocity of the particle relative to the mean orbital velocity of the atomic or molecular electrons in the shell (or subshell) that connect to the inelastic process under consideration [I71]. For sufficiently *fast* collisions, the influence of the incident particle upon an atom or molecule may be regarded as a sudden and small external perturbation.

The theory of a process in which a *fast* particle transfers a given amount of energy and momentum consists of two distinct factors, one dealing with the *incident particle* only and the other dealing with the *target* only (concerning the GOS of an atom or

molecule). The problem of *slow* collisions, on the other hand, essentially involves a *combined system* of the incident particle plus the target in which the former has lost its mechanical identity.

When an electron beam is incident on a target, some of the electrons are inelastically scattered and lose a fraction of their energy. Electronic, vibrational and rotational excitations are detected as structure in the distribution of energy losses in the scattered electron beam. The process may be represented as seen earlier, in eq. (1.1):

$$e^-(E_0) + M \rightarrow M^*(E_n) + e^-(E_1; \Omega(\theta, \varphi)) \tag{2.1}$$

where M is the target species in its ground electronic state, E_0 is the kinetic energy of the incident electron beam, M^* is an excited state of the target which has internal energy E_n with respect to the ground state and E_1 is the residual kinetic energy of the electron which is inelastically scattered through the angle $\Omega(\theta, \varphi)$ (with respect to the incident beam) in the collision. If the target molecules are randomly oriented in space, which is usually the case in gas phase electron energy loss experiments, the scattering intensity has no azimuthal (φ) angular dependence.

The law of energy conservation gives:

$$E_0 = E_n + E_1 + E_t \tag{2.2}$$

where E_t is the additional translational kinetic energy of the molecule after the collision (see Fig. 1.1). From momentum conservation it can be shown that [K68, H78]:

$$E_t \approx \frac{2mE_0}{M}\left[\left(1 - \frac{E_n}{2E_0}\right) - \left(1 - \frac{E_n}{E_0}\right)^{1/2}\cos\theta\right] \tag{2.3}$$

where m and M are the masses of the incident electron and target molecule respectively. Because of the large mass disproportion between the electron and the target and because of near cancellation of the terms inside the square bracket (if $E_0 >> E_n$), the target recoil energy is very small and may be ignored when small scattering angles are being examined. Therefore the electron energy loss, $E_0 - E_1$ is essentially equal to the energy E_n transferred to the target.

2.2. The Bethe-Born Theory

For a quantitative treatment of small angle inelastic scattering of fast electrons a quantum mechanical scattering theory is required. This was initially derived by Bethe (1930) [B30], extended by Fano (1954) [F54], and reviewed in detail by Inokuti (1971) [I71, IIT78] and Kim (1972) [K72].

The Bethe theory for electron scattering is based on the First Born Approximation (FBA) which assumes that the interaction between the electron and the target is weak and therefore the incident wave (approximated by a plane wave) is negligibly distorted by the interaction. Within this assumption the differential cross section (DCS) for inelastic scattering of an electron into an angle θ while exciting a hydrogen atom to the nth discrete state is given in Hartree atomic units ($\hbar = m = e = 1$) by [F95] :

$$\frac{d\sigma_n}{d\Omega(\theta)} = \frac{1}{(4\pi)^2}\frac{k_1}{k_0}\left|\int U_{0n}(\vec{r}_1)\exp(i\vec{K}\cdot\vec{r})]d\vec{r}\right|^2 \qquad (2.4)$$

where

$$U_{0n}(\bar{r}_1) = 2\int \psi_0^*(\bar{r}_2)\left(\frac{1}{r_{12}} - \frac{1}{r_1}\right)\psi_n(\bar{r}_2)d\bar{r}_2 \tag{2.5}$$

and $\psi_0(\bar{r}_2)$ is the ground state wavefunction, $\psi_n(\bar{r}_2)$ is the excited state wavefunction, $\bar{r}_1$ and $\bar{r}_2$ are the coordinates of the incident and target electrons, r_{12} is the interelectron distance and $\hbar K$ is the momentum transfer in the collision given by:

$$K^2 = \left|\bar{K}\right|^2 = \left|\bar{k}_0 - \bar{k}_1\right|^2 = k_0^2 + k_1^2 - 2k_0k_1\cos\theta \tag{2.6}$$

where k_0 (k_1) is the wavenumber of the incident (scattered) electron.

This can be generalized by including the interaction with all of the target electrons so that:

$$U_{0n} = 2\int \psi_n^*\left[-\sum_{s=1}^{N}\frac{1}{\bar{r}-\bar{r}_s} + \frac{Z_N}{r}\right]\psi_0 d\bar{r}_1 \ldots\ldots d\bar{r}_N \tag{2.7}$$

where $\bar{r}$ is the position vector of the incident electron with respect to the nucleus (of charge Z_N) and the integration is carried out over the positions of all atomic electrons (whose coordinates are $\bar{r}_s$). Bethe has simplified the expression by substituting (2.7) into (2.4) and using

$$\int \frac{\exp(i\bar{K}\cdot\bar{r})}{|\bar{r}-\bar{r}_s|}d\bar{r} = \frac{4\pi}{K^2}\exp(i\bar{K}\cdot\bar{r}_s) \tag{2.8}$$

Thus, when the particle is sufficiently fast but still non-relativistic, the DCS for small angle inelastic scattering is given by combining (2.4), (2.7) and (2.8) (neglecting the nuclear term which is zero if the atomic wavefunctions are orthogonal):

$$\frac{d\sigma_n}{d\Omega(\theta)} = 4\frac{k_1}{k_0}\frac{1}{K^4}\left|\int\psi_n^*\sum_{s=1}^{N}\exp(i\bar{K}\cdot\bar{r}_s)\psi_0 d\tau_N\right|^2 \tag{2.9}$$

where $d\tau_N$ indicates integration over all the coordinates of the N atomic electrons, or

$$\frac{d\sigma_n}{d\Omega(\theta)} = 4\frac{k_1}{k_0}\frac{1}{K^4}\left|\varepsilon_{0n}(\bar{K})\right|^2 \tag{2.10}$$

where

$$\varepsilon_{0n}(\bar{K}) = \int\psi_n^*\sum_{s=1}^{N}e^{i\bar{K}\cdot\bar{r}_s}\psi_0 d\tau_N \tag{2.11}$$

If one takes a closer look at the origin of the $\exp(i\bar{K}\cdot\bar{r}_s)$ term in eq. (2.11) that gives the matrix element, this can be derived using a simple two-electron state picture for fast incident electron and one of the N electrons in the target atom (whose coordinates are $\bar{r}_s$). The initial two-electron state describes the incoming fast electron by $\psi_{inc}(\bar{r}_1)$ and the ground state electron "2" by $\psi_0(\bar{r}_2)$. The final two-electron state describes the outgoing scattered electron "1" by $\psi_{out}(\bar{r}_1)$ and the excited electron "2" in the target by $\psi_n(\bar{r}_2)$. Thus, assuming a weak interaction, $\varepsilon_n(\bar{K})$ can be expressed as:

$$\varepsilon_{0n}(\bar{K}) = \left\langle\psi_n(\bar{r}_2)\cdot\psi_{out}(\bar{r}_1)\,|\,H_{\text{int}}\,|\,\psi_{inc}(\bar{r}_1)\cdot\psi_0(\bar{r}_2)\right\rangle \tag{2.12}$$

where H_{int} is the Coulombic interaction operator, given by:

$$H_{\text{int}} = \frac{1}{\left|\bar{r}_1 - \bar{r}_2\right|} \tag{2.13}$$

Within the FBA, the incoming and outgoing scattered electron can be expressed as single plane wave:

$$\psi_{inc}(\vec{r}_1) \Rightarrow \exp(i\vec{k}_0 \cdot \vec{r}_1) \tag{2.14}$$

$$\psi_{out}(\vec{r}_1) \Rightarrow \exp(i\vec{k}_1 \cdot \vec{r}_1) \tag{2.15}$$

Substitution of (2.14) and (2.15) in (2.12) yields the following more explicit form:

$$\varepsilon_{0n}(\vec{K}) = \int d\vec{r}_1 \int d\vec{r}_2 \psi_n^*(\vec{r}_2) \exp(-i\vec{k}_1 \cdot \vec{r}_1) \frac{1}{|\vec{r}_1 - \vec{r}_2|} \exp(i\vec{k}_0 \cdot \vec{r}_1) \psi_0(\vec{r}_2) \tag{2.16}$$

or

$$\varepsilon_{0n}(\vec{K}) = \int d\vec{r}_1 \int d\vec{r}_2 \psi_n^*(\vec{r}_2) \frac{1}{|\vec{r}_1 - \vec{r}_2|} \exp[i(\vec{k}_0 - \vec{k}_1) \cdot \vec{r}_1] \psi_0(\vec{r}_2) \tag{2.17}$$

With $\vec{K} = \vec{k}_0 - \vec{k}_1$ and $\vec{r}_1 = \vec{r}_2 - \vec{r}$, substitution into (2.17) yields:

$$\varepsilon_{0n}(\vec{K}) = \int d\vec{r}_2 \psi_n^*(\vec{r}_2) \left[\int d\vec{r} \left(\frac{1}{r} \right) \exp(i\vec{K} \cdot \vec{r}) \right] \exp(i\vec{K} \cdot \vec{r}_2) \psi_0(\vec{r}_2) \tag{2.18}$$

Recognizing that (2.18) can be simplified using a Fourier transform, one obtains the final expression:

$$\varepsilon_{0n}(\vec{K}) = const \left\langle \psi_n(\vec{r}_2) \,|\, \exp(i\vec{K} \cdot \vec{r}_2) \,|\, \psi_0(\vec{r}_2) \right\rangle \tag{2.19}$$

which depends only on the electron in the target with coordinate $\vec{r}_2$. Letting $\vec{r}_2 = \vec{r}_s$ in (2.19) and summing over all N electrons in the target, leads directly to the operator in expression (2.11) for a multielectron atom.

Eq. (2.11) is further generalized to electron-molecule scattering by using the appropriate molecular wavefunction. In this case one normally assumes the validity of the Born-Oppenheimer approximation and expresses the molecular wavefunctions as the product of electronic and nuclear terms:

$$\psi_{evr}(\vec{r};\vec{q}) = \psi_e(\vec{r};q_0)\cdot\psi_{vr}(\vec{q}) \tag{2.20}$$

where ψ_{evr} designates the total wavefunction describing the electronic (e), vibrational (v) and rotational (r) motions, $\vec{r}/\vec{q}$ are the coordinates of the electrons/nuclei and q_0 is a fixed nuclear configuration. Within this approximation the intensities of vibrational excitation accompanying an electronic transition are given by Franck-Condon factors (overlaps of initial and final state vibrational wavefunctions) so that the differential cross-section for electron-molecule scattering involving excitation from the ground state (e_n, v_n, r_n) is given by (2.10) with:

$$\varepsilon_{0n}(\vec{K}) = \left\langle \psi_{e_n} \left| \sum_{s=1}^{N} \exp(i\vec{K}\cdot\vec{r}_s) \right| \psi_{e_0} \right\rangle \cdot \left\langle \psi_{v_n r_n} \mid \psi_{v_0 r_0} \right\rangle \tag{2.21}$$

It is useful to note that, from (2.4) and (2.9), in the Bethe-Born expression for inelastic DCS, all of the target dependent factors are included in the $\exp(i\vec{K}\cdot\vec{r}_s)$ matrix element while the remainder of the expression solely involves kinematic factors, dependent only on the value of the energy loss and the experimental scattering conditions.

2.3. The Generalized Oscillator Strength (GOS)

2.3.1 The Theoretical Model for Interpretation of Spectral Intensities

Since the work of Bethe [B30] in 1930 it has been known that the GOS, a quantity related to the excitation of atoms and molecules by electron impact, approaches the OOS as the momentum change of the colliding electron approaches zero. Bethe has shown

that electron impact excitation can also be described within the first Born approximation (FBA) in terms of a GOS given by a simplified formula (in Hartree atomic units):

$$f_n(K) = \frac{E_n}{2}\frac{1}{K^2}\left|\varepsilon_{0n}(K)\right|^2 \tag{2.22}$$

where $\varepsilon_{0n}(K)$ is the matrix element for the electric-dipole transition from the ground "0" to the excited state "n" and is defined by (2.11).

By combining (2.10) and (2.22), an effective GOS, $f'_n(K)$ can be calculated entirely from experimental parameters regardless of the validity of the FBA:

$$f'_n(K) = \frac{E_n}{2}\frac{k_0}{k_1}K^2\frac{d\sigma_n}{d\Omega} \tag{2.23}$$

From (2.22) and (2.11), the GOS $[f_n(K)]$ is defined as:

$$f_n(K) = \frac{E_n}{2K^2}\left|\left\langle \psi_0 \mid \sum_{s=1}^{N}\exp(iK\cdot r_s) \mid \psi_n \right\rangle\right|^2 \tag{2.24}$$

where E_n is the energy lost by the incident electron to the target, ψ_0 and ψ_n are the electronic wavefunctions describing the target in its initial and final states respectively and r_s specifies the position of the s-th of N target electrons with respect to the center of mass of the target. In the limit as the momentum transfer, K, approaches zero, the GOS reduces to:

$$\lim_{K\to 0} f_n(K) = \frac{E_n}{2}\left(\varepsilon_1^2\right)_{0n} \tag{2.25}$$

where ε_{10n} is the matrix element for the electric dipole transition from the ground state ψ_0 to the excited state ψ_n.

Equation (2.25) is important since it establishes a link between energy loss and photoabsorption intensities. This link also suggests that the mechanism for energy transfer for electrons scattered at zero angle must be similar to that in the photon case. This means we can view zero angle inelastic scattering as a long range encounter between the electron and the target, in which the target is excited by absorbing energy from the momentary electric field supplied by the passing electron.

The relationship between OOS and GOS becomes apparent when the exponential in the matrix element (2.9) is expanded in a power series in K:

$$\exp(i\vec{K}\cdot\vec{r}) = 1 + (i\vec{K}\cdot\vec{r}) + \frac{1}{2}(i\vec{K}\cdot\vec{r})^2 + \ldots + \frac{1}{n!}(i\vec{K}\cdot\vec{r})^n \tag{2.26}$$

Substituting (2.26) into the matrix element of (2.9) and assuming that ψ_n and ψ_0 are orthogonal:

$$\varepsilon_{0n}(K) = \varepsilon_1(iK) + \varepsilon_2(iK)^2 + \varepsilon_3(iK)^3 + \ldots \tag{2.27}$$

and

$$f_n(K) = \frac{E_n}{2}\left[\varepsilon_1^2 + (\varepsilon_2^2 - 2\varepsilon_1\varepsilon_3)K^2 + O(K^4)\right] \tag{2.28}$$

where

$$\varepsilon_l = \frac{1}{l!}\left\langle \psi_n \left| \sum_s \vec{r}_s^{\,l} \right| \psi_0 \right\rangle \tag{2.29}$$

and ε_l is thus the lth order multipole matrix element (l = 1 is electric dipole, l = 2 is electric quadrupole, l = 3 is electric octupole, etc.).

From eq. (2.28) it can be seen that:

$$\lim_{K\to 0} f_n(K) = \frac{E_n}{2}\varepsilon_1^2 = f_n \tag{2.30}$$

Thus the GOS approaches the OOS at small momentum transfer and in the limit of zero momentum transfer, only electric dipole induced transitions will be observed.

It is interesting to note that electric dipole transitions still dominate ISEELS even at relatively large K values because of the very small spatial extent of the core orbitals. In principle, one needs to measure energy loss spectra at a range of momentum transfers and extrapolate to zero K in order to obtain accurate OOS from GOS. However, in many cases it suffices to work at sufficiently small K such that the GOS becomes a good approximation to the OOS.

While there is good match between photoabsorption and ISEELS in the majority of spectra recorded under dipole scattering conditions ($E_0 > 1$ keV, $\theta < 5°$), there are some very interesting cases where inner-shell electric quadrupole transitions have been identified through comparisons between low-K ISEELS and optical studies [HB78, SB85].

Also, when the incident electron energy is no longer large relative to the transition energy, there are strong interactions between the target and the scattered electrons so that the FBA no longer holds. At large scattering angles ($\theta > 5°$) and intermediate energies (2-5 times the transition energy) quadrupole transitions become increasingly important. An example of how the FBA breaks down in such experimental conditions will be shown in chapter 5 for SF_6.

As the impact energy approaches the threshold for the electronic transition the probability of an "exchange" between the incident and the target electron increases. This leads to the detection of spin-exchange transitions. Such studies can be particularly useful for distinguishing valence and Rydberg core-excited states [HK86] since appreciable singlet-triplet splittings are only found in intense transitions corresponding to core excitations into compact virtual orbitals of a large valence character.

2.3.2. The GOS Shape

By looking at the characteristic *shapes* of GOS profiles, one can notice the difference between an optically allowed transition and an optically forbidden transition with respect to both the magnitude and the behavior at the optical limit $K \rightarrow 0$.

The cross section, to which the GOS is proportional, is related to the impact parameter (b) (see section 1.3.1 and Fig. 1.2). The fact that $f_n(K)$ is finite and greatest at $K \rightarrow 0$ for the *allowed* excitations reflects the efficiency of collisions with large impact parameters in exciting allowed transitions [I71]. Scattering processes at large impact parameter correspond to low scattering angle, small momentum transfer collisions in which an energetic electron passes far from the molecule. When the impact parameter is small, the incident electron approaches very close to the target and it is typically scattered at a high scattering angle, with a high momentum transfer. The size of the impact parameter defines an area around the target. Clearly for the large impact parameter regime this area (πb^2), which is proportional to the excitation cross-section, is much greater than that for the small impact parameter regime. Thus the cross section at large

impact parameter is much larger than that at small impact parameter and in general one expects a continuous decline in cross section with increasing angle. For non-dipole transitions the zero-intensity forbidden process at $K = 0$ combined with the general decline of cross-sections at larger angle (smaller impact parameter) leads to formation of a characteristic maximum in the GOS profile. In some cases, such as two coherent channels for a given excitation, there can be additional maxima in GOS profiles [M75, KM69, MMK69].

2.3.3. Bethe Surface

To indicate a further use for the GOS, consider the expression of the total cross section for the inelastic scattering involving a particular energy loss. Using (2.10) and (2.22), this can be written as [B79]:

$$\int d\Omega \frac{d^2\sigma}{d\Omega dE_n} = \frac{4k_1}{k_0} \int \frac{d\Omega}{K^2 E_n} f_n(K) = \frac{4\pi}{k_0^2 E_n} \int_{K^2_{min}}^{K^2_{max}} d[\log K^2] f_n(K) \qquad (2.31)$$

where k_0^2 is the incident electron energy and K^2_{min} and K^2_{max} are the minimum and maximum allowed values of the square of the momentum transfer. Thus, it is particularly convenient to exhibit graphically the complete GOS by plotting $f_n(K)$ as a function of log K^2 and E_n. Such a plot defines a *Bethe surface* [I71] and, the complete knowledge of a Bethe surface makes it possible to learn a great deal about the target system under study. The *Bethe surface* represents a three-dimensional representation of the GOS over large ranges of energy loss and momentum transfer. One of the principal features in any Bethe surface is a diagonal ridge running through it, the *Bethe ridge* which is associated with

Compton scattering of the incident electron by the valence electrons.[I71, LCS89, LDW&80]

2.3.4. The Lassettre Series

Lassettre [L65] has pointed out that the GOS for bound-state excitations can be expanded in a power series in even powers of the momentum transfer in the form:

$$f(K,E) = f_0 + \sum_{l=1}^{\infty} b_l \left(\frac{K^2}{K^2 + \alpha^2} \right)^l \tag{2.32}$$

where

$$b_l = \sum_{m=1}^{l} f_m \binom{l-1}{m-1} \alpha^{2m} \tag{2.33}$$

and

$$\alpha = \sqrt{I} + \sqrt{I - E} \tag{2.34}$$

with I the first ionization potential above the energy loss E_{loss} under consideration and $\binom{l-1}{m-1}$ is a binomial coefficient [L65]. Equation (2.32) is useful as a means of extrapolating experimental data to higher and lower values of K.

So far we have restricted ourselves completely to cases where the Born approximation is assumed to be valid. Actually a number of important theoretical results exist which go *beyond the Born approximation*. The most important of these relations, also due to Lassettre and co-workers [LSD69], is a theorem which states that:

$$\lim_{K \to 0} \left(\frac{E_n k_0 K^2}{2k_1} \right) \left(\frac{d^2\sigma}{d\Omega dE_n} \right)_{expt} = \lim_{K \to 0} f'(K,E)_{expt} = \lim_{K \to 0} f(K,E) = f(E) \tag{2.35}$$

where $f'(K,E_n)_{expt}$ is the effective GOS [eq.(2.23)] defined in terms of the experimental cross-section and $f(K,E_n)$ is the usual definition of the GOS. This theorem says that if the experimentally observed effective oscillator strength can be accurately extrapolated from the last physically observable value of $K \approx E_n/2k_0$ ($\theta = 0°$) to the value at $K^2 = 0$, then one can obtain the correct OOS even if the Born approximation is not applicable in explaining the data in the physically observable region. The importance of this theorem in the high energy electron impact spectroscopy domain is that for a fixed transition energy or energy loss E, the extrapolation becomes more reliable as the incident energy and hence k_0 increases (i.e., $K(\theta = 0°) \approx E/2k_0$ becomes smaller).

The modified Lassettre series [L65, DL75], provides a semi-empirical connection between measured GOS profiles and the coefficients in equation (2.28) :

$$f(K,E) = \frac{1}{(1+x)^6} f_0 \sum_{n=0}^{m} \frac{f_n}{f_0} \left(\frac{x}{1+x} \right)^n \qquad (2.36)$$

where $x = K^2 / [(2I)^{1/2} + (2|I - E_n|)^{1/2}]^2$. Quantum mechanically, f_n is related to linear combinations of the respective multipole matrix elements. In the limit when K approaches zero, $f(K, E)$ approaches the dipole oscillator strength (OOS) value, f_0. The original Lassettre series was developed to quantitatively deduce precise OOS values by extrapolating the measured GOS data, obtained by angle-resolved EELS to the zero K limit. The second term, f_1, in the series is related to the quadrupole interaction through the difference of the square of the quadrupole matrix element and the product of dipole and octupole matrix elements (equation 2.28). Higher order terms give measures of the other multipole contributions. In practice the summation is usually limited to $m = 3$ since

including higher terms increases the errors in the lower terms, making the values unreliable. A direct electric quadrupole transition would be characterized by a positive f_1 term. In contrast f_1 for an electric dipole transition is negative since the product of the dipole and octupole matrix elements is larger and positive.

2.3.5. Origin and Labeling of States and Molecular Orbitals

Electron spectroscopy deals with transitions of molecules between different electronic *states*. More specifically, inner-shell electron spectroscopy studies the electronic transitions between the ground state and core excited states of a molecule. A state is a mathematical concept defined by a wavefunction, which describes the position and the motion of all electrons in the molecule. Usually, most core excitation processes consider the simpler picture of just one electron excitation from the core level to a final level.

In terms of the MO theory, an electron is promoted from a low energy orbital to a higher energy *orbital*, or, the electron configuration is changed such that the overall energy is increased. An orbital is a one-electron wavefunction that describes the distribution of an electron in an atom or molecule. The molecular wavefunction can be approximated as a linear combination of atomic orbitals (LCAO) [HAK&84]. An atomic orbital is a wave function that describes the behavior of one electron with respect to the nucleus of an atom.

If for the description of diatomic molecules we choose a coordinate system with its z-axis along the internuclear axis, σ valence orbitals originate from atomic $2s$ and/or $2p_z$ orbitals and π orbitals arise from $2p_x$ and $2p_y$ atomic orbitals [P60, JS73, MKT85].

For diatomic molecules, σ orbitals are symmetric with respect to reflection through a plane containing the symmetry axis of the molecule and π orbitals are antisymmetric. In polyatomic molecules, the MOs involve atomic overlap, which is generally more extended, but the resulting orbitals can still be labeled either σ, symmetric, or π, antisymmetric, with respect to a local symmetry plane [JS73]. For σ orbitals or bonds there is no nodal surface that contains the bond axis, while a π bond has one nodal surface or plane containing the bond axis. The σ bond is always present while the existence of a π bond depends on the atomic constituents of the molecule and the number of valence electrons available for bonding.

For $1s$ spectra, it is the nonfilled antibonding orbitals which are of importance, since the observed resonances correspond to dipole allowed transitions of a $1s$ core electron to π and σ antibonding orbitals. For homonuclear and polyatomic molecules with center of symmetry, orbitals are given a second label ***g*** (*gerade*) or ***u*** (*ungerade*) indicating the *inversion symmetry through the center of the molecule.* For complex molecules it is appropriate to use group theory and designate the MOs by their irreducible representations, rather than by the simple σ and π label [K85, C71].

Since the dipole operator is a vector with components (x, y, z), *a transition will be electric dipole allowed if the direct product of the irreducible representations of the*

initial and final states is, or contains, the irreducible representation to which x, y or z belongs. More specifically, from equation (2.29), the electric dipole matrix element can be written as $\varepsilon_1 = \langle \psi_n | r | \psi_0 \rangle$, while the electric quadrupole matrix element is $\varepsilon_2 = \frac{1}{2}\langle \psi_n | r^2 | \psi_0 \rangle$, transforming thus as x^2, y^2, z^2, xy, xz, yz.

Chapter 3

INSTRUMENT DESIGN AND PERFORMANCE

The basic high-energy electron impact spectroscopy experimental set-up consists of an electron beam source, a target usually consisting of a gas jet or a fixed volume of low-pressure gas, confined to a container with small apertures for admission of the incident electrons and for exiting of scattered and unscattered electrons, and an energy analyzer with an electron detector. The intensity of the inelastically scattered electrons is measured as a function of the energy loss at various scattering angles, θ. This chapter presents an update of the design, construction and performance of McVAHRES (McMaster Variable Angle High Resolution Electron Spectrometer) as it was used to investigate the electronic spectroscopy of gases and map generalized oscillator strengths. The spectrometer features sophisticated computer-controlled electron optics that allows a high degree of flexibility with regard to spectrometer operation.

3.1. Introduction

This chapter describes the design, construction and operating procedures of an electron energy-loss spectrometer optimized for inner-shell spectroscopic studies under a

wide range of experimental scattering conditions. The spectrometer performs quantitative studies of dipole allowed (small angle), spin forbidden (variable E_0), and dipole forbidden (variable angle), valence and inner-shell experiments.

Other EELS spectrometers for inner-shell studies are optimized for only one or a few of these areas. The Waterloo system [YDM&93, YML93, YML&93, YL94, YML94] uses a fixed, high impact energy (2.5 keV), has a comparatively limited angular range, and modest energy resolution (0.8 eV FWHM). The Indiana [BB92] and Rome spectrometers [CFP&87] have a large angular range but modest resolution (> 0.5 eV FWHM). The Manchester spectrometer [HK86, HK87] works at extremely low impact energies with modest resolution (~ 0.8 eV FWHM) and a fixed 90° scattering geometry.

The McMaster spectrometer has already been used to study non-dipole inner-shell excitation of a variety of species. Spin-forbidden, C 1*s* core excited triplet states of CO, C_2H_4, C_2H_2 and C_6H_6 have been characterized [FEL&94]. The momentum transfer dependence and vibrational structure of the (C $1s \rightarrow \pi^*$) $^3\Pi$ state of CO was investigated [FKH94]. The spectroscopy and GOS profiles for S 2*p* and S 2*s* excitation of SF_6 [TFT&95, HEF&98, FTT&95, ETH99] and C 1*s* and O 1*s* excitations in CO_2 [ETH&99] have also been studied.

All the spectroscopy-related studies were performed with the monochromated version of the spectrometer. Its construction and performance has been described in detail previously by James Francis who built it [F95]. For the GOS studies an optional unmonochromated version was later implemented.

This chapter will describe both setups, while mentioning that the unmonochromated mode was used for all the results presented in chapters 5, 6 and 7.

I used the monochromated setup in a study of the isomeric sensitivity of the C 1s spectra of xylenes [EHU&98].

3.2. The Original Monochromated Spectrometer Design

Full details on the mechanical design and electronics are presented in the Ph. D. thesis of James Francis' [F95].

3.2.1. General Considerations

Briefly, the spectrometer consists of a thermionic electron source, a monochromator, a collision region, an electron velocity analyzer, a single electron sensitive detection system (channel electron multiplier detector), along with a sophisticated electrostatic lens system to transport, accelerate, and optimize the beam among these elements. Full hemispherical electrostatic deflectors are used for both monochromator and analyzer.

Energy loss spectra, the distribution of electrons inelastically scattered by a sample gas at a fixed detection angle, are measured by retarding the electrons to a constant final energy (and therefore fixed resolution) prior to velocity analysis. The energy loss spectrum is scanned by adding the desired energy loss to the impact energy before the collision.

The main goal is to study dipole-forbidden core excitation processes. Therefore, the electron optics has to allow impact energies from a few hundred eV to a few keV, the scattering angle has to be mechanically scanable over a wide range (achieved in this case by scanning the analyzer and detector), and the overall efficiency of the optics and velocity selectors has to be as high as possible due to the low cross sections of the features of interest.

Cross-sectional, three-dimensional and plan views of the spectrometer are presented in **Fig. 3.1**. It incorporates variable impact energy (200 – 2000 eV) and variable scattering angle (-35 to +85°).

The voltages for the velocity selector and associated lenses are supplied by computer-interfaced power supplies. All parts are manufactured from non-magnetic materials (aluminum, brass or non-magnetic stainless steel). Ceramic alumina spacers and rods, teflon tubing, and ruby balls are used to electrically isolate and to maintain the alignment of the various elements.

3.2.2. The Vacuum

The base plate of the chamber has two turbo ports. The main port has a Balzers Turbo Molecular Pump backed by an Alcatel rotary pump that provides a typical base pressure of ~ $2x10^{-7}$ torr without backing.[F95]

Gaseous samples are introduced either through a capillary array (Minitubes – Grenoble, 7, Ave. de Grand Chatelet, 38100 Grenoble, France) centered on the collision region, or through a 1/8" stainless steel tube entering the chamber far from the collision

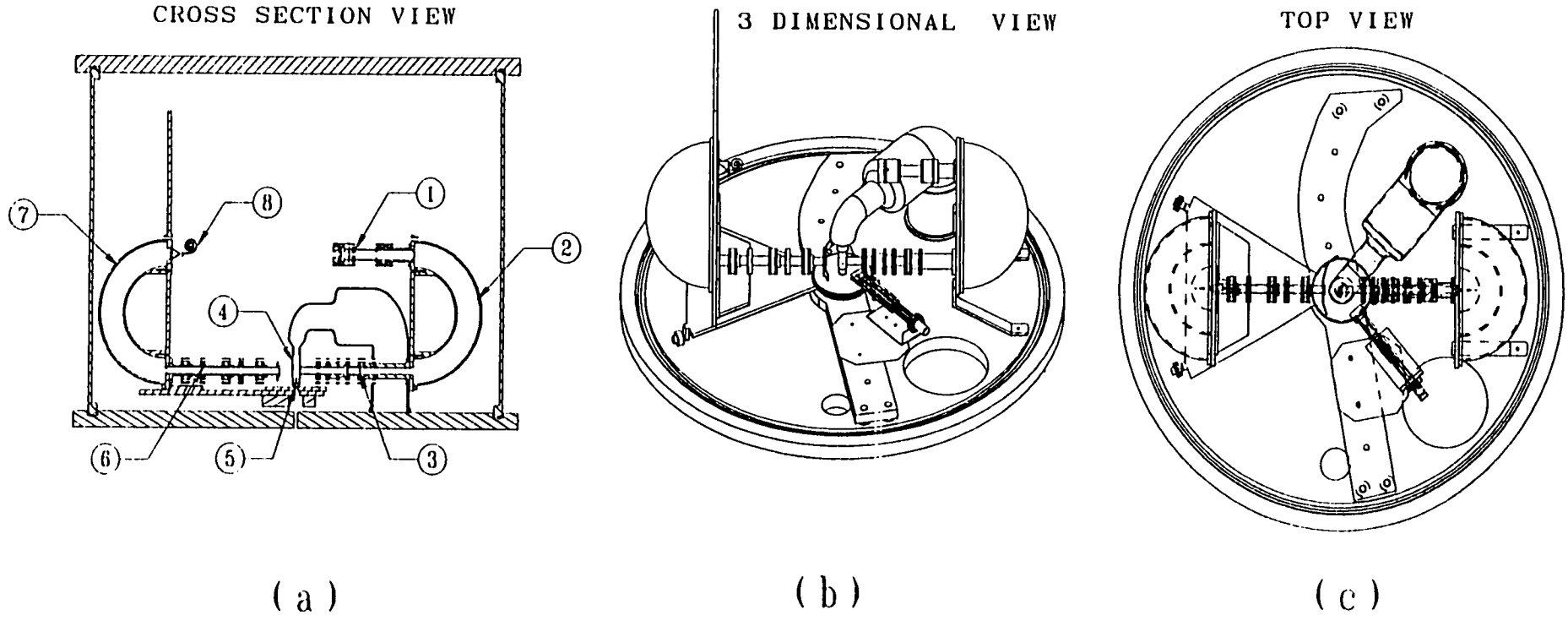

Fig. 3.1 Schematic of the spectrometer. **(a)** cross section view, showing: the electron gun (1), the monochromator (2), the monochromator exit lens (3), the gas cell (4), the capillary array (5), the analyzer entrance lens (6), the analyzer (7) and the detector (8). The **(b)** 3D view and **(c)** top view show both monochromated and unmonochromated implementations. The unmonochromated electron gun is positioned at the same level as the analyzer lens and faces the collision cell.

region. The latter is used to measure background signals as described in chapter 4. A three-way valve distributes the sample gas through one of these two channels. A Granville Phillips leak valve controls the sample flow rate. The vacuum in both parts of the apparatus is monitored with Bayard-Alpert ionization gauges.

3.2.3. Rotation Mechanism

The deceleration lens, analyzer and detector are mounted on a rotatable aluminum platform driven by a reduction geared rotation mechanism. A computer interfaced stepper motor drives the reduction gear. There was a 5° backlash that had to be accounted for whenever the rotation direction was changed. The total angular range for this setup is ~ 120°, from -35° to 85° [F95].

3.2.4. The Electron Optics

The electron optics were designed with the help of the electrostatic lens design algorithm SIMION (D. A. Dahl and J. E. Delmore, SIMION PC/2 Version 3.1 Idaho National Laboratory, EG&G Idaho Inc., Idaho Falls, ID 83415), which analyzes charged particle trajectories in a system of electrostatic fields created by a collection of shaped electrodes, of cylindrical symmetry in this case. All lens elements were chosen as cylinder type. The individual sections comprising the overall spectrometer are each described in turn in the following paragraphs.

3.2.4.1. Electron Gun

The electron gun was required to produce high current at low electron energy and to make a 1mm image at the entrance of the monochromator, with nearly parallel incident beam. Thermionic emission from a DC-heated tungsten hairpin filament was used since it has better stability, higher emission, and reduced sensitivity to reactive gases, relative to indirectly heated oxide cathodes.

The overall gun design (**fig. 3.2a**) was adapted from a low energy spectrometer design by Tronc. The first stage extracts the electrons produced by the filament using a conventional cathode-grid-anode system and accelerates them to the second stage, a three-element lens which decelerates and focuses the beam at the entrance of the monochromator at the desired pass energy.

3.2.4.2. Monochromator Exit Lens

The monochromator exit lens accelerates the energy selected beam of low energy electrons (typically 10 - 25 eV) which passes through the (virtual) monochromator exit aperture up to the impact energy (200 - 2000 eV). The lens is required to form a low divergence, ~ 1mm diameter beam at the collision region.

The design chosen was a five-element lens (**fig. 3.2b**) that accelerates the low energy electrons to the final impact energy in two stages since single-stage lenses (i.e., two or three elements) produce unacceptable aberrations at large acceleration ratios.

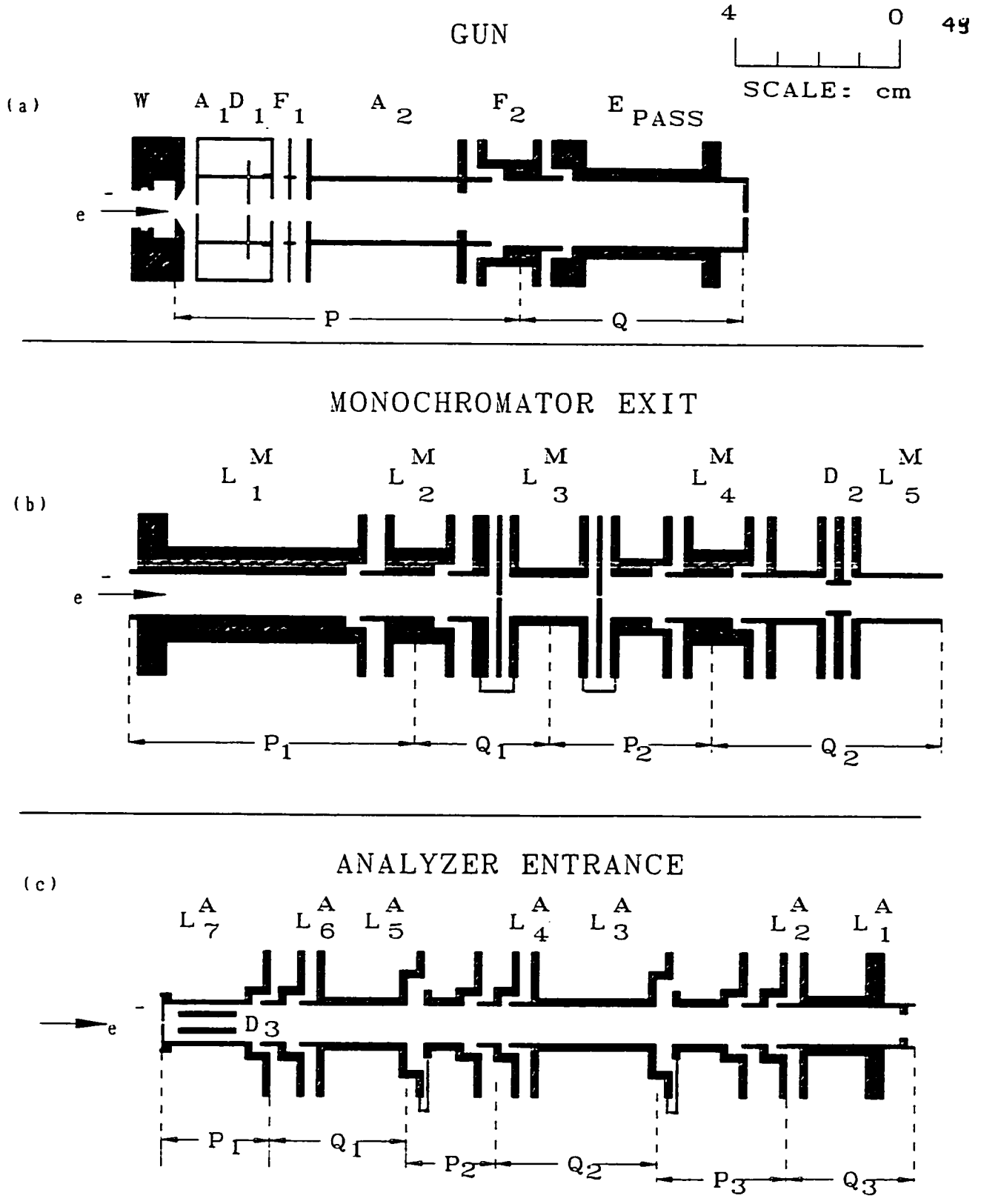

Fig. 3.2 (a) Schematic of the electron gun used in monochromated operation. **(b)** Schematic of the monochromator exit lens system. **(c)** Schematic of the analyzer entrance lens system.

By placing two real apertures of 1 mm in diameter separated by 25 mm, centered on the third lens of the monochromator (L^{M}_{3}) (fig. 3.2b), virtual apertures are created as images at the entrance and exit of the lens system [HR75, CNK74]. Virtual apertures reduce sensitivity to patch fields and provide the correct field at the exit plane of the monochromator [RCI&74].

A design based on virtual apertures was selected to minimize space charge at the monochromator exit, and to achieve the maximum possible beam current in the collision region.

A pair of deflectors mounted at the exit of the lens system is used to center the beam in the collision cell.

3.2.4.3. Collision Region

The gas was introduced as an effusive jet formed by expansion through a metallic capillary array which is composed of > 100 channels each with ~100:1 length/diameter ratio.

3.2.4.4. Analyzer Entrance Lens

The analyzer entrance lens (fig. 3.2c) accepts inelastically scattered electrons within an angular range of 2^{o} (estimated from SIMION studies) and decelerates and focuses them to the analyzer pass energy at the analyzer entrance plane.

After exploring a number of less complex designs, a seven elements lens was selected. The design incorporates three single-stage, three-element lenses placed in series

in such a manner that the object of one lens forms the image for the adjacent lens. Real exit and entrance apertures are used in order to better define the analyzer viewing cone over a range of deceleration ratios.

Both the monochromator and analyzer dispersion elements are full 180° hemispherical electrostatic deflectors since this geometry provides superior performance for electron scattering studies that are differential in both energy and angle [H71].

3.2.4.5. Detection

For all work published to date, the detector has been a channel electron multiplier. The amplified pulses from single electrons are processed using standard pulse counting techniques with a custom built combined pre-amplifier, amplifier and discriminator circuit.

3.3. McVAHRES Upgrades; The Unmonochromated Spectrometer

In order to provide greater signal at large momentum transfer, a configuration for unmonochromated operation was implemented as an upgrade. A number of upgrades have also been performed to achieve differential pumping, higher precision for the rotation mechanism, higher electron beam intensity and higher gas density in the collision region. The next paragraphs will describe in detail at these upgrades.

3.3.1 Vacuum

The pumping system consists now of two turbo-molecular pumps, the one for the main chamber and the other for the collision cell, which was implemented as part of the "new", unmonochromated spectrometer, to achieve differential pumping (fig. 3.1). Water-cooled baffles were also installed for both pumps with the goal of trapping out hydrocarbons or other impurities in the oil used in the turbo pumps (or from the fore pumps) that could lead to poor vacuum inside the chamber. The base pressure in the main chamber is 1.2×10^{-7} torr, similar to that in the neck of the collision cell pump, without baking. When a gas sample is introduced, the main chamber pressure rises to ~ 2×10^{-5} torr while the pressure in the differential pumping channel above the gas cell is ~ 6×10^{-5} torr.

The density in the collision region is estimated to be 200 times larger than that in the main chamber based on the ratio of the '**cell**' and '**non-cell**' intensities at large scattering angle (both '**cell**' and '**non-cell**' are defined in chapter 4).

3.3.2. Rotation Mechanism

Upgrading work was performed on the rotation mechanism as well. Routinely, checking for magnetic fields caused by ball bearings was performed, followed by demagnetization if necessary. The coupling between the stepping motor and the rotation gears was changed for a stiffer one that would not allow torsion. The stepping motor was changed for a more powerful one. Precise angular measurements were done and an indicator was attached to the analyser carousel pointing to the angular scale traced both

inside and outside the chamber. All these diminished the backlash from 5° to 1°. This residual backlash is automatically removed when scanning the scattering angle.

The interface and associated software were also modified to display in real time the angular position of the analyzer while in rotation. The motion can be stopped at any time and the position can be recalibrated. For this, a micro-switch positioned close to 0° ("home position") provides a fiducial input used by the computer to periodically calibrate the scattering angle scale.

The total angular range for this setup is ~ 120°, from -10° to 110°.

3.3.3. The Electron Optics

3.3.3.1. Electron Gun

A glancing incidence Auger electron gun (PHY Model 04-015) was mounted beside the monochromator (see fig. 3.1). This electron gun provided an electron beam of much greater intensity, an acceptable beam size, and modest energy resolution. The electron source is a tungsten filament. The beam is formed by a standard anode-grid-focus combination and a pair of deflector plates is mounted at the exit of the gun for beam steering. The ~ 1 mm diameter beam goes through the gas cell and either hits the side of the analyzer entrance lens, or is trapped by a current monitoring plate at large scattering angles. A phosphor coating on the entrance of the gas cell and analyzer lens allows optimization of the incident electron beam by viewing its position and shape from outside the chamber. The unmonochromated electron gun is powered by the same electronics as the monochromated gun.

The unmonochromated gun is mounted at 40° relative to the monochromated gun (fig. 3.1) and the analyzer was remounted to access scattering angles from -10° to +110° using two different mounting positions of the gas cell. It was also found that surrounding the electron gun by an aluminum shield minimizes spurious backgrounds due to non-beam electrons and reduces stray fields from the gun in the region of the lenses.

The **energy resolution** available routinely with the unmonochromated setup is ~ 0.4 eV for valence excitation and ~ 0.7 eV for core level excitation, where use of a much higher beam current (5 – 10 μA versus 0.1 – 0.5 μA) leads to space charge broadening (Boersch effect [BGH62]).

3.3.3.2. Collision Region

A copper tube was designed, constructed and mounted inside the vacuum system (fig. 3.1) to connect the additional turbo molecular pump to the collision region, thus realizing differential pumping. Fig. 3.3 shows the present performance of the differential pumping.

In order to have good differential pumping between the main chamber and the collision region, a 6 mm diameter collision cell was installed around the capillary array, thus greatly increasing the gas density in the scattering region without increasing the apparatus working pressure, and therefore the intensity of the inelastically scattered signal. The collision cell has a 2-mm entrance aperture and an exit slot subtending 50°. In order to sample the full scattering range, the gas cell is repositioned and a second 2-mm entrance aperture is used. This allows studies in the later (unmonochromated) setup

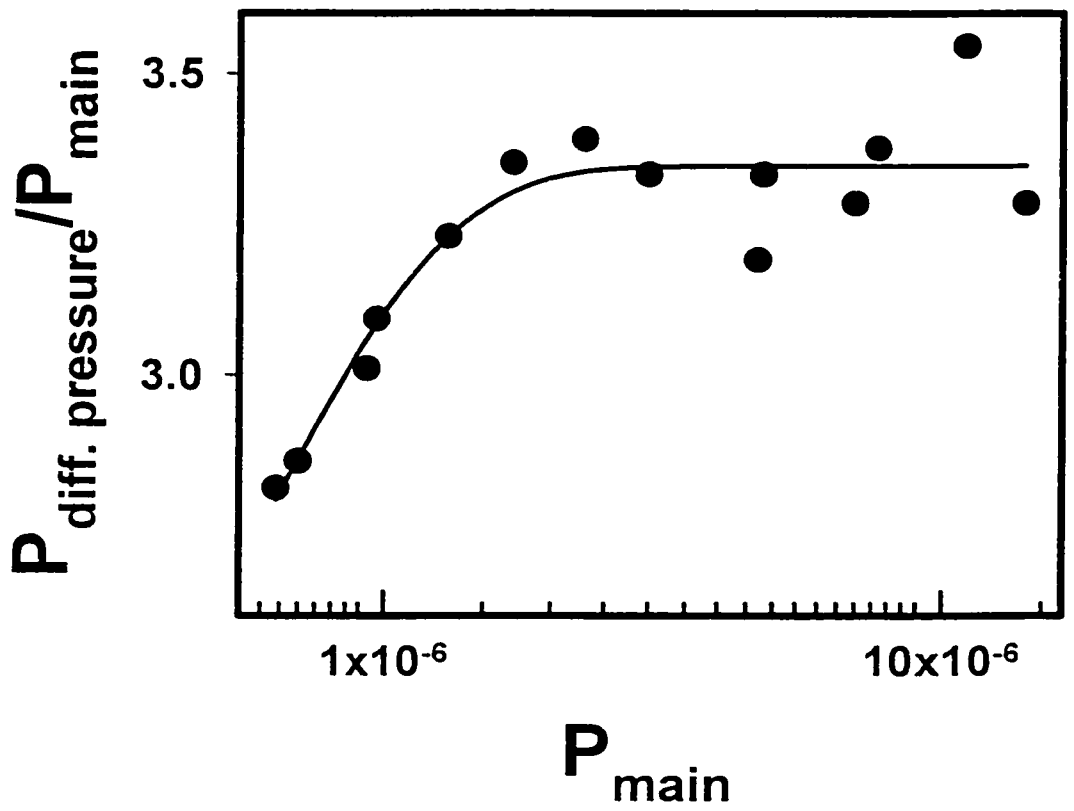

Fig. 3.3 Evaluation of the performance of the differential pumping.

from -10° to +110° degrees, with an overlap in the region of 30° - 40° between the two gas cell positions. The unmonochromated gun delivers 5 - 10 μA, whereas the original gun and monochromator only delivered 10 - 100 nA to the collision region. The combination of much higher beam current and the achievement of a much higher pressure in the collision region due to the use of the gas cell have resulted in several orders of magnitude higher scattered intensities. This provides much stronger signal at large scattering angles thereby enabling large momentum transfer GOS studies.

Historically, after installing the turbo-molecular pump assigned to the pumping of the collision region, the copper tube was mounted without the gas cell surrounding the capillary effusive jet source. The results were not satisfactory; the ratio between the pressure obtained in the collision region and the one in the main chamber was at best, unitary. What actually changed the situation was installation of the gas cell that creates a temporary trap for the molecules within the collision region. Fig. 3.4 shows a photograph of this region.

3.3.3.3. Analyzer Entrance Lens

A set of computer-controlled deflectors was mounted at the entrance of the analyzer lens system to better orient the electron beam to its path to the detector.

3.3.3.4. Detection

The detector was better positioned so that it would not be able to escape its mounting piece due to vibrational motion induced by the pumps.

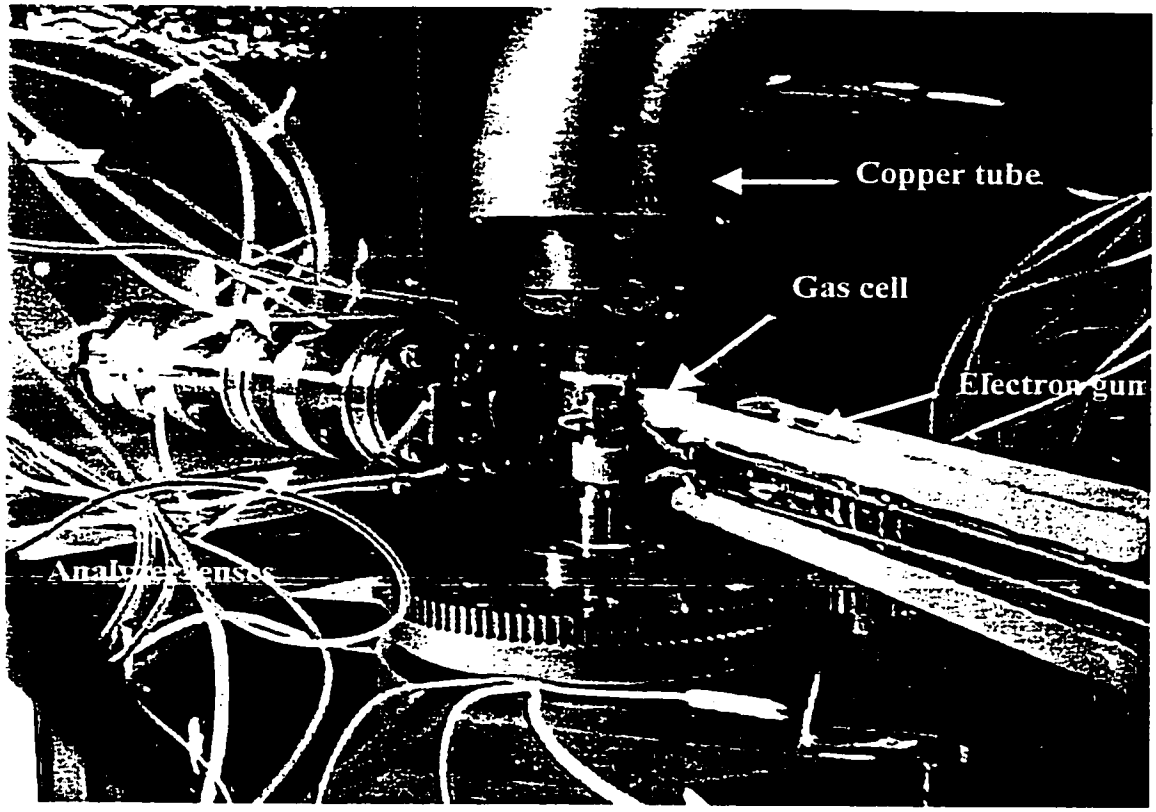

Fig. 3.4 View of the collision region, from the electron gun. Also shown are the copper tube and the analyzer lenses.

At the present time, a resistive anode position sensitive parallel detector (Quantar 3300, Quantar Technology Inc., Santa Cruz, CA, 95060) has been installed. This provides a 20-fold enhancement in signal rates over single channel detection.

A viewport was also installed in combination with an internal mirror, to "see" the electron spot as it hits the collision cell and the entrance of the analyzer, which have been previously sprayed with a phosphorescent powder.

A baking system consisting of two 300 W light bulbs was installed diametrically opposed in the main chamber. No difference was found in the quality of the vacuum or on the differential pumping when these were operated to heat the internal elements at 60°C. Most of the screws were replaced with similar ones in brass, but where stainless steel parts (screws, gears, etc) are still in place, careful demagnetization was periodically carried out, either by heating the part or by AC demagnetization. Weekly cleaning was required on the electron gun and monochromator lenses for the original setup, while general cleaning (the mounting surface and O-ring seal) was performed every time the spectrometer was open. For the unmonochromated setup, cleaning of the analyzer entrance aperture and of the gas cell, together with general cleaning was also performed each time the spectrometer was open.

3.4. Summary

An improved inelastic scattering spectrometer optimized for flexible studies of inner-shell electronic excitation has been developed. The instrumentation used to obtain GOS profiles has been described.

Chapter 4

EXPERIMENTAL PROCEDURES AND DATA ANALYSIS FOR GENERALIZED OSCILLATOR STRENGTH (GOS) DETERMINATION FROM ANGLE-RESOLVED ELECTRON ENERGY-LOSS MEASUREMENTS

This chapter presents the experimental procedures developed for McVAHRES and the data analysis used to process the electron energy loss raw spectra into generalized oscillator strength profiles. Specific examples are given to emphasize the step-by-step procedure. Comparison with literature [LKS64, SL64, SKD70, KI68] is presented for He where the GOS is well characterized.

4.1. Introduction

A systematic procedure of data acquisition and processing was developed in order to measure generalized oscillator strength (GOS) profiles. The GOS for a particular electronic transition as a function of momentum transfer (K) is called the **GOS profile**. GOS profiles are plotted in terms of K^2 rather that K since the Bethe-Born expansion (chapter 2, equation 2.28) is expressed in even powers of K. In order to obtain an

absolute GOS profile, all other factors such as pressure, incident beam current, acquisition time, etc. that determine the signal strength, are either held constant, or variations in their values are measured and taken into account. Algorithms were developed to reliably monitor and correct for changes in pressure and beam current during the acquisition period, which often extended over several days or weeks, on account of the weak signals involved. With appropriate normalization (and compensation for this normalization, when error bars are being evaluated), spectra acquired under different conditions can be combined in order to provide better statistics.

There are some specific instrumental factors that must be carefully treated. In order to have a precise value of K^2, both the impact energy and scattering angle must be well known, as the momentum transfer is calculated using these experimental parameters. The gas pressure and incident beam currents must be monitored and kept relatively constant over the acquisition period. Fluctuations in these quantities will reduce the precision of the results.

4.2. Spectral Acquisition Methods

Two different methods of acquiring data in order to compute the GOS profiles are discussed here: "**energy scan**" and "**angle scan**" modes [EFT&99]. They will be discussed separately in the following sections. Both methods are carried out using DOS-based acquisition software, McVSpec, written in FORTRAN. Thus, it is possible to collect spectra in constant scattering angle mode by scanning the energy loss, or in constant energy loss mode by scanning the scattering angle.

Before starting systematic scanning, the first thing to check is the correct "zero degree" position. This can be done by scanning at a fixed particular energy loss a range of scattering angles that comprises the estimated "zero degree" position. If the tuning of all lenses is correct and the mechanical alignment of the system gun-cell-analyzer is within limits, the recorded spectrum should show a maximum corresponding to the searched position. After this was checked and (if necessary) the software re-calibrated, the spectral acquisition can start in a systematic way.

Note also that the spectrometer operates in a constant final energy mode:

$$E_{impact} = E_{loss} + E_{final} + E_{pass}^{analyzer} \qquad (4.1)$$

where E_{impact} is the impact energy, E_{loss} is the energy loss, E_{final} is the final energy and $E_{pass}^{analyzer}$ is the pass energy of the analyzer.

4.2.1. "**Energy Scan**" Mode

In this mode, three different types of high quality, full energy loss spectra are recorded at a relatively small number of scattering angles. The number of spectra is set in the acquisition routine, together with the energy step, the dwell time and the energy range to be scanned. The scattering angle is mechanically set to the desired value. Next, the angle is periodically incremented manually or the computer can set it and the entire scanning process is resumed for the newly set angle.

The three modes are:

a) "**cell**" spectrum

b) "**non-cell**" spectrum

c) "**non-gas**" spectrum

a) In the "**cell**" measurements (the conventional spectrum), the high sample gas density is introduced in the collision cell to a pressure P_{gc} (typically ~ $6x10^{-5}$ torr). The main chamber pressure is P_{mc}. These spectra contain mainly the signal from high density of gas inside the cell.

b) In the "**non-cell**" measurements, the sample is introduced outside of the collision cell through an additional inlet at the same main chamber pressure P_{mc}. These spectra are acquired to subtract the signal coming from scattering by gas outside the collision cell.

c) In the "**non-gas**" measurements, no sample is introduced. This signal, which originates from residual gas, the gas cell and other parts of the apparatus as well as detector background, is present in both the cell and non-cell spectra.

The energy scales of all recorded spectra are calibrated using a well-known transition energy as reference.

Next, the spectra are normalized to the dwell time (time per energy point), the number of scans and the electron beam current. This data is recorded in the spectral file as well. The output file is a multicolumn file, displaying both the raw data and the normalized data.

When a set of spectra for the same angle are grouped together, after individual calibration, they are added and the sum-spectrum is normalized to the dwell time, the total number of scans and the current. This procedure ensures that the statistical factors are correctly treated.

At each scattering angle, the "**non-gas**" spectra are subtracted from the **cell** and "**non-cell**" spectra. The corrected spectrum used for subsequent processing is obtained from the difference ("**cell**" – "**non-cell**") and normalized to the pressure in the collision cell during the "**cell**" measurements. This corrected spectrum contains only the contribution from the main gas density in the collision cell.

Fig. 4.1 shows "**cell**", "**non-cell**" and "**non-gas**" C 1*s* spectra of COS recorded at 4° and an impact energy of 1623 eV, along with the corrected spectrum.

The BAN data analysis program is used to prepare each overlap corrected, K^2 dependent, energy spectrum and angle spectrum for fitting.

With the goal of GOS measurements, it is very important that high quality data is recorded. The time needed depends on the signal intensity. At small scattering angles a few tens of scans are usually enough but at higher scattering angles (> 16°) this number will usually increase non-linearly to a few hundred scans. Therefore, the stability of the signal is a very important issue as the spectral acquisition at high angle might last a few days.

4.2.2. "**Angle Scan**" Mode

While the high energy point density of the energy scan data gives precise integrated signals for each peak at a small number of momentum transfers, these spectra could only be obtained over a sparse K^2 mesh in a reasonable time.

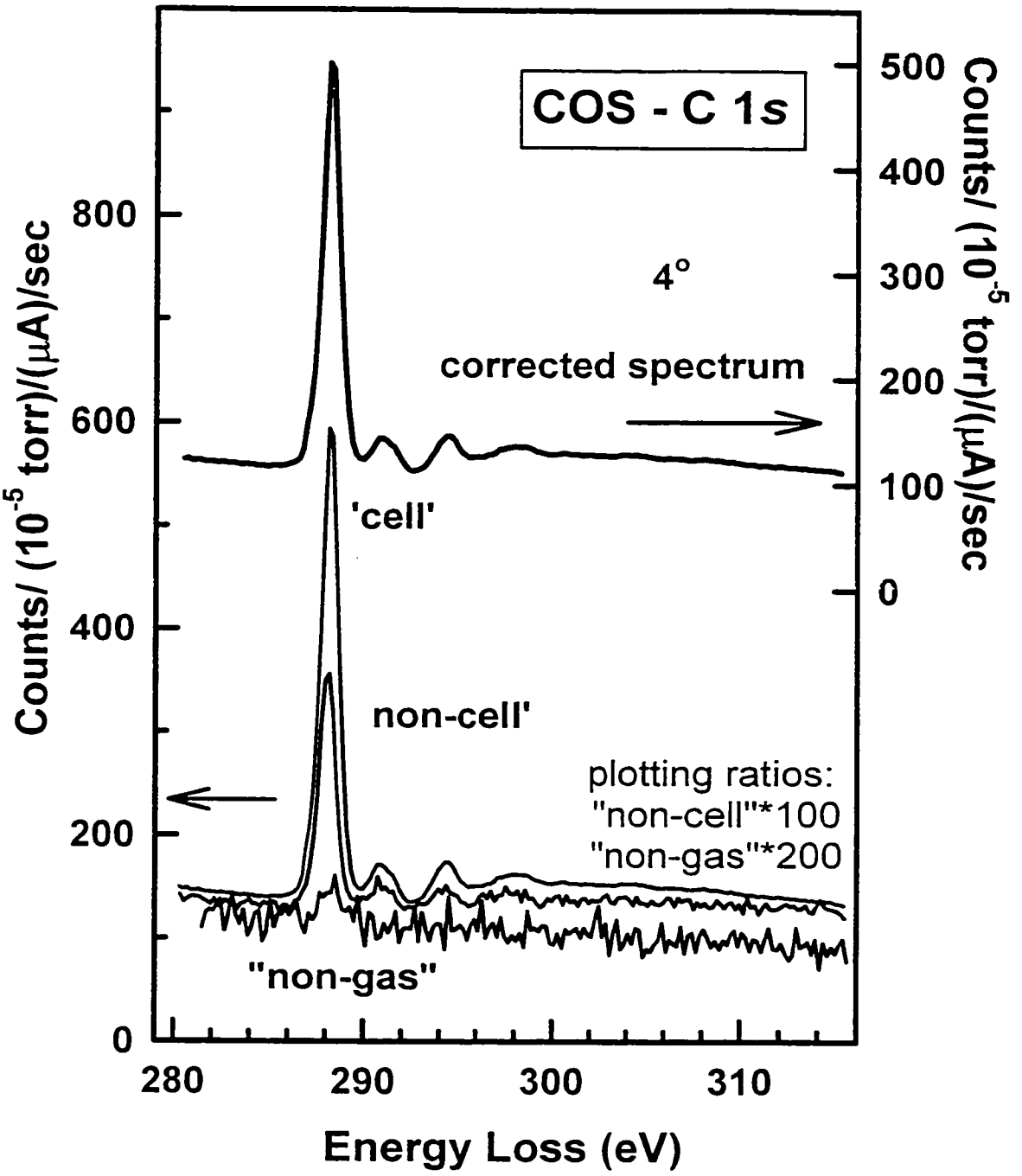

Fig. 4.1 Cell, non-cell and non-gas as-recorded spectra for C 1*s* excitation of COS measured at 4° with a final electron energy of 1300 eV. Each spectrum has been normalized as mentioned in the text.

In order to sample the GOS profiles at more K^2 values we have also carried out measurements in the alternate "**angle scan**" mode.

In "**angle scan**" mode, the signal-averaged measurements are carried out using scattering angle rather than energy loss as the control parameter. However, since the speed of mechanical scanning is limited, we optimize the acquisition process by measuring signals at a number of energy loss values at each scattering angle.

The acquisition setup will contain again the desired energy range, the dwell time, the energy step as well as the angular range to be scanned. Usually, the energy points are chosen so that there will be a high sampling where the region of interest is, while just a few points are taken outside it. Enough points should be planned to be recorded for the background. The algorithm carries the scanning from the highest scattering angle to the lowest, by automatically changing the angle. It also enables a variable dwell time as a function of the scattering angle; thus, this time will be longer at large scattering angles and shorter at low scattering angles. Together with the electron current and the cell pressure, the dwell time is recorded in the file containing the spectrum. An example of raw data from an angle scan is given in **fig. 4.2**.

As in the "**energy scan**" mode, the energy scales of all spectra are next calibrated using a well known transition energy as reference. If a series of spectra are to be added, then this is when this operation should be done, as mentioned for the "**energy scan**" mode. Next, the spectra are normalized to the number of scans acquired, the specific dwell time and the electron beam current.

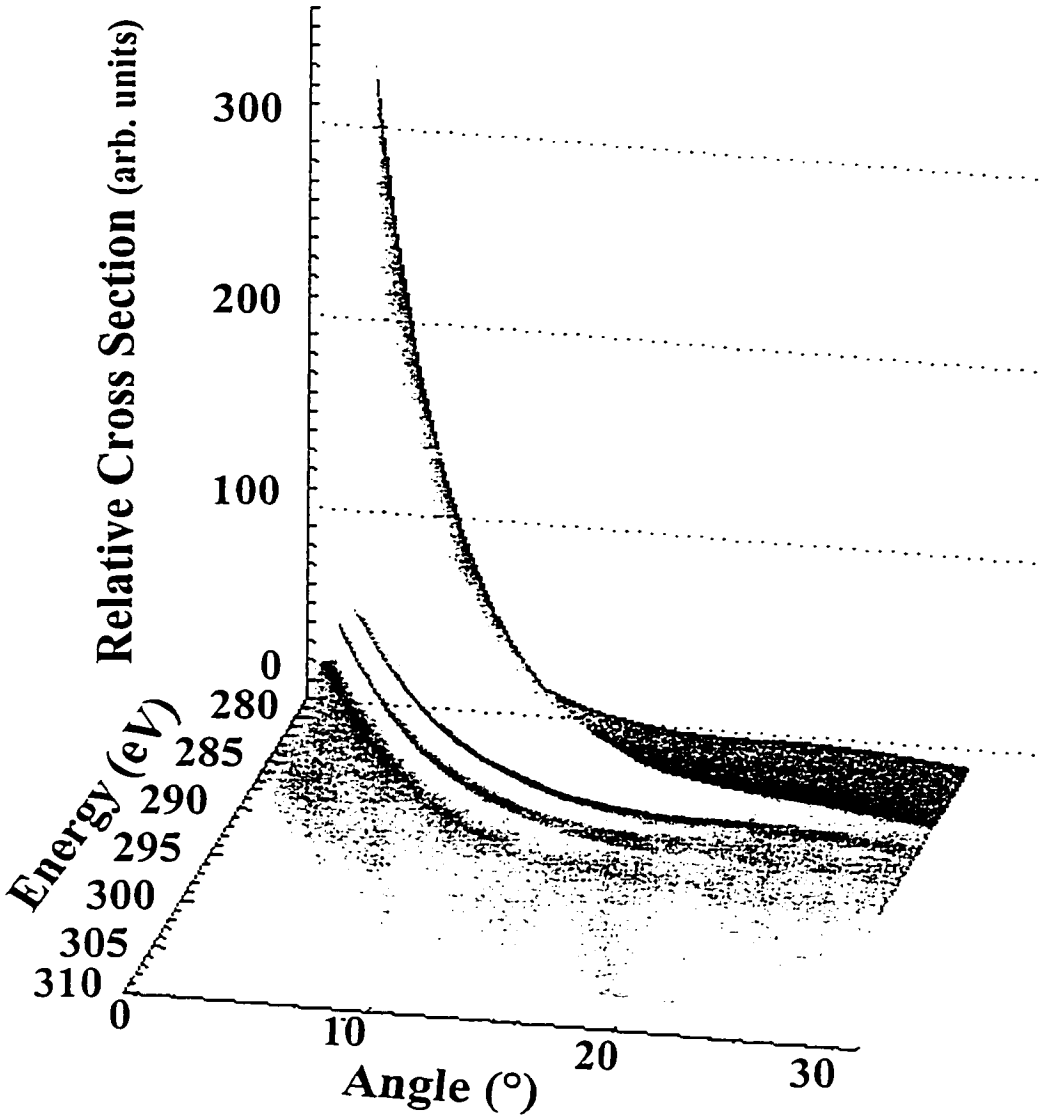

Fig. 4.2 Angular dependence of the C 1*s* excitation of COS as measured in "**angle scan**" mode.

For a fixed acquisition period, the angle scan mode provides a means of achieving a much denser sampling of the scattering angle (and thus momentum transfer), thereby providing more detailed GOS profiles.

However, high quality "**energy scan**" mode spectra are essential to ensure proper spectroscopic analysis at all momentum transfers and to allow checks for systematic errors. If the spectrometer operates with the correct and stable tuning (i.e., no insulating contamination of the spectrometer surfaces or beam degradation over the period of the measurements), the normalized and calibrated "**angle scan**" and "**energy scan**" data recorded for the same energy loss range, the same K^2, and the same impact energy should be the same within mutual experimental uncertainties.

4.3. Deriving the Absolute GOS

The relative cross-section for each resolved electronic transition was derived from the spectra acquired in the "**energy scan**" and "**angle scan**" modes as follows.

4.3.1. The Background Subtraction

The underlying ionization continuum background is first removed from the "clean spectrum" by subtracting a smooth curve determined from a curve fit of a binomial function ($a(E\text{-}c)^d$) to the continuum structure below the onset of core excitation. After this operation is done for all energy and angular spectra, it is useful to compare them by overplotting one on top of the other. A smooth decrease in intensity has to be observed

as the scattering angle increases. This is one way of insuring that the background subtraction is done well.

4.3.2. Multi-File Fit Analysis

The background subtracted spectra are next fitted to a combination of Gaussian peak shapes and an error function representing the ionization threshold. For the 4° spectrum, the signal intensity is high and thus the statistics are very good, therefore the model for the future multi-fit is built using this spectrum. This model for the fitting, i.e., establishing the number and positions of the fit features, is determined using BGAUSS. The fit routine requires the input of the width, energy position and amplitude of each line comprising the overall fit. This model should be connected to the spectroscopic meaning. In addition, it is possible (and recommended) to fix at a constant value and/or correlate any of these parameters during the fitting routine. The output of the routine lists the widths, energy positions, amplitudes and in the case of the Gaussian lines, the area.

The spectra taken at all other angles are subsequently fit simultaneously to this fit model, using a constrained multi-parameter optimization procedure MGAUSS [ATH&92].

After an acceptable multi-file fit for all "**energy scan**" spectra, the "**angle scan**" spectra are added and the fit is repeated, such that the final result is determined by a unified treatment of the "**energy scan**" and "**angle scan**" data.

It is critical to have accurate energy calibration of all spectra, since the energy positions and the widths of Gaussians are kept constant in the multi-file fitting procedure.

The output file contains all peak areas associated with each feature representing the geometry-distorted relative cross-sections. They are determined for each feature at all scattering angles at which energy-scan spectra are acquired.

An alternate way that was used in some cases adopted the multi-fit procedure just described for the "**energy scan**" spectra to obtain the geometry-distorted relative cross sections. Next, the "**angle scan**" data was matched with the "**energy scan**" data at typically 4° or 8°. A factor was thus calculated and applied to convert all intensities of peaks in the "**angle scan**" spectra into areas.

Figures 4.3 and **4.4** illustrate this procedure through a step-by-step example of spectra analysis and data manipulation for the C 1*s* edge in COS.

4.3.3. The Geometrical Correction

Next, the peak areas associated with each feature at all different K^2 values are submitted to a **geometrical correction (fig. 4.5)** [BT81], to obtain the geometry-corrected relative cross-sections, necessary to evaluate the relative GOS.

This correction takes into account two factors: first, the changes in geometric overlap caused by the change in the size and shape of the interaction region with the scattering angle (the collision path length is longer at small angles) and second, the existence of a non-uniform gas distribution inside the collision cell and approximated as a Gaussian distribution.

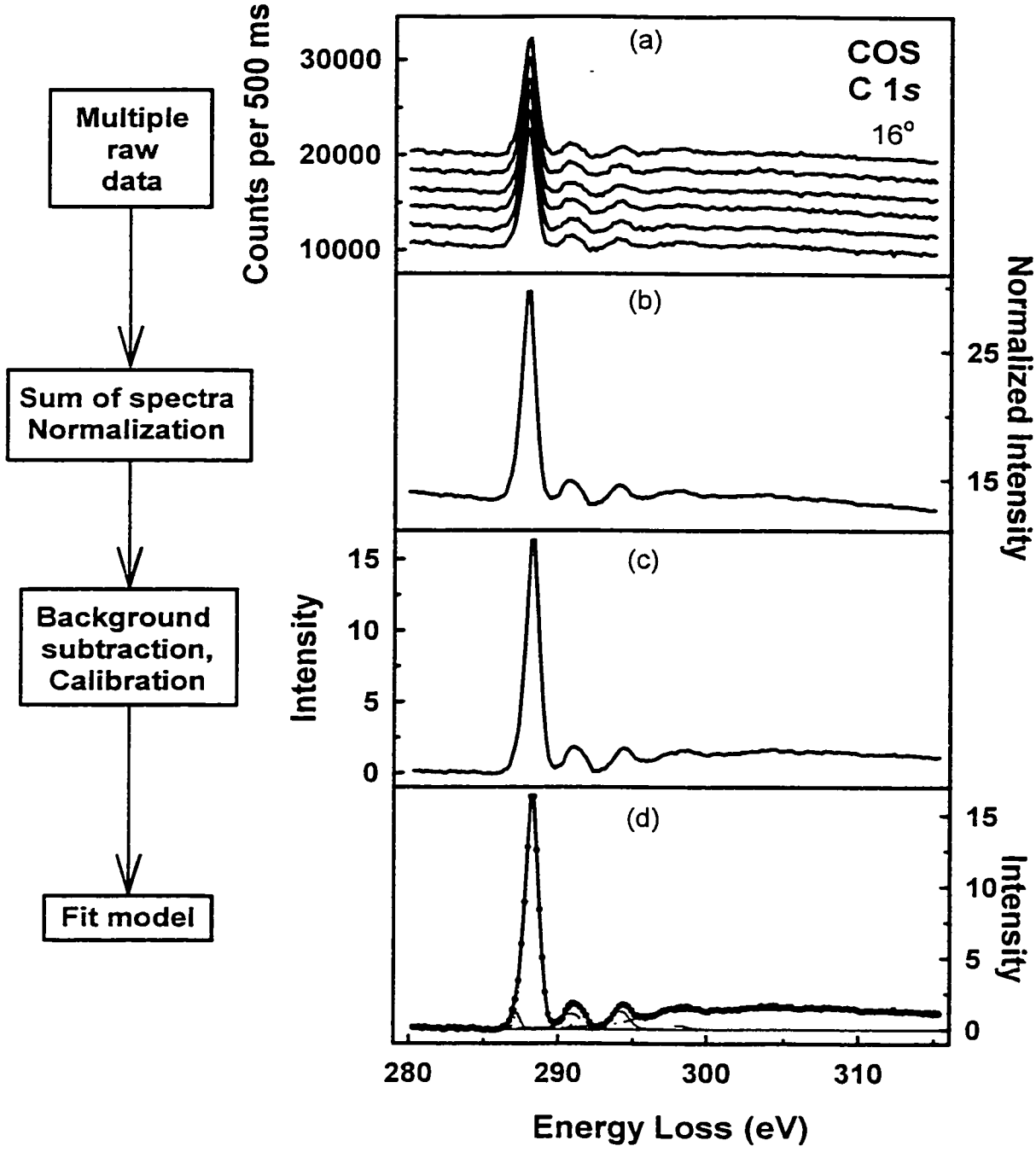

Fig. 4.3 Step-by-step example of spectral analysis: (a) stack of raw spectra; (b) sum of raw spectra, normalization as described in the text; (c) background subtraction; (d) fit analysis of all features

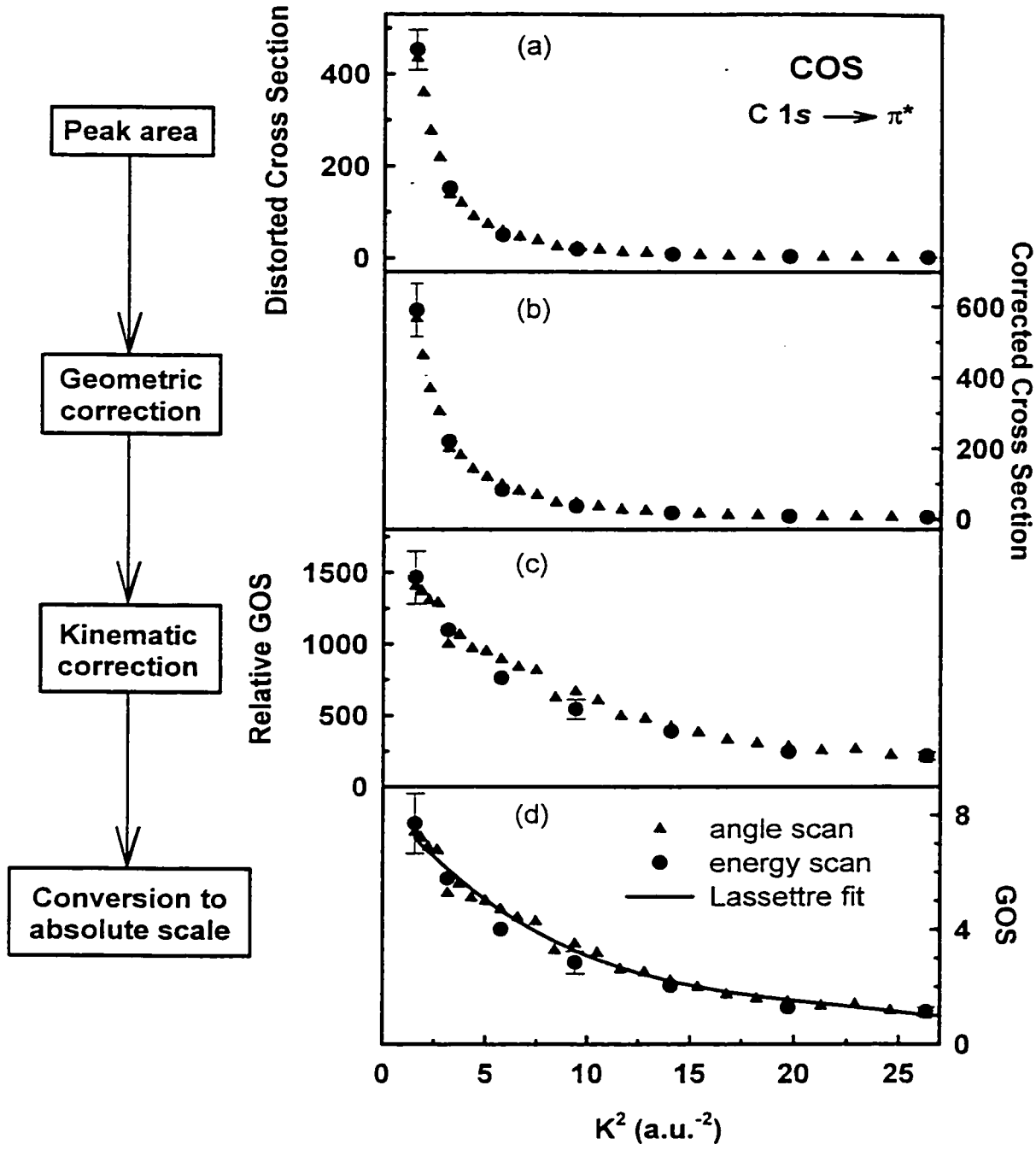

Fig. 4.4 Step-by-step example of data analysis for GOS: (a) uncorrected cross section; (b) geomety corrected cross section; (c) relative GOS after kinematic correction; (d) conversion to absolute GOS.

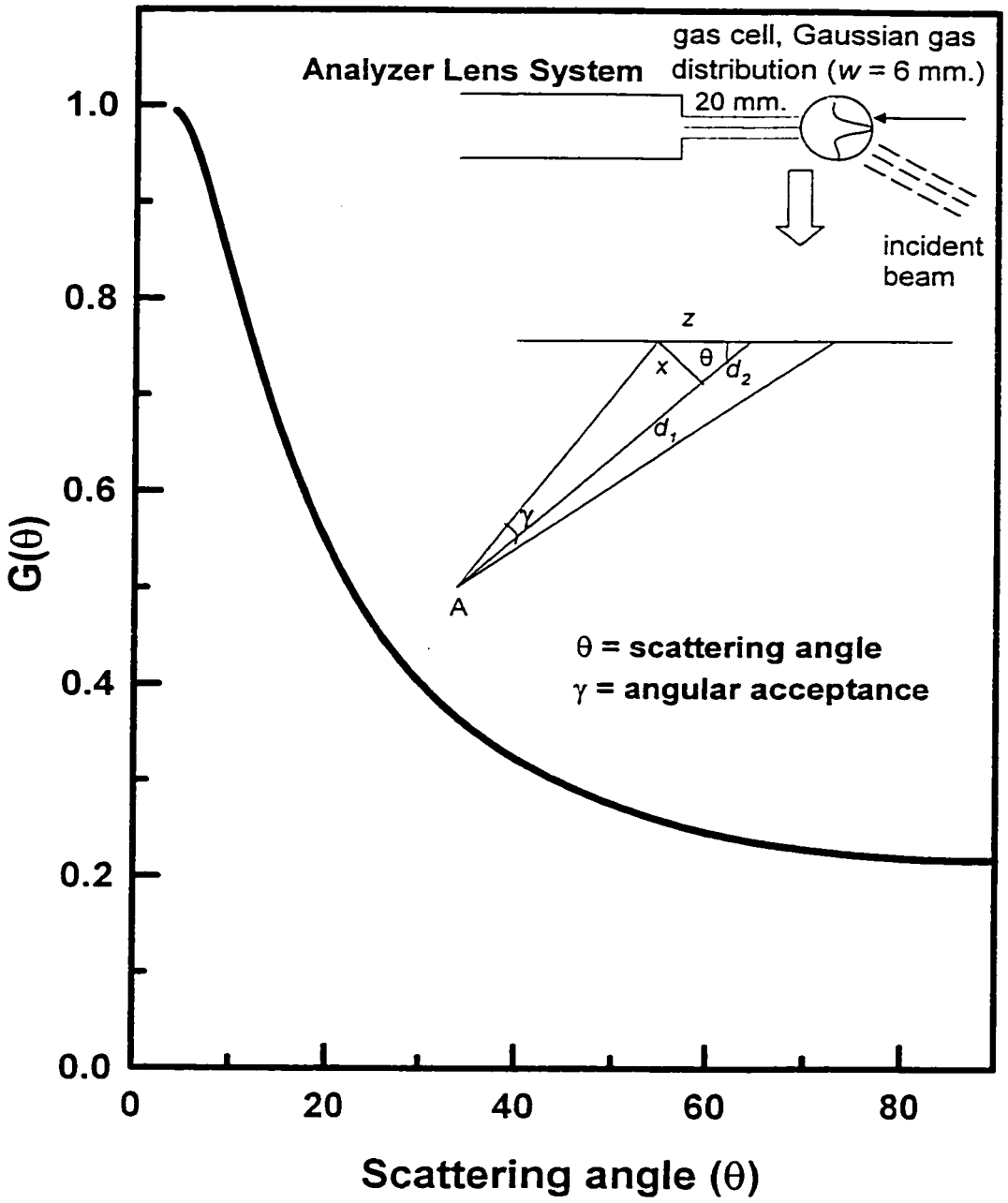

Fig. 4.5 Geometric correction function used to correct the angular dependence of the overlap of incident beam, analyzer viewing cone and spatial variation of the gas density. The insert shows the geometry used to derive the analytical form for the correction factor.

There are several approximations involved in generating the geometric correction as it was obtained. The entrance of the analyzer is assumed to be a point (A), the incident and scattered flux are assumed to be parallel beams (z direction), the gas density in the cell is assumed to be a Gaussian distribution of $w = 6$ mm width and the acceptance angle 2γ for the analyzer is assumed to be 4°.

In fig. 4.5, the following notations are used:

θ = scattering angle

2γ = analyzer angular acceptance

z = 1/2 acceptance length of the beam

Thus, we have the following set of relations:

$$d = d_1 + d_2 \tag{4.2a}$$

$$\tan\gamma = \frac{x}{d_1} \tag{4.2b}$$

$$\tan\theta = \frac{x}{d_2} \tag{4.2c}$$

$$\sin\theta = \frac{x}{z} \tag{4.2d}$$

$$\cos\theta = \frac{d_2}{z} \tag{4.2e}$$

From eqns. (4.2a), (4.2b) and (4.2e) we have:

$$x = d_1 \tan\gamma = (d - d_2)\tan\gamma = (d - z\cos\theta)\tan\gamma = d\tan\gamma - z\cos\theta\tan\gamma \tag{4.3}$$

By equating (4.2d) and (4.3):

$$z\sin\theta = d\tan\gamma - z\cos\theta\tan\gamma \tag{4.4a}$$

$$z(\sin\theta + \cos\theta\tan\gamma) = d\tan\gamma \tag{4.4b}$$

$$z = \frac{d\tan\gamma}{\sin\theta + \cos\theta\tan\gamma} \tag{4.4c}$$

Next, the Gaussian function that represents the gas distribution in the intersection volume is written as a function of $z = f(\theta)$, as:

$$f(z) = A\exp\left[-\frac{z^2\ln 2}{\left(\frac{1}{2}w\right)^2}\right] \tag{4.5}$$

where w = 6 mm (Gaussian function width), d = 20 mm, γ= 2° and A = amplitude factor used to normalize the geometrical correction to a maximum value of 1.

The geometric correction as a function of the scattering angle is then obtained by integration of the Gaussian function $f(z)$.

The application of the geometrical correction to the peak areas associated with each feature, i.e., the peak areas divided by the geometric function, gives the geometry corrected relative cross section, necessary to evaluate the relative GOS.

This correction function is specific to the McVAHRES gas cell. Other corrections must be developed for different spectrometers [BT81]. For example, the earlier GOS studies [TFT&95, ETH99] used an effusive jet to introduce the sample and thus required a very different geometric correction procedure.

4.3.4. The Relative GOS

The last step before getting the values for the relative GOS as a function of K^2, is to apply the Bethe-Born kinematic correction factor, $(k_0/k_1)K^2$ $(E/2)$ by multiplying the set of values obtained after the geometrical correction was applied.

4.3.5. The Absolute GOS

The scale factor which is used to convert relative to absolute GOS may be determined by extrapolating the relative GOS values for a determined feature to $K^2 = 0$, and then deriving the factor from the match of this relative optical oscillator strength (OOS) to the literature OOS. The same scaling factor is used to derive the absolute GOS from the relative GOS for all features. In the work presented in this thesis, the OOS was determined in various ways as it will be described for each case, therefore it is important to select the best suited value for the case.

4.3.6. The Lassettre Series

The modified Lassettre series [L65, DL75], provides a semi-empirical connection between measured GOS profiles and the coefficients in equation :

$$f(K,E) = \frac{1}{(1+x)^6} f_0 \sum_{n=0}^{m} \frac{f_n}{f_0} \left(\frac{x}{1+x} \right)^n \qquad (4.6)$$

where $x = K^2 / [(2IP)^{1/2} + (2|IP - E_n|)^{1/2}]^2$, IP is the ionization potential and E_n is the excitation energy of a particular discrete transition.

Quantum mechanically, f_n are related to linear combinations of the respective multipole matrix elements (chapter 2, equations 2.28, 2.29). *f(0, E)* is the optical oscillator strength (OOS) value, f_0.

The original Lassettre series was developed to quantitatively deduce precise OOS values by extrapolating GOS data measured by angle-resolved EELS, to the zero K limit. The second term, f_1, in the series is related to the quadrupole matrix element and the product of dipole and octupole matrix elements (chapter 2, equation 2.29) [H79]. Higher order terms give measures of other electric multipole contributions.

In practice, the summation is usually limited to $m = 3$ since including larger terms increases the error in lower terms, making their values unreliable.

A direct electric quadrupole transition would be characterized by a positive f_1 term. In contrast, f_1 for an electric dipole transition is negative since the product of the dipole and octupole matrix elements is larger and positive. This results in a maximum for the quadrupole transitions and a continuous drop off for the dipole transitions.

4.3.7. Error treatment

Experimental uncertainties for the derived GOS values were determined from the energy scan data, taking into account contributions from the uncertainties in the momentum transfer (K^2) and in the peak area. The uncertainty in K^2 is determined from the uncertainty in the scattering angle, ±0.25°. The uncertainty in the peak area includes uncertainty in the gas pressure (~ 2%), and the incident beam current (~ 1%), along with contributions from the statistical precision of the data, all added in quadrature. The total

uncertainty in the GOS for each K^2 value is then determined by adding in quadrature the uncertainty in the peak area and the uncertainty in relative GOS arising from the uncertainty in K^2.

It should be noted that significant systematic errors could be associated with various aspects of the data treatment.

A proper geometrical correction is important since, if the geometrical correction is not applied, the intensity of the signal at low scattering angles is substantially overestimated. The kinematic correction relating relative cross-section and relative GOS is a further possible source of systematic error if there is undetected bias in the conversion of experimental parameters to momentum and momentum transfer. Finally, application of equation 2.23 (chapter 2) and the whole GOS concept assumes that the first Born approximation (FBA) is valid [I71]. From valence shell GOS measurements this is expected to breakdown in the range of K^2 we have studied. However, comparison to the theoretical results computed within the FBA suggests that for inner shell GOS, the FBA may be valid to much larger K^2 values [ETH&99].

4.4. GOS of He

To confirm the validity of our data treatment methodology and to ensure that the experimental GOS were correctly measured without distortion by various possible instrumental artifacts, we used these procedures to record the well known GOS profiles for excitation to the ($1s^{-1}$, $2s$) and ($1s^{-1}$, $2p$) states at 20.6 and 21.2 eV of He. The GOS

profiles obtained matched the literature results [LKS64, SL64, SKD70, KI68] within mutual experimental uncertainties.

Experimentally, a series of electron energy-loss spectra were acquired in "**energy scan**" mode, from 3° to 38°, one degree apart, covering a range $K^2 = 0.28 - 40$ a.u.$^{-2}$. The same acquisition setup was kept for "**non-jet**" measurements. The energy loss scales were calibrated using the He $1s \rightarrow 2p$ transition (21.22 eV).

The relative GOS distributions are obtained by dividing the peak areas derived with MGAUSS by the geometrical correction.

The scaling factor converting the relative GOS to absolute values was determined by graphically extrapolating the relative GOS for the He $1s \rightarrow 2p$ transition and then selecting the factor to match the relative OOS to the OOS reported in the literature (0.26) [SL64].

As expected, the He $1s \rightarrow 2p$ dipole allowed transition is fading away at higher scattering angles, while the He $1s \rightarrow 2s$ dipole forbidden transition is increasing dramatically, to become the dominant feature of the spectrum at high K^2. **Fig. 4.6** shows this behavior for scattering angles ranging from 3° to 14°.

The GOS profiles obtained match with all the previous data reported in the literature [LKS64, SL64, LSD70, KI68], as seen in **fig. 4.7,** which compares the theoretical (squares) and experimental (diamond, triangle down) results and the corrected GOS values (simple line and circles).

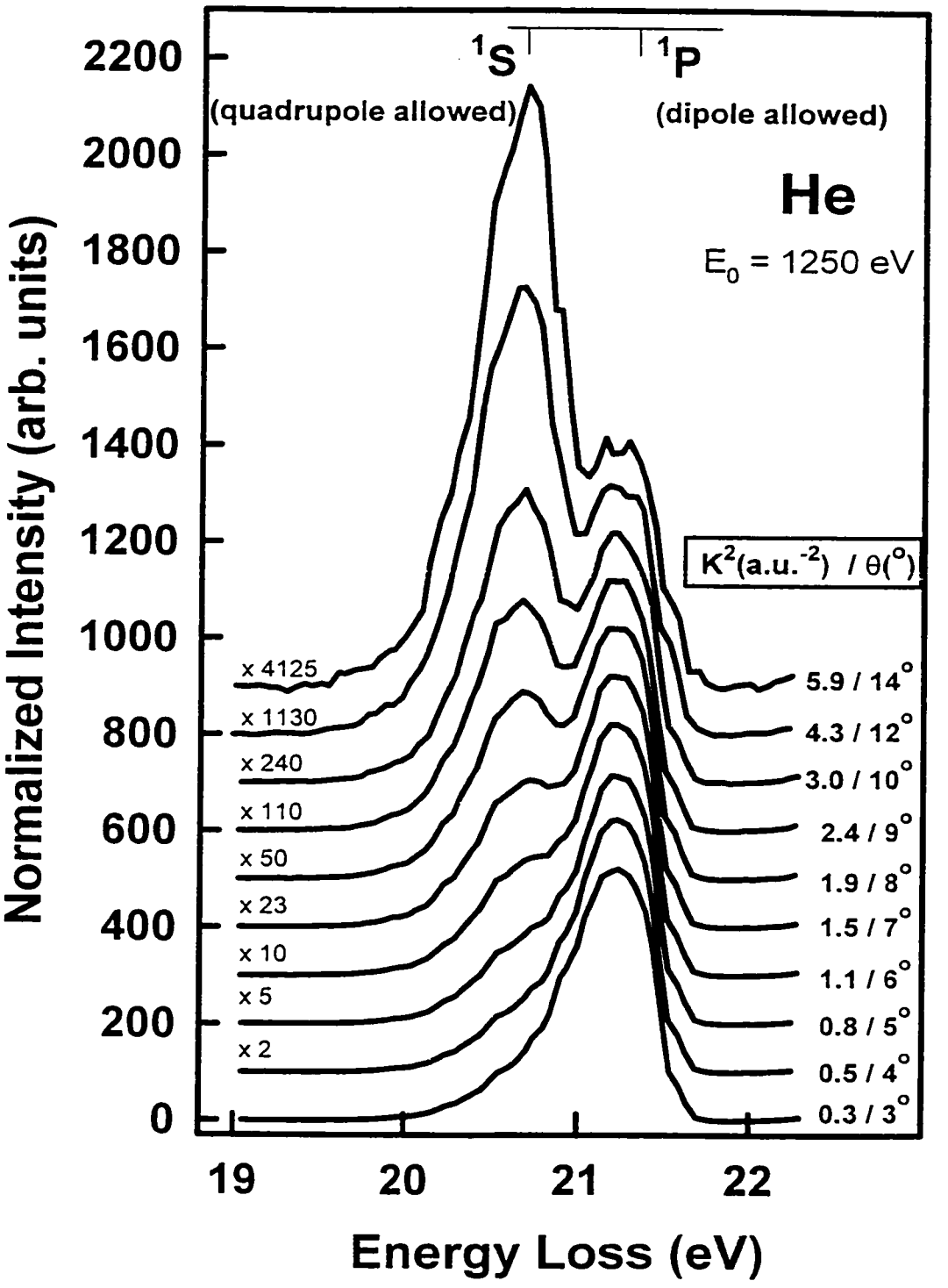

Fig. 4.6 Background subtracted energy loss spectra of He.

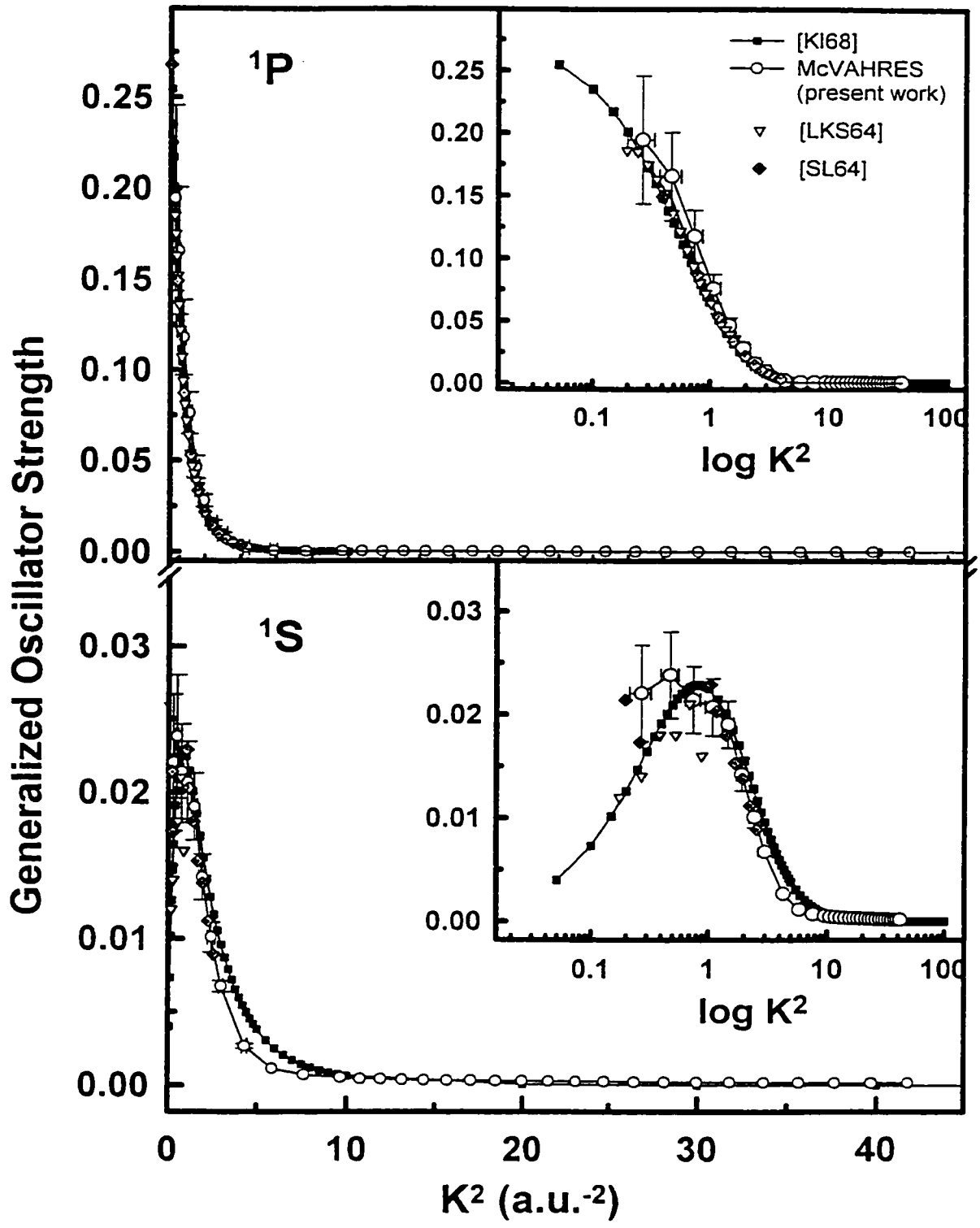

Fig. 4.7 GOS curves for He $1s \rightarrow 2p$ and $1s \rightarrow 2s$ electronic transitions.

4.5. Summary

This part of the thesis describes the methodology employed to derive the absolute GOS curves. The step-by-step procedure is described and specific examples are given. A geometric correction specific for McVAHRES and the gas cell used for the experimental measurements is presented. Since the scattered geometry corrected curves agree so favorably with the literature experimental and theoretical curves we have confidence that this correction must be applied to all data obtained using the present collision cell structure. Note that the earlier GOS studies on McVAHRES using SF_6 [FTT&95, TFT&95] were obtained without the gas collision cell and thus a different experimental correction procedure was needed.

Chapter 5

INNER-SHELL ELECTRON ENERGY-LOSS SPECTROSCOPY OF SF_6 AT VERY HIGH MOMENTUM TRANSFER; GENERALIZED OSCILLATOR STRENGTHS FOR INNER-SHELL EXCITATION

Electron energy loss spectra recorded with variable scattering angles and impact energies corresponding to momentum transfers up to K^2 = 113 a.u.$^{-2}$ have been used to explore non-dipole transitions to S 2s and S 2p core excited states. A little known, non-dipole excitation at 181 eV is found to become the dominant S 2p spectral feature in EELS spectra recorded at large momentum transfer (K). A variable impact energy, fixed-K study shows that the first Born approximation breaks down under low impact energy conditions. An in-depth characterization of the generalized oscillator strength (GOS) distributions for S 2p, S 2s and F 1s excitation in SF_6 up to very high momentum transfer is also presented. The GOS profiles for F 1s excitation of SF_6 are reported for the first time.

5.1. Introduction

A considerable number of studies have focussed on SF_6 [HBV78, HB78, YML93, TFT&95, FTT&95, HEF&98] since it has high symmetry (and thus its spectroscopy

features electric dipole forbidden processes) and since it is a prototype of molecules exhibiting potential barrier phenomena. In fact the first positive identification of a non-dipole transition in the inner shell electron energy loss spectrum of a molecule was that of the (S $2p$ $(t_{1u})^{-1}$, $6t_{1u}$) "A state" at 177 eV in SF_6 [HBV78].

This chapter will document a dramatic observation, that, under certain scattering conditions, the electric dipole forbidden transition S $2p$ at 181 eV ("B state") is the strongest S $2p$ energy loss signal. This is surprising since this signal, which incorporates several non-dipole excitations, was first documented in the open literature only recently in our first variable momentum transfer study of SF_6 [TFT&95].

This chapter also reports an extensive study of the GOS profiles for inner-shell excitation of sulfur hexaflouride (SF_6).

SF_6 is a very useful system to obtain a detailed understanding of inner shell excitation spectroscopy and core state dynamics. SF_6 belongs to a family of molecules in which a central atom forms polar bonds with two or more electronegative atoms as in BF_3, $SiCl_4$, etc.[D72]

Nefedov [N70] first proposed the existence of a potential barrier in molecules like SF_6. Initially, this barrier was attributed to a net repulsive interaction in the vicinity of the electronegative atoms in the molecule [D72, N70], but modern understanding [DD75, D76, DPS87, S92] attributes the barrier to a centrifugal potential associated with high angular momentum of the ejected photoelectron since the continuum resonances appear at specific energies in selected angular-momentum partial waves of the outgoing electron in the final state.

5.2. Spectroscopy at very high momentum transfer

The S $2p$ and S $2s$ core excitation spectra of SF_6 are dominated by one-electron excitations to states in which the core electron is promoted to levels associated with four virtual valence orbitals - a_{1g}, t_{1u}, t_{2g}, e_g -, confined by a pronounced barrier to the inner-well region of a double-well potential [N70, BHK&72, D72].

Under dipole conditions (photoabsorption [N70, BHK&72, D72, HSD&93] or small momentum transfer EELS [HB78]), one observes only T_{1u} final states, which are those associated with S $2p$ excitation to the a_{1g}, t_{2g} and e_g unoccupied levels, or S $2s$ excitation to the t_{1u} level. If the energy loss spectra are measured at higher scattering angles [YML93, TFT&95, FTT&95] or reduced impact energy [H86], the selection rules are relaxed and the spectra exhibit new features associated with dipole forbidden core excitations.

The non-dipole S $2p(t_{1u}) \rightarrow 6t_{1u}$ excitation leads to 4 separate final states (of A_{1g}, E_g, T_{1g} and T_{2g} symmetry). While the lowest energy (S $2p^{-1}$, $6t_{1u}$) A_{1g} state has been known for many years [HB78], and even identified optically [HSD&93], it was only through systematic momentum transfer studies, combined with *ab initio* calculations [TFT&95] that a weak signal at 181 eV was associated with the E_g and T_{2g} states from S $2p(t_{1u}) \rightarrow 6t_{1u}$ excitation. This signal, labeled the "**B-state**" [TFT&95], was first observed by King and Harrison [H86] who had assigned it to a non-dipole state associated with S $2p(t_{1u}) \rightarrow t_{2g}$ excitation.

Also, in order to experimentally investigate the break-down of the Born approximation, a series of spectra was measured in which both scattering angle (25°–51°) and final electron energy (1600 to 300 eV) were varied simultaneously in order to maintain a constant $K^2 = 25$ a.u.$^{-2}$.

5.2.1. S 2*p* spectrum

Fig. 5.1 compares the background subtracted S 2*p* spectrum recorded at small momentum transfer (4°, $K^2 = 0.9$ a.u.$^{-2}$), with that recorded at extremely high momentum transfer (62°, $K^2 = 113$ a.u.$^{-2}$). **Table 5.1** list the peak energies used in the data analysis, along with their spectral interpretation [FTT&95, BGH62]. The present study greatly extends the range of momentum transfer investigated since the previous study [TFT&95] was limited to scattering angles below 16°.

The dipole-regime S 2*p* spectrum is dominated by three bands, corresponding to excitation to the dipole coupled states arising from S 2*p* excitation to the a_{1g}, t_{2g} and e_g virtual valence orbitals. Under strong non-dipole conditions, there are two additional bands ("**A**" and "**B**") which are associated with non-dipole coupled states arising from S 2*p* excitation to the t_{1u} virtual valence orbital.

At strongly non-dipole conditions, the relative intensity of the second dipole forbidden feature increases dramatically to the extent that, above $K^2 \sim 40$ a.u.$^{-2}$, the "**B state**" becomes the most intense spectral feature, even stronger than the $T_{1u}(t_{2g})$ transition which dominates the dipole spectrum [ETH99].

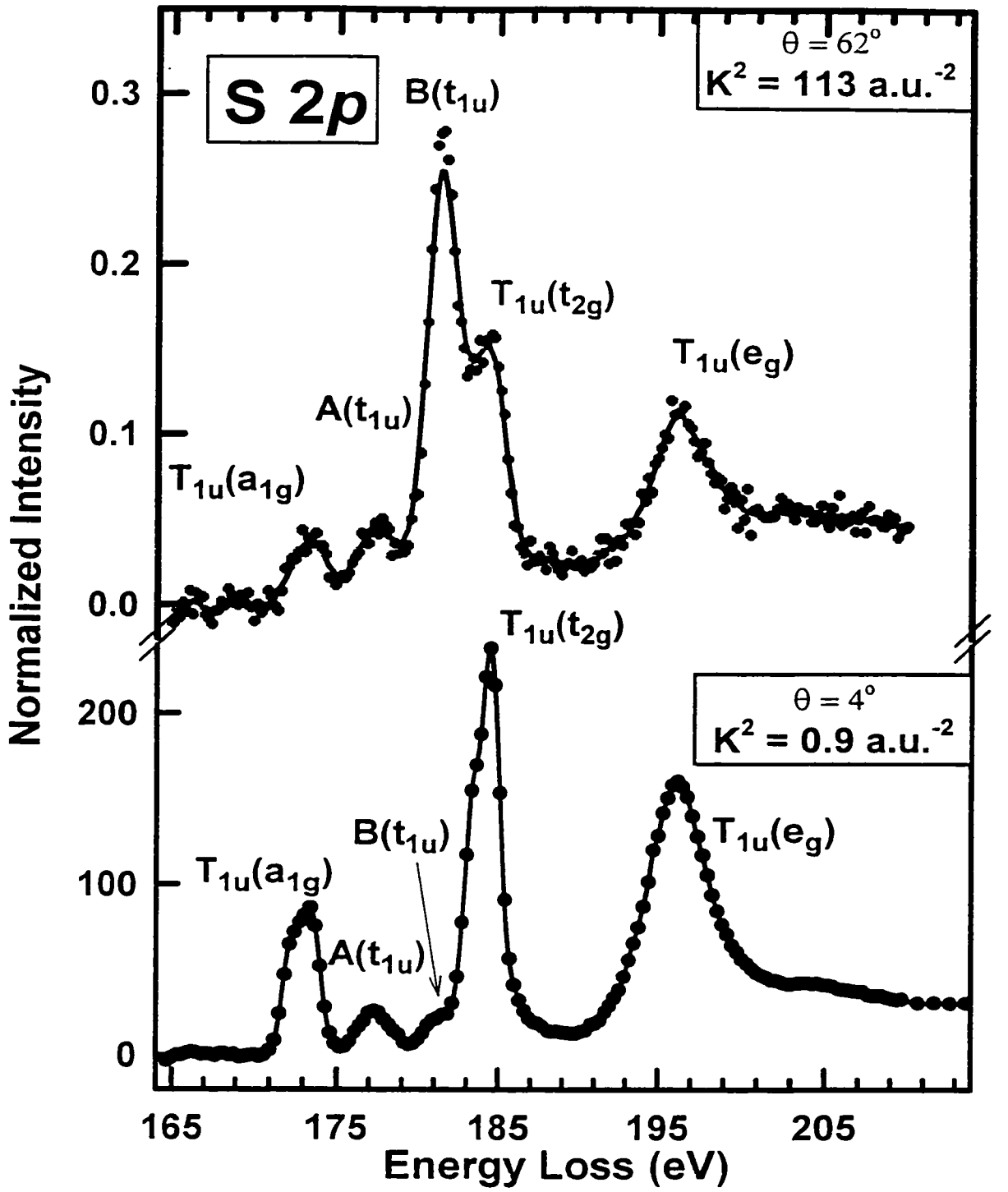

Fig. 5.1 Background subtracted electron energy-loss spectra in SF_6 in the S 2*p* region recorded at 1300 eV final electron energy and scattering angles of 4° (bottom) and 62° (top). The original data is the dots while the full line is a smoothed version to guide the eye.

Table 5.1 : Energies, widths, line shapes and optical oscillator strengths derived from a constrained multiple file curve-fit analysis of the S 2*p* spectra of SF_6.

State	E(eV)[a]	Line Type*	Width(eV)[a]	OOS ($x10^{-2}$)[b] (this work)	(literature) [TFT&95]	[D72]	[HSD&93]
$T_{1u}(a_{1g})$-3/2	172.5	G	1.41	7.0	7.9	9.6	8.7
$T_{1u}(a_{1g})$-1/2	173.6	G	1.14				
$A(t_{1u})$	177.5	G	2.86	3.5	0.9		
continuum 1[c]	180.4	E	1.50				
IP (3/2)[d]	180.4						
IP (1/2)[d]	181.6						
$B(t_{1u})$	181.2	G	2.06	0.06	0.06		
$T_{1u}(t_{2g})$-3/2	183.4	G	1.10	21	23	23	18
$T_{1u}(t_{2g})$-1/2	184.5	G	1.06				
continuum 2[c]	192.8	E	2.50				
$T_{1u}(e_g)$	195.9	G	2.73	19	20	34	24
$T_{1u}(e_g)$	197.4	G	3.36				

*G = Gaussian profile, E = error function shape

[a]The energy and width of each feature is fixed to these values during the fit. Only the intensities were varied in fitting the spectrum at each angle.

[b]The GOS scales were set by normalizing the extrapolated OOS for the a_{1g} to 0.096 and that of the t_{2g} to 0.23. In the fitting the 3/2 and 1/2 components were fit separately.

[c]The spectra are fit to two separate continua to take into account inner-well and outer-well regions of the potential barrier. The details are discussed in [TFT&95].

[d]Ionization potential from XPS measurements [JBE84, SCT73].

The most striking observation is that at 62°, K^2 = 113 a.u.$^{-2}$ the (S $2p(t_{1u})^{-1}$, $6t_{1u}$) "**B state**" (181 eV) is almost twice as intense as the next highest intensity S $2p$ spectral feature. Indeed the peak intensity of the "**B state**" first exceeds that of the (S $2p$ $(t_{1u})^{-1}$, t_{2g}) T_{1u} state (184.5 eV) at a momentum transfer of 47 a.u.$^{-2}$ or at scattering angles above 39° for a final electron energy of 1300 eV. According to the spectral assignments [TFT&95], the "**A state**" (177 eV) is associated with the same (S $2p$ $(t_{1u})^{-1}$, $6t_{1u}$) configuration as the "**B state**". Its relative intensity changes with K in a very different manner than that for the "**B state**". The shape of the signal between 175 - 180 eV is quite different between K^2 = 0.9 and 113 a.u.$^{-2}$.

Harrison [H86] first observed the "**B state**" signal in an EELS study at high scattering angle (90°) and very low final electron energies of 74 eV (K^2 ~ 25 a.u.$^{-2}$) and 150 eV (K^2 ~ 35 a.u.$^{-2}$). **Fig. 5.2** compares his results to ours for very similar K^2 (~ 25 a.u.$^{-2}$). Surprisingly, while the "**B state**" signal is still visible in the Harrison spectrum, it is much less prominent than in our work, which uses much higher impact energy. The "**A state**" (177 eV) is also much more intense with near threshold impact [H86] relative to our spectrum recorded at the same K^2 but with 1600 eV final electron energy. These observations suggest that inelastic scattering at lower impact energies cannot be described within a first Born approximation, since the Bethe-Born treatment [I71] requires that the spectral shape be determined by the value of K^2 and not the specific combination of impact energy and scattering angle used to achieve that momentum transfer.

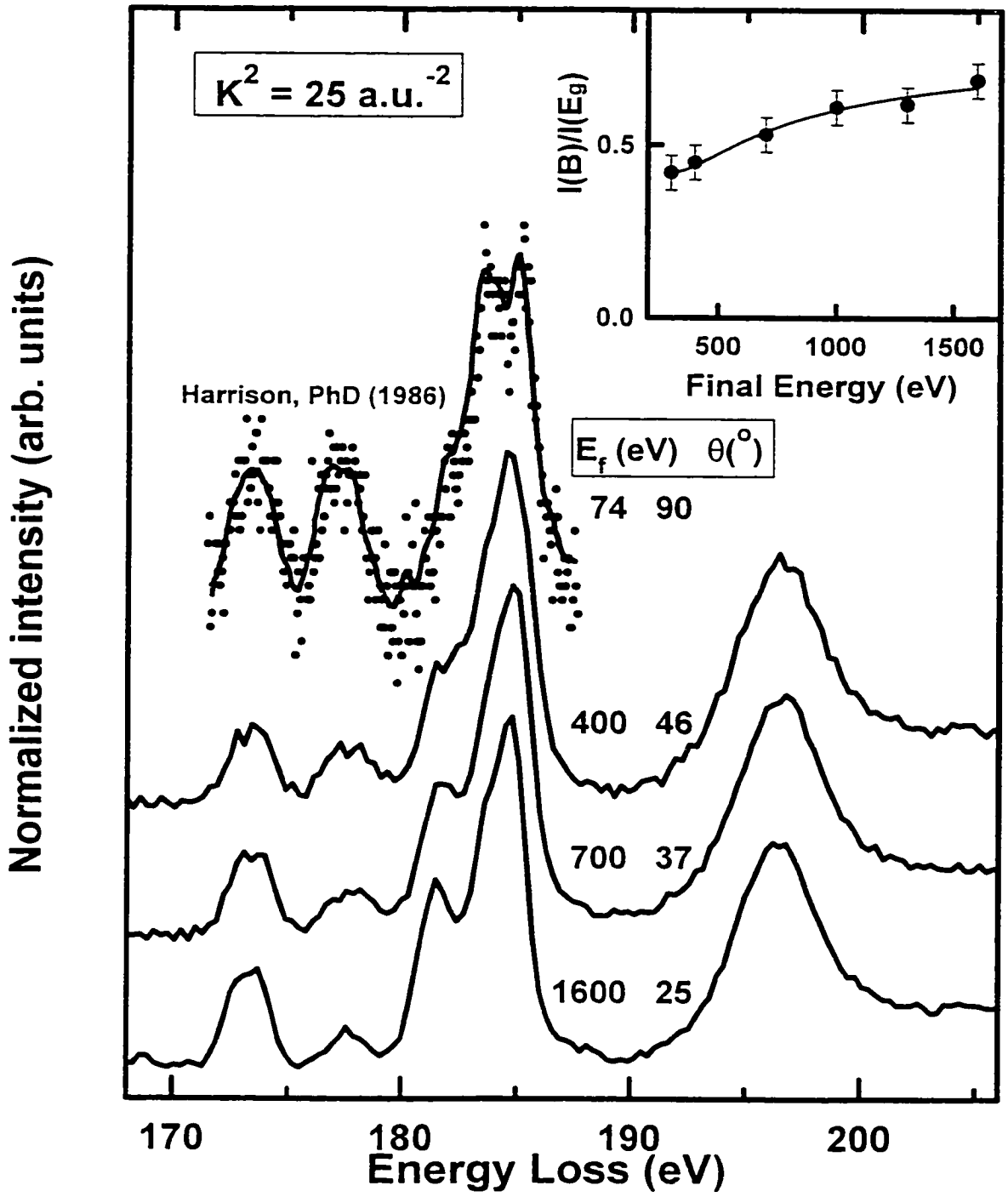

Fig. 5.2 Comparison of S 2*p* energy loss spectra of SF_6 recorded at a fixed K^2~25 a.u.$^{-2}$ but using variable final energies and scattering angles E_f=1600eV, θ = 25°; E_f=700eV, θ = 37°; E_f=400eV, θ = 46° (this work); E_f=74eV, θ=90° ([H86]). The insert plots the ratio of the intensity (peak area) of the B-state to that of the $T_{1u}(e_g)$ state (195eV).

In order to confirm the breakdown of the first Born approximation for lower impact energies, we systematically measured the S $2p$ spectrum at a range of impact energies while simultaneously changing the scattering angle to keep the momentum transfer constant at a relatively high value (~ 25 a.u.$^{-2}$). As the impact energy drops, the "B state" diminishes while the "A state" increases. The insert plots the ratio of the intensity of the "B state" to that of the (S $2p$ $(t_{1u})^{-1}$, e_g) T_{1u} state (195 eV). There is a clear change in slope around 700 eV final electron energy. This suggests that the first Born approximation is likely valid for the "**B state**" at higher impact energies but that it becomes increasing inappropriate at lower energies.

5.2.2. S $2s$ spectrum

Fig. 5.3 displays the background subtracted S $2s$ spectra recorded at small momentum transfer (4°, K^2 = 1.3 a.u.$^{-2}$), with that recorded at much higher momentum transfer (35°, K^2 = 40 a.u.$^{-2}$). **Table 5.2** lists the peak energies used in the data analysis, along with their spectral interpretation [FTT&95, BGH62]. It was not possible to achieve as large a scattering angle for S $2s$ studies because the S $2s$ is a weak signal on the strong S $2p$ background. Even so, these results are a significant extension in momentum transfer to those reported earlier [TFT&95, FTT&95].

Because the S $2s$ core level has opposite parity to the S $2p$ level, the dipole/non-dipole character of transitions to the same upper level is reversed.

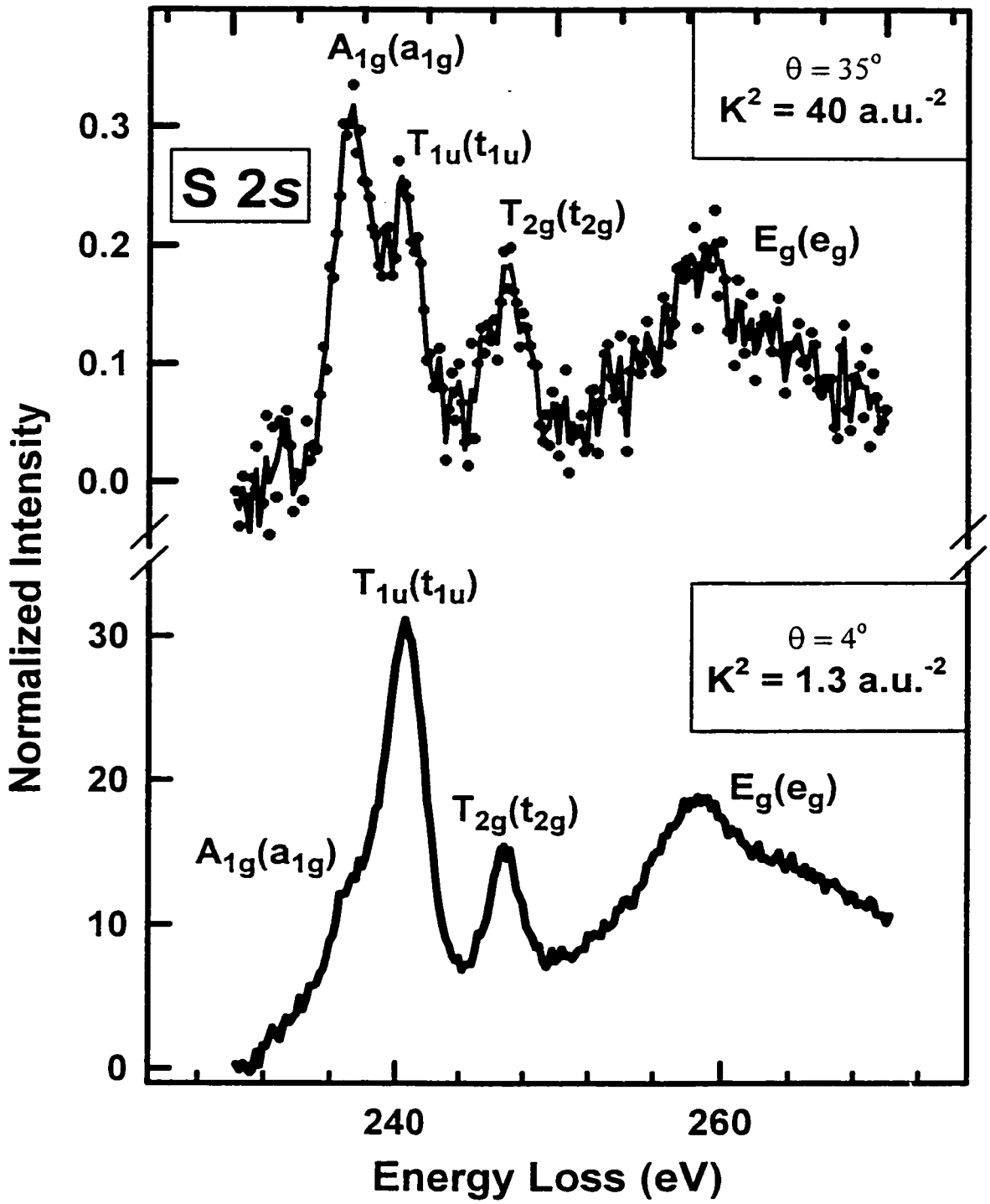

Fig. 5.3 Background subtracted electron energy-loss spectra of SF_6 in the S 2*s* region recorded at 1300 eV final energy and scattering angles of 4° (bottom) and 35° (top). The original data is the dots while the full line is a smoothed version to guide the eye.

Table 5.2 : Energies, widths, line shapes and optical oscillator strengths derived from a constrained multiple file curve-fit analysis of the S 2*s* spectra of SF_6.

State	E(eV) [a]	Line type	Width (eV)[a]	OOS ($x10^{-2}$)[b]
$A_{1g}(a_{1g})$	237.4	Gaussian	2.83	1.5
$T_{1u}(t_{1u})$	240.4	Gaussian	2.83	3.6
continuum	244.7	arctangent	1.25	
IP[c]	244.7			
$T_{2g}(t_{2g})$	246.8	Gaussian	2.14	0.7
$E_g(e_g)$	258.5	Gaussian	5.10	1.3
$E_g(e_g)$	262.8	Gaussian	7.97	

[a]The energy and width of each feature is fixed to these values during the fit. Only the intensities were varied in fitting the spectrum at each angle.
[b]GOS scale set by correlating S 2*s* and S 2*p* scales in a simultaneous measurement of both edges under near-dipole conditions.
[c]Ionization potential from XPS [SCT73].

In addition, since the S 2*s* level is non-degenerate, the orbital and state picture of the S 2*s* spectroscopy are interchangeable, which is not the case for the S 2*p* or F 1*s* excitation, where a full state picture is essential [FTT&95]. Thus, there is only one dipole-allowed S 2*s* excitation and three dipole-forbidden, quadrupole-allowed S 2*s* transitions. There is a very marked re-arrangement of spectral intensities with increasing momentum transfer.

The only electric-dipole-allowed S 2*s* inner-well core → valence transition is that to the (S $2s^{-1}$, t_{1u}) T_{1u} state at 240.5 eV. The features observed at 237.3 eV (A_{1g}), 246.9 eV (T_{2g}) and 258.9 eV (E_g) all correspond to electric dipole forbidden, quadrupole allowed transitions. These are quite prominent even at relatively low momentum transfer. This indicates that, at least in the moderate momentum transfer region, excitations from 2*s* core levels have more intense non-dipole transitions than excitations from S 2*p* levels. At high momentum transfer all three non-dipole transitions become relatively much more intense, and that for the (S $2s^{-1}$, a_{1g}) A_{1g} at 237.3 eV becomes the strongest spectral feature. Thus, as for the S 2*p* "**B state**", we find that optically forbidden, electric quadrupole transitions dominate the S 2*s* core excitation spectrum of SF_6 at sufficiently high momentum transfer.

5.2.3. F 1*s* spectrum

Fig. 5.4 compares energy loss spectra of SF_6 at the F 1*s* edge, recorded under dipole-dominated and extreme non-dipole conditions. **Table 5.3** lists the peak energies used in the data analysis, along with their spectral interpretation [FTT&95, BGH62].

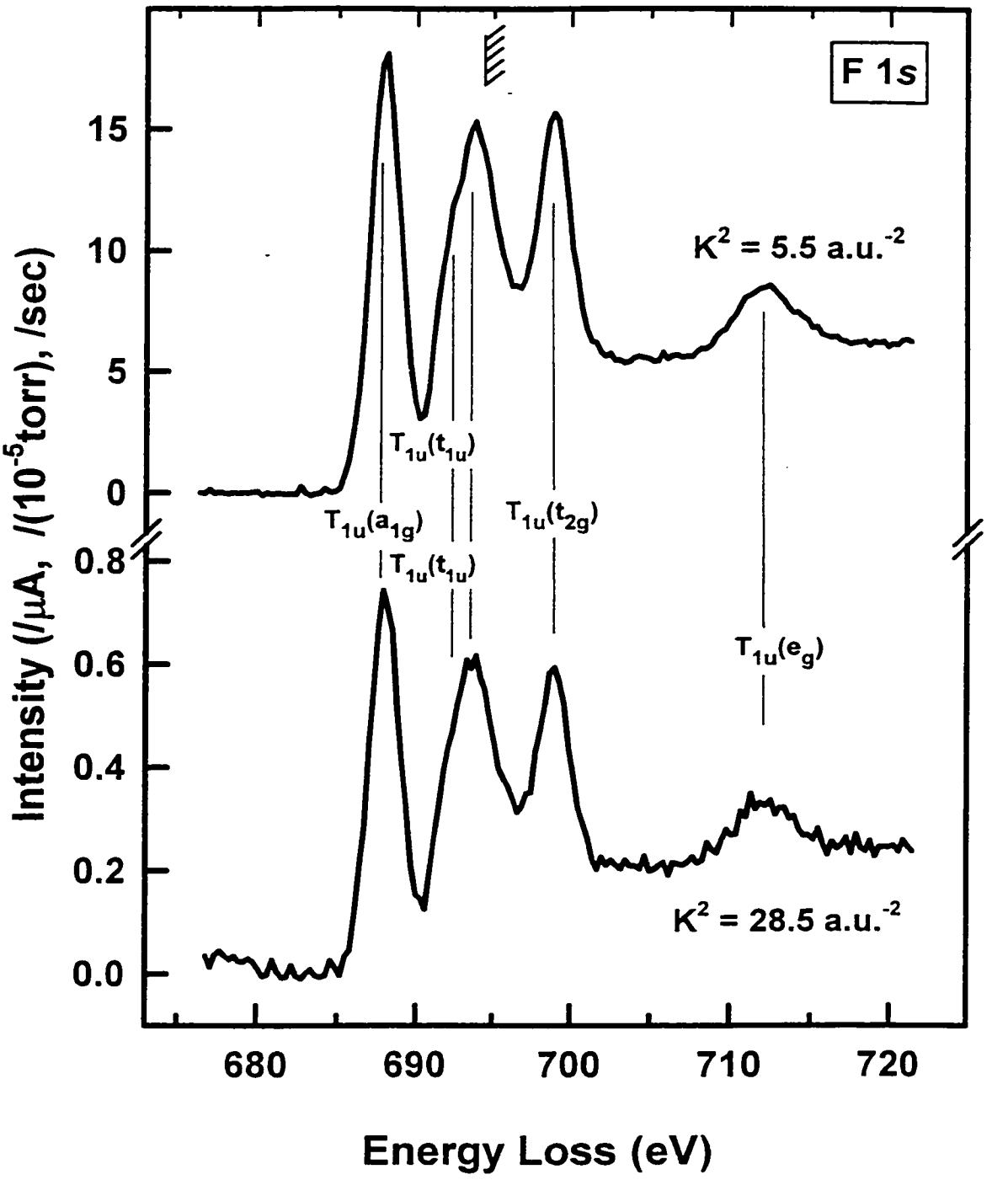

Fig. 5.4 Background subtracted electron energy loss spectra of SF_6 recorded with 1400eV final electron energy in the F 1*s* region in both near-dipole (4°) and non-dipole conditions (F 1*s* - 24°). The hatched lines indicate the ionization potential.

Table 5.3 : Energies, widths, line shapes and optical oscillator strengths derived from a constrained multiple file curve-fit analysis of the F 1*s* spectra of SF_6.

State	E(eV)[a]	Line type	Width (eV) [a]	OOS ($x10^{-2}$)[b]
$T_{1u}(a_{1g})$	687.9	Gaussian	2.36	10.7
$T_{1u}(t_{1u})$	691.4 (sh)	Gaussian	1.66	2.1
$T_{1u}(t_{1u})$	693.5	Gaussian	3.25	17.6
continuum	694.6	error function	1.3	
IP[c]	694.6			
$T_{1u}(t_{2g})$	698.8	Gaussian	2.60	9.9
$T_{1u}(e_g)$	712.1	Gaussian	4.41	4.7

[a]The energy and width of each feature is fixed to these values during the fit. Only the intensities were varied in fitting the spectrum at each angle.
[b]GOS scale was set by matching the relative data to the absolute GOS value at $K^2 = 2.9$ a.u.$^{-2}$ [HB78].
[c]Ionization potential from XPS [SCT73].

A correct symmetry analysis of F 1*s* excitation of SF_6 [FTT&95] shows there are five excited states that are dipole coupled to the ground state. A superficial examination of the F 1*s* spectrum suggests that there are four resonances corresponding to F 1*s* excitations, which previously had been assigned to the four virtual valence orbitals [HSD&93]. A closer examination reveals a distinct shoulder on the second peak, with an energy of 692.4 eV, 1.6 eV below the peak maximum at 694.0 eV. The F 1*s* spectral shape changes negligibly with increasing momentum transfer, suggesting that, either the dipole states dominate at all scattering conditions, or that any additional quadrupole states are not energy resolved and have similar GOS profiles such that their contributions are merged with the apparent dipole contributions. Interestingly, a recent combined experimental – computational study of the GOS for O 1*s* excitation of CO_2 [ETH&99] strongly suggests that in cases of core excitation from chemically equivalent sites, the non-dipole excitation channel can be as strong as the dipole channel at finite momentum transfer.

5.3. Generalized Oscillator Strengths for Inner Shell Excitation of SF_6

The next section illustrates the detailed GOS results for the S 2*p*, S 2*s* and F 1*s* GOS profiles of SF_6.

5.3.1. S 2*p*

Generalized oscillator strength profiles are shown for three dipole allowed S 2*p* transitions and for the S 2*p* continuum in **fig. 5.5**, and for the two dipole-forbidden S 2*p*

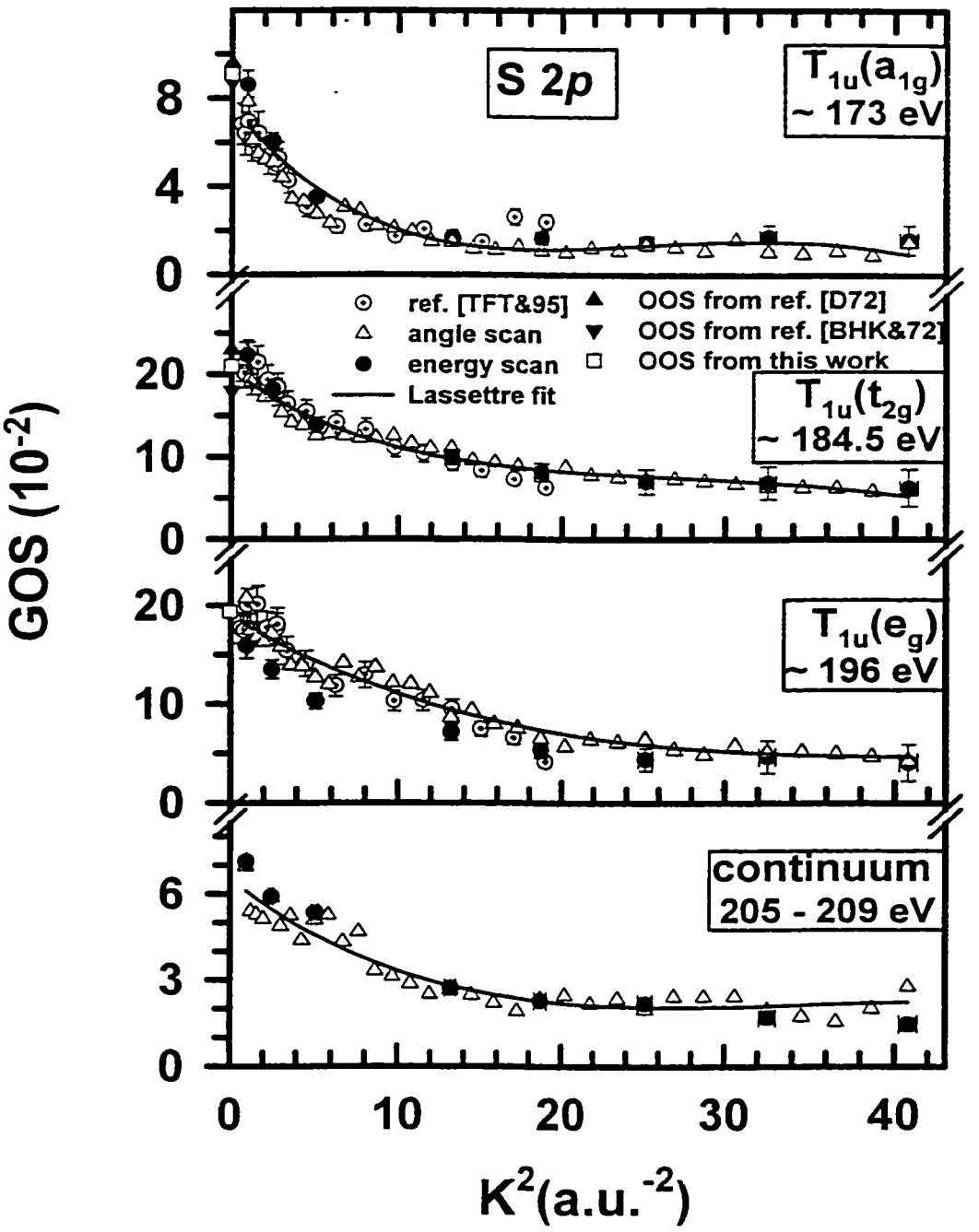

Fig. 5.5 GOS profiles for the $T_{1u}(a_{1g})$,$T_{1u}(t_{2g})$ and $T_{1u}(e_g)$ dipole-coupled S 2*p* excited states and continuum, derived from the experimental data. The GOS absolute scales were set to the OOS values for a_{1g} and t_{2g} transitions. The solid lines are the result of fits of the data to the Lassettre series.

transitions in **fig. 5.6**. The absolute GOS scale for the S 2*p* region was set by matching the graphical extrapolation to $K^2 = 0$ of the relative GOS profile for the $T_{1u}(a_{1g})$ and $T_{1u}(t_{2g})$ states to the average of the values reported by Dehmer [D72] (0.096 for a_{1g} and 0.23 for t_{2g}) and by Bleschmidt et al. [BHK&72] (0.087 for a_{1g} and 0.18 for t_{2g}). Since there is significant disagreement, especially for the t_{2g} OOS, using the mean literature OOS implies ~ 15% uncertainty in the absolute GOS values. The results derived from the 'energy-scan' and 'angle-scan' modes are plotted separately. In almost all cases there is good agreement between these two sets of results. Fits of the GOS profiles to a 3-term, modified Lassettre series are also plotted in Figs 5.5, 5.6 (and the other figures reporting GOS). The coefficients from the Lassettre fits are summarized in **table 5.4.**

The GOS for all three dipole-allowed transitions decay relatively smoothly to higher K^2 from a maximum at $K^2 = 0$. The shape and absolute values determined in this work are in good agreement with the previous results [TFT&95]. Since the spectrometer and procedures used in this work differ substantially from the earlier study (in particular, a different gas sample arrangement and thus a different geometric correction factor) this agreement provides strong and independent support that the derivation of GOS from peak areas with geometry correction is the correct approach, rather than determination from peak intensities without geometry correction, as reported by Ying et al [YML94].

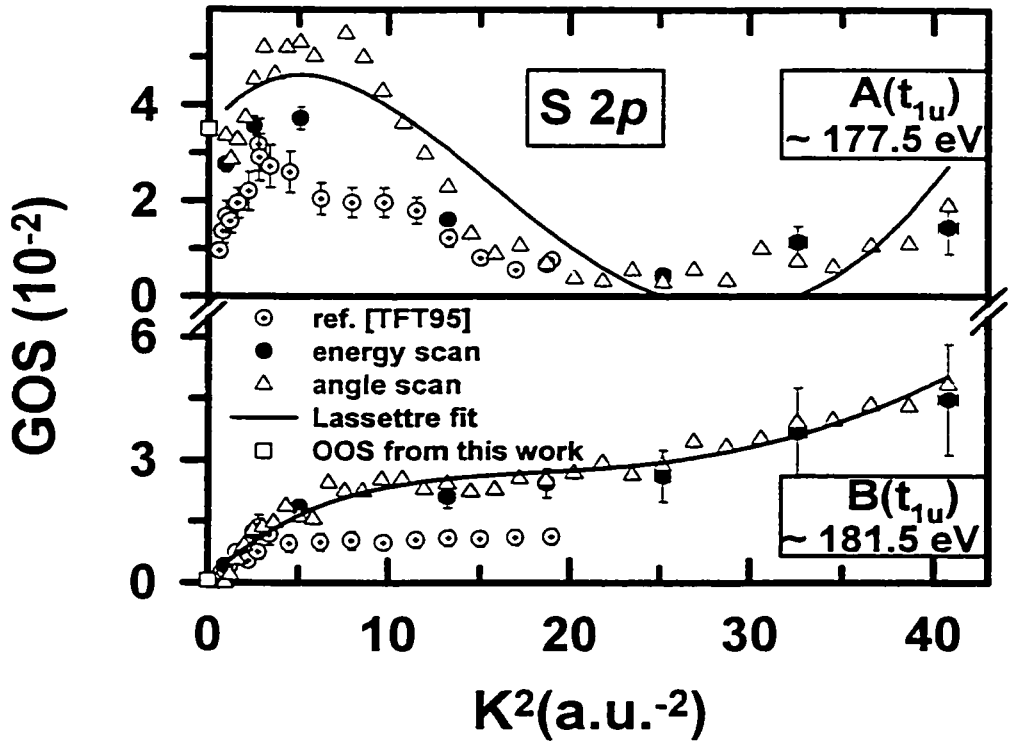

Fig. 5.6 GOS profiles for the $A(t_{1u})$ and $B(t_{1u})$ quadrupole-coupled S 2*p* excited states derived from the experimental data. The GOS absolute scales were set to the OOS values for a_{1g} and t_{2g} transitions. The solid lines are the result of fits of the data to the Lassettre series (chapter 2, equation 2.39).

Table 5.4 : Values of the Lassettre Coefficients derived from fits to the GOS profiles.

	f_0 x10^{-2}	f_1	f_2 x10^{2}	f_3 x10^{2}	f_1/f_0	f_2/f_0 x10^{3}	f_3/f_0 x10^{4}
S 2*p* - $T_{1u}(a_{1g})$	7.0	-4.9	1.2	-9.1	-64	1.6	-1.2
$A(t_{1u})$	3.5	2.5	-1.2	11	71	-3.3	3.1
$B(t_{1u})$	0.06	1.8	-0.3	2.8	2900	-57	46
$T_{1u}(t_{2g})$	21	-5.5	1.0	-6.3	-27	0.5	-0.3
$T_{1u}(e_g)$	19	-5.3	0.7	-2.8	-28	0.4	-0.2
S 2*s* - $A_{1g}(a_{1g})$	1.5	-0.2	0.1	-0.7	-16	0.6	-0.5
$T_{1u}(t_{1u})$	3.6	-1.8	0.5	-3.3	-51	1.2	-0.9
$T_{2g}(t_{2g})$	0.7	0.6	-0.3	2.8	82	-3.8	3.8
$E_g(e_g)$	1.3	1.2	-0.7	7.9	88	-5.0	5.9
F 1*s* - $T_{1u}(a_{1g})$	10.9	-10.1	4.1	-51	-92	3.7	-4.7
$T_{1u}(t_{1u})^1$	1.5	-1.5	0.6	-1.4	-98	3.5	-0.9
$T_{1u}(t_{1u})^2$	12.8	-11.3	4.3	-51	-89	3.9	-4.0
$T_{1u}(t_{2g})$	7.2	-7.7	3.6	-54	-108	5.0	-7.5
$T_{1u}(e_g)$	3.4	-3.7	1.9	-37	-110	5.6	-11

[1] $(2a_{1g}, 6t_{1u})T_{1u}$

[2] $(1e_g, 6t_{1u})T_{1u}$

The GOS for all three dipole-allowed transitions decay relatively smoothly to higher K^2 from a maximum at $K^2 = 0$. The shape and absolute values determined in this work are in good agreement with the previous results [TFT&95]. Since the spectrometer and procedures used in this work differ substantially from the earlier study (in particular, a different gas sample arrangement and thus a different geometric correction factor) this agreement provides strong and independent support that the derivation of GOS from peak areas with geometry correction is the correct approach, rather than determination from peak intensities without geometry correction, as reported by Ying et al [YML94].

The GOS profile for the dipole forbidden "**A state**" signal shows a maximum at $K^2 \sim 4$-6 a.u.$^{-2}$, and is in good agreement with the earlier results [TFT&95]. The intensity of the "**A state**" is non-zero in the optical limit [HSD&93]. These observations suggest there are two excitation mechanisms for this state: a vibronically allowed one, which gives rise to the weak component observed optically [L77, SS88] and a dipole-forbidden mechanism [FTT&95, HSD&93].

In the case of the B(t_{1u}) transition there is good agreement between values obtained from 'energy-scan' and 'angle-scan' modes and the agreement with the earlier values [TFT&95] is reasonable, at least in the region of small K^2 values. Note that the data reported in [TFT&95] was recorded using ~0.3 eV resolution rather than the ~0.7 eV resolution of the present work. It is interesting to note that even though the two states are associated with the same electron configuration, the excitations to the **A** and **B** signals have quite different GOS profiles. The OOS for the **B**-state is zero and the **B**-state GOS profile contains much more signal above 10 a.u.$^{-2}$, continuing to increase right to the

maximum K^2 sampled. Indeed the **B**-state GOS is still rising at $K^2 = 113$ a.u.$^{-2}$ (62°, $E_0 =$ 1300 eV) [ETH99]. This suggests there are at least two different states contributing to the "**B state**" signal, consistent with the lineshape analysis of the high resolution spectrum reported in [FTT&95].

The f_n values derived from the fit to the modified Lassettre equation (chapter 2, equation 2.39) exhibit sign alternation. This was also observed by both Ying [YML93] and Turci [TFT&95]. The f_n/f_0 ratios for the dipole allowed transitions in S 2*p* are found to be similar in magnitude to the ones from ref. [YML93] and [TFT&95]. The f_n/f_0 ratios determined for the **A**, **B** dipole-forbidden S 2*p* transitions are smaller than in the previous study [TFT&95], consistent with the observed difference in the GOS shape as well as the presence of a second maximum in both profiles, which is only seen in the present work due to the much larger K^2 range investigated.

5.3.2. S 2*s*

Fig. 5.7 reports the GOS profiles for the four S 2*s* transitions and for the S 2*s* continuum. The relative S 2*s* GOS were converted to an absolute scale by simultaneously measuring the S2*p*→t_{2g} and S2*s*→ t_{1u} intensities under near-dipole conditions ($K^2 = 0.5$ a.u.$^{-2}$). The ratio of peak areas (0.205) was combined with the S 2*p* GOS scale factor to generate the scale factor for the S 2*s* GOS. Although some early results were presented elsewhere [HEF&98], the GOS for the S 2*s* states are mapped with high statistical accuracy for the first time and the K^2 range has been extended to approximately 40 a.u.$^{-2}$.

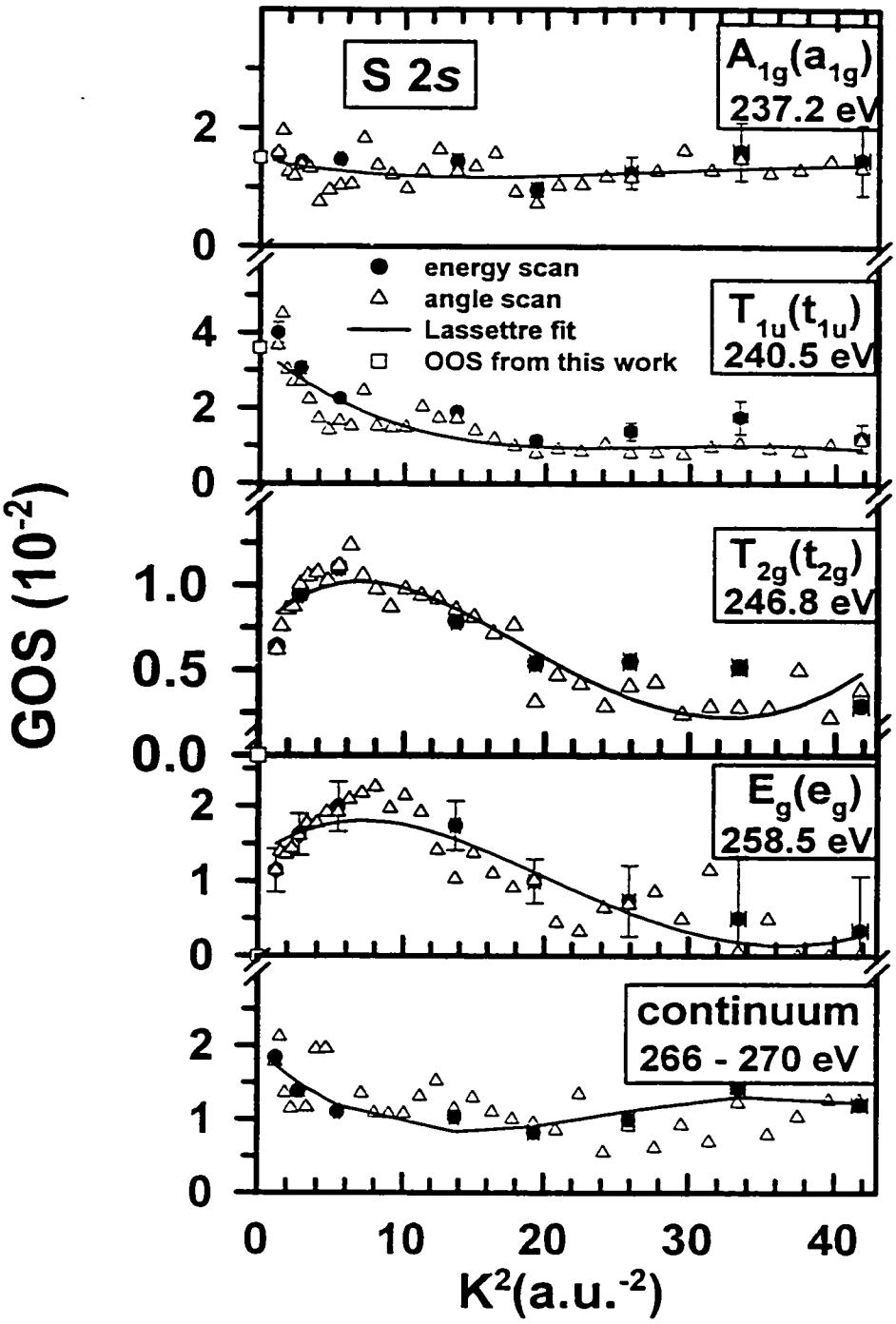

Fig. 5.7 GOS profiles for the $T_{1u}(t_{1u})$ dipole-coupled S 2*s* excited state and for the $A_{1u}(a_{1u})$, $T_{2g}(t_{2g})$ and $E_g(e_g)$ quadrupole-coupled S 2*s* excited states and continuum derived from the experimental data. The absolute GOS scale was set by correlating S 2*s* and S 2*p* scales in a simultaneous measurement of both edges under near-dipole conditions. The solid lines are the result of fits of the data to the Lassettre series.

The GOS profile for the dipole allowed S $2s$ (a_{1g}) $\rightarrow$ t_{1u} transition decays continuously from a maximum at $K^2 = 0$. The GOS profiles for the t_{2g} and e_g dipole forbidden transitions approach zero at $K^2 = 0$ then increase to a peak at $K^2 \sim 8$ - 10 a.u.$^{-2}$. Surprisingly, the $A_{1g}(a_{1g})$ state is almost independent of K^2 and the GOS profile clearly indicates a non-zero OOS. It is possible there is a vibronic mechanism active for S $2s \rightarrow$ a_{1g} excitation in the dipole limit. The peak for the dipole-allowed transition S $2s$ (a_{1g}) $\rightarrow$ t_{1u} transition in the optical (total ion yield) spectrum [FTT&95] has a shoulder on the low energy side, in the region of the a_{1g} state. In the S $2s$ edge there is a clear enhancement of transitions to dipole-forbidden states with increasing momentum transfer. Thus, at high momentum transfer (fig. 5.3) all three non-dipole transitions, observed at 237.3 eV (A_{1g}), 246.9 eV (T_{2g}) and 258.9 eV (E_g), become relatively more intense than the dipole-allowed transition at 240.5 eV (T_{1u}). In the strong non-dipole regime the A_{1g} transition dominates the spectrum (see fig. 5.3). Fig. 5.7 also plots fits of the GOS profiles to the modified Lassettre function. The general trend for alternating signs in the coefficients is consistent with the (non-controversial) spectral assignments [FTT&95].

5.3.3. F $1s$

Fig. 5.8 presents the GOS profiles for F $1s$ excitations of SF_6. This is the first report of GOS profiles for F $1s$ excited SF_6.

The relative GOS of the F $1s \rightarrow a_{1g}$ transition was extrapolated to $K^2 = 0$ and set to 0.018 per F atom for this transition, the OOS value for the a_{1g} transition derived by atomic continuum normalization [HM94]. The independence of the F $1s$ spectral shape

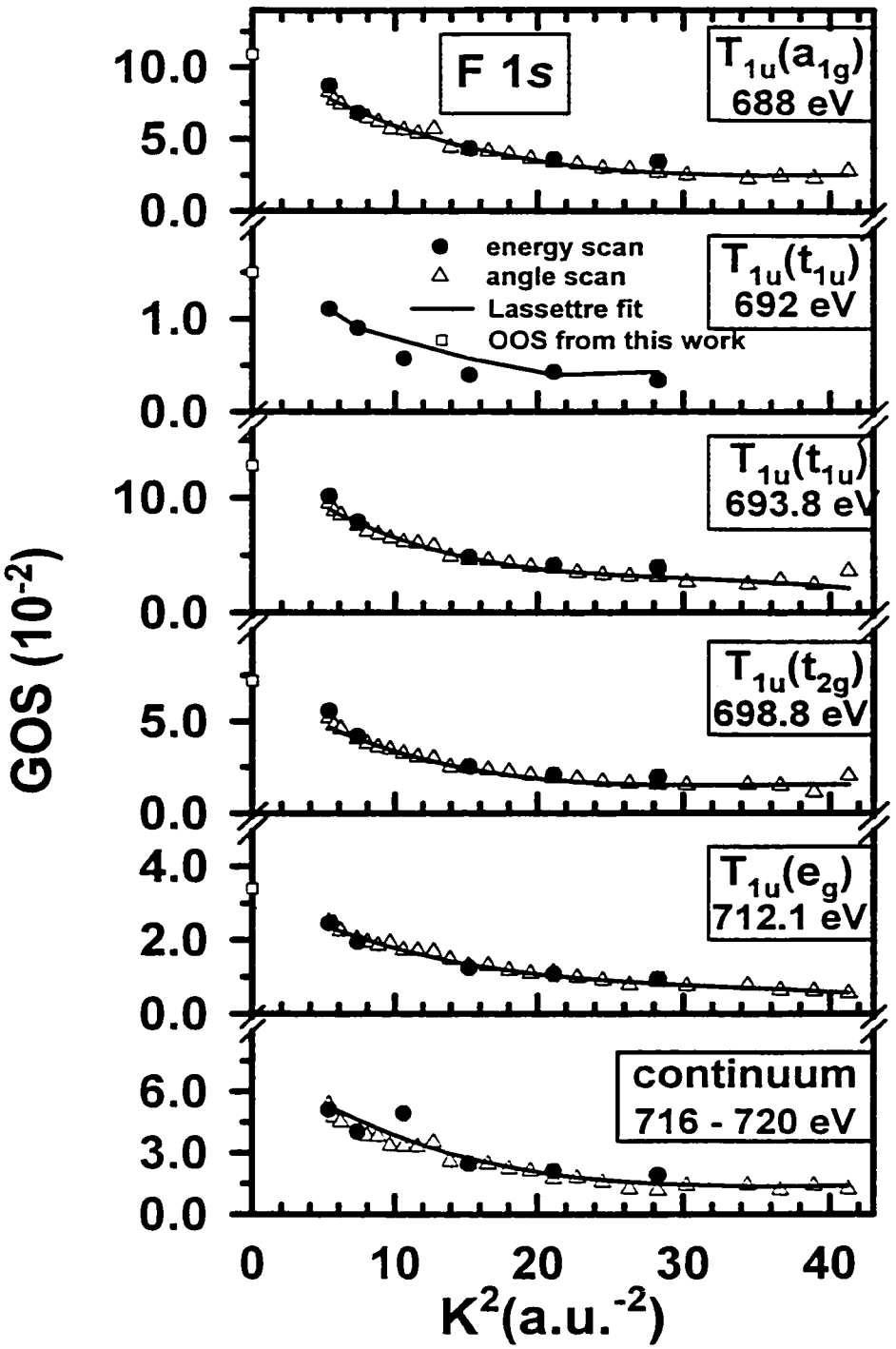

Fig. 5.8 GOS profiles for the $T_{1u}(a_{1g})$, $T_{1u}(t_{1u})$, $T_{1u}(t_{2g})$ and $T_{1u}(e_g)$ dipole-coupled F 1*s* excited states and continuum derived from the experimental data. The absolute GOS scale was set by atomic continuum normalization. The solid lines are the result of fits of the data to the Lassettre series (chapter 2, equation 2.39).

on K^2 means that atomic continuum normalization at finite K^2 is not a significant source of error.

Group theory analysis shows there are five dipole accessible F 1*s* excited states [FTT&95]. The GOS profiles for each of the five resolvable bands $(1t_{1u}, 6a_{1g})T_{1u}$, $(2a_{1g}, 6t_{1u})T_{1u}$, $(1e_g, 6t_{1u})T_{1u}$, $(1t_{1u}, 2t_{2g})T_{1u}$ and $(1t_{1u}, 4e_g)T_{1u}$ are consistent with a dipole allowed character of the transitions. Dipole transitions may dominate F 1*s* excitation because promotions to all five virtual valence orbitals can occur from either the gerade $(2a_{1g}, 1e_g)$ or the ungerade $(1t_{1u})$ F 1*s* molecular orbitals, as required to fulfill dipole selection rules. Fig. 5.8 also plots fits of the F 1*s* GOS profiles to the modified Lassettre function. The signs of the coefficients derived from fitting the modified Lassettre function to the measured F 1*s* GOS profiles alternate (see table 5.4). This suggests that dipole transitions dominate at all momentum transfer, in apparent contrast to the suggestion from a theoretical study of O 1*s* GOS profiles of CO_2 [ETH&99], that there might be large non-dipole contributions in cases of core excitation from symmetry equivalent sites like the F 1*s* levels of SF_6.

5.4. Dynamic effects of inner-shell shape resonances on GOS profiles

An important theme in inner-shell excitation of molecules like SF_6 with strong potential barrier phenomena, is the role that continuum shape resonances might play in photoionization dynamics. The shape resonance delays the escape of the ionized core electron, and thus the system takes on some of the characteristics of a quasi-bound excited state. Attempts have been made to see if these influences extend to the time scale

of bond breaking, by searching for changes in the photoionization mass spectrum. All evidence reported to date [HBV78] suggests that the ionic fragmentation at the t_{2g} and e_g S 2*p* continuum resonances of SF_6 is the same as that of the non-resonant continuum. Since the inelastic scattering interaction takes place on a K-dependent time scale, it was of interest to search for evidence of an impact of the continuum resonances on GOS profile – i.e., to answer the question, are the shapes of the GOS for the t_{2g} and e_g S 2*p* continuum resonances the same as, or different from that of the non-resonant continuum.

Fig. 5.9 shows the GOS profiles for the t_{2g} and e_g resonances from each spectral edge (S 2*p*, S 2*s*, F 1*s*), together with their ratio of the GOS profile of the corresponding continuum. The shapes of the ratios show no structure or trend at all, suggesting that the t_{2g} and e_g resonances have the same GOS profile shape at all edges.

5.5. Summary

Our results demonstrate that relatively unknown, non-dipole excitations can become the dominant spectral feature in inner shell EELS spectra recorded at large momentum transfer. From our variable impact energy study we conclude that a relatively complete exploration of the scattering surface may be required to be sure that all states are found. Studies using only threshold excitation or only high impact energy (first Born approximation) excitation may provide only a partial picture of intensity redistribution as a function of momentum transfer. A detailed study of the GOS for S 2*p*, S 2*s* and F 1*s* excitation of SF_6 over $0.8 < K^2 < 40$ a.u.$^{-2}$ was presented.

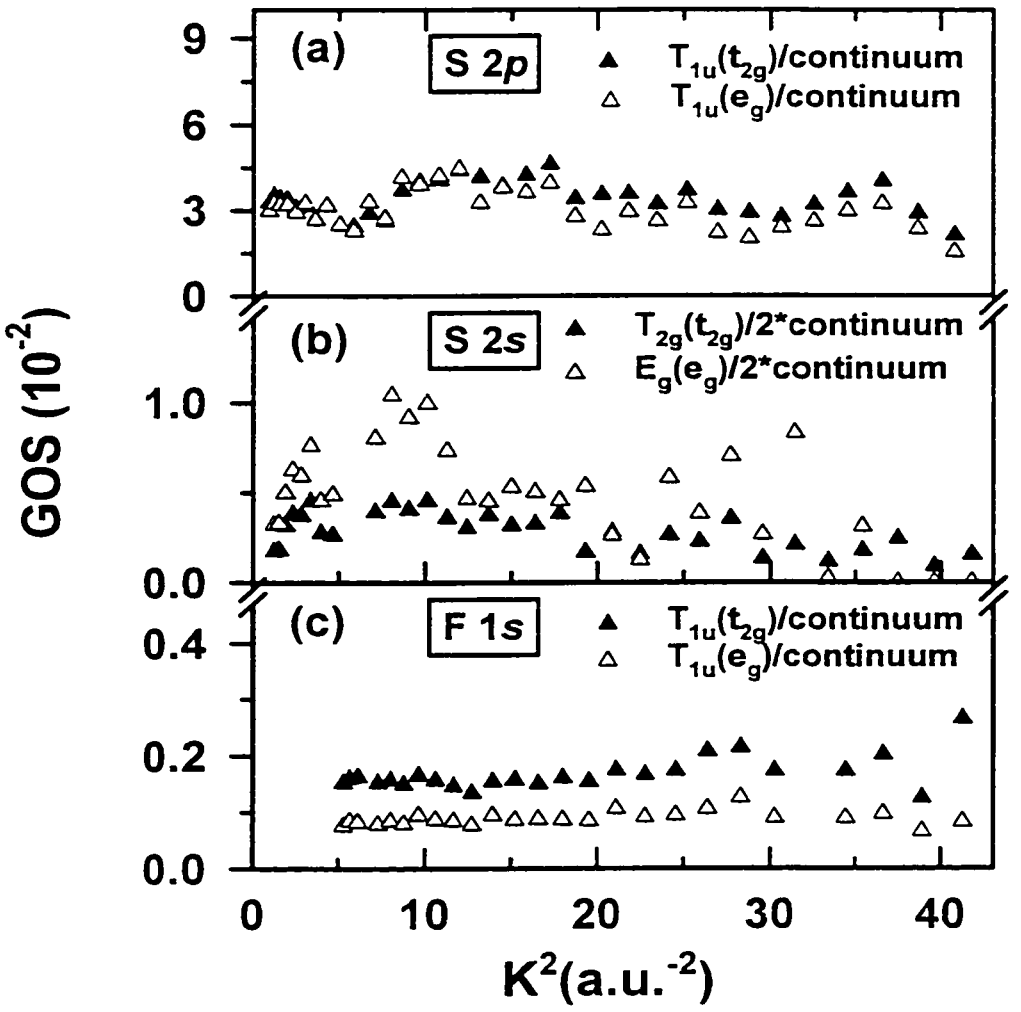

Fig. 5.9 Comparison of the GOS profiles for the t_{2g} and e_g continuum shape resonances and their ratios to the GOS profiles of the continuum for S 2*p*, S 2*s* and F 1*s* core excitation.

Chapter 6

EXPERIMENTAL AND THEORETICAL STUDY OF GENERALIZED OSCILLATOR STRENGTHS FOR C 1*s* AND O 1*s* EXCITATION IN CO_2

In this chapter the electron energy loss spectra of CO_2 in the region of C 1s and O 1s excitation recorded over a wide range of momentum transfer (K), (2 a.u.$^{-2}$ < K^2 < 70 a.u.$^{-2}$) is presented. Also, the dipole forbidden transition to the (C 1s σ_g^{-1}, σ_g) $^1\Sigma_g^+$ state in CO_2 ($D_{\infty h}$ symmetry) is detected for the first time.*

The data analysis, described in detail in chapter 4, has been used to convert the measured relative cross sections to absolute, momentum transfer dependent, generalized oscillator strength (GOS) profiles for all resolved C 1s and O 1s transitions of CO_2. Theoretical results for the GOS, computed within the first Born approximation (FBA) by Dr. C. E. Bielschowsky and A. B. Rocha from Universidade Federal do Rio de Janeiro (UFRJ), were obtained with ab-initio configuration interaction wave functions for the C 1s transitions and with ab-initio generalized multi-structural wave functions for the O 1s transitions. These wave functions include relaxation, correlation and hole localization effects. Theory predicts large quadrupole contributions to the GOS for O1s excitations. Overall there is good agreement between the experimental and theoretical results indicating that the FBA holds to a surprisingly large momentum transfer for the core excitations studied.

6.1. Generalities

The study of GOS up to such large K^2 values gives new insight into spectral assignments for CO_2 and the nature of GOS surfaces for core excitation.

An ongoing collaboration between the Hitchcock group at McMaster University and the Bielschowsky group at Universidade Federal do Rio de Janeiro (UFRJ) provided the theoretical work included in this chapter. Dr. Cassia Turci (UFRJ) also provided a great input in all aspects of experimental methodology and data treatment.

In order to take into account the strong relaxation that occurs when an inner-shell electron is promoted to a valence orbital, independent configuration interaction (CI) target electronic wave functions were calculated by Alexandre Rocha and Carlos Bielschowsky (UFRJ) for the ground and each of the excited states. The matrix elements between the non-orthogonal wave functions were determined within a bi-orthogonalization procedure [BNH92, MB93]. The conventional non-localized molecular orbital picture leads to theoretical results for O 1*s* excitation, which are in poor agreement with experiment. An improvement can be obtained by considering the excited electron in an electronic structure with a hole localized on one of the O atoms [RO85]. This approach leads to excitation energies and optical oscillator strengths (OOS) in better agreement with the experimental results but still with considerable error. It also has the additional disadvantage of breaking the molecular symmetry. In order to restore the molecular symmetry while still considering strong core hole localization, the generalized multistructural wave function (GMS) is used, where the excited state is built with different nonorthogonal structures [BNH92, MB93].

This work is part of a broader theoretical [SKR&82, BNH92, MB93, MBB&94] and experimental [TFT&95, FTT&95, ETH99, EFT&99] investigation of inner shell GOS surfaces.

The ground state of carbon dioxide is linear and can be described by the electron configuration:

$(1\sigma_g)^2\,(1\sigma_u)^2\,(2\sigma_g)^2\,(3\sigma_g)^2\,(2\sigma_u)^2\,(4\sigma_g)^2\,(3\sigma_u)^2\,(1\pi_u)^4\,(1\pi_g)^4\,(2\pi_u^*)^0\,(5\sigma_g^*)^0\,(4\sigma_u^*)^0\,,\ ^1\Sigma_g^+$

where $(2\pi_u^*)^0$, $(5\sigma_g^*)^0$ and $(4\sigma_u^*)^0$ are unoccupied orbitals of antibonding character. The $1\sigma_g$ and $1\sigma_u$ orbitals are linear combinations of oxygen 1*s* atomic orbitals, while the $2\sigma_g$ is the carbon 1*s* atomic orbital. Because the atomic orbitals of three atoms are involved, a larger number of MOs results, in particular, two empty antibonding MOs of σ symmetry, the $5\sigma_g^*$ and $4\sigma_u^*$ orbitals, and one empty π^*, the $2\pi_u^*$ orbital. Note that the 1*s* orbital of carbon is nondegenerate and *gerade* since the carbon atom is located in the inversion center of the molecule. This leads to different oxygen and carbon K-shell spectra. In CO_2 transitions from C 1*s* are allowed to the $4\sigma_u^*$ (node) but not to the $5\sigma_g^*$ (node less) MO, while both transitions are allowed for excitation of O 1*s*. The allowed transitions follow from a general rule, which forbids transitions between two states of the same *inversion* symmetry. Hence g → g and u → u transitions are forbidden. The reason is that the dipole operator is *ungerade* with respect to inversion and hence the direct product of initial and final states must be *ungerade* too. For O 1*s*, the initial state is a nearly degenerate $1\sigma_g$ and $1\sigma_u$ pair and the transitions $1\sigma_g \rightarrow 2\pi_u^*$, $1\sigma_u \rightarrow 5\sigma_g^*$ and $1\sigma_g \rightarrow 4\sigma_u^*$ are allowed. In contrast, for the C 1*s* excitation, the initial $2\sigma_g$ MO is of *gerade* symmetry only and therefore the $2\sigma_g \rightarrow 5\sigma_g^*$ transition is forbidden.

Within twenty eV above the core ionization threshold, shape resonances are characteristically found in the photoabsorption spectra of small molecules. This type of resonance can be thought of as a one-electron phenomenon and to be due to the temporary trapping of the outgoing photoelectron by a centrifugal potential barrier, or alternatively, due to a transition into an antibonding molecular orbital in the continuum [GGL72]. In this chapter, molecular orbital language is used to discuss these continuum features while recognizing that there is a strong dynamical aspect to these features. Many groups have noted that positions of continuum shape resonances in small molecules can be correlated in various ways with bond lengths [SSH84]. In this regard, the σ^* resonances of CO_2 have been a controversial subject. The positions of the features initially attributed to σ^*_{CO} resonances in CO_2 (312 eV in C 1*s*, 559 eV in O 1*s*) were anomalous with respect to an empirical correlation of bond length and resonance position [SSH84]. This was used as a central point in the critique of Piancastelli *et al.* [PLF&87] of the empirical correlation. Later [HS87] it was noted that in CO_2 and several other unsaturated linear triatomic molecules, the short bond length leads to strong interaction of σ^*_{CO}(L) and σ^*_{CO}(R) (the L and R refer to left and right localized σ^*_{CO} functions, which must be mixed to generate correctly symmetry adapted functions) such that there is a large energy separation between the two σ^*_{CO} resonances, roughly corresponding to that between the $5\sigma_g^*$ and $4\sigma_u^*$ molecular energy levels. The average position of core excitation to these two σ^* levels was postulated to be the appropriate parameter to use in the empirical bond length correlation [HS87]. Results from low energy electron scattering [TAP79] and valence photoemission [FLK84] indicate that the $5\sigma_g^*$ and $4\sigma_u^*$

levels are separated by ~ 16 eV in the ground state. Calculations [DDH82, LM82] suggested there should be a similar separation between the O 1*s* ($1\sigma_u \rightarrow 5\sigma_g^*$) and O 1*s* ($1\sigma_g \rightarrow 4\sigma_u^*$) core excited states. Re-examination of the O 1*s* spectrum showed that there are features attributable to O 1*s* excitation to both σ^* levels [HS87]. The location of the weak feature at 542 eV attributed to O 1*s* ($1\sigma_u \rightarrow 5\sigma_g^*$) transitions is consistent with the calculation [DDH82, LM82]. However, for symmetry reasons, only the C 1*s* ($2\sigma_g \rightarrow 4\sigma_u^*$) transition can be observed in photoabsorption or dipole-regime ISEELS. In order to have a more complete understanding of how positions of continuum resonances relate to molecular structure [SSH84, HS87] and also to have a better understanding of the core level spectroscopy of CO_2, extensive non-dipole ISEELS measurements have been carried out, with the goal of identifying the location of the electric dipole forbidden C 1*s* ($2\sigma_g \rightarrow 5\sigma_g^*$) transition.

6.2 Results and discussion

6.2.A Spectroscopy

6.2.A.1. C 1*s* Excitation

The pass energy used for the analyzer was 50 eV and the final electron energy was 1300 eV. The energy scales of all spectra were calibrated internally, using the well known values of the π^* transitions of CO_2 [SB84].

Figure 6.1 presents experimental C 1*s* spectra recorded under small ($\theta = 4°$, $K^2 = 1.6$ a.u.$^{-2}$) and large ($\theta = 32°$, $K^2 = 34.2$ a.u.$^{-2}$) momentum transfer conditions. The spectra

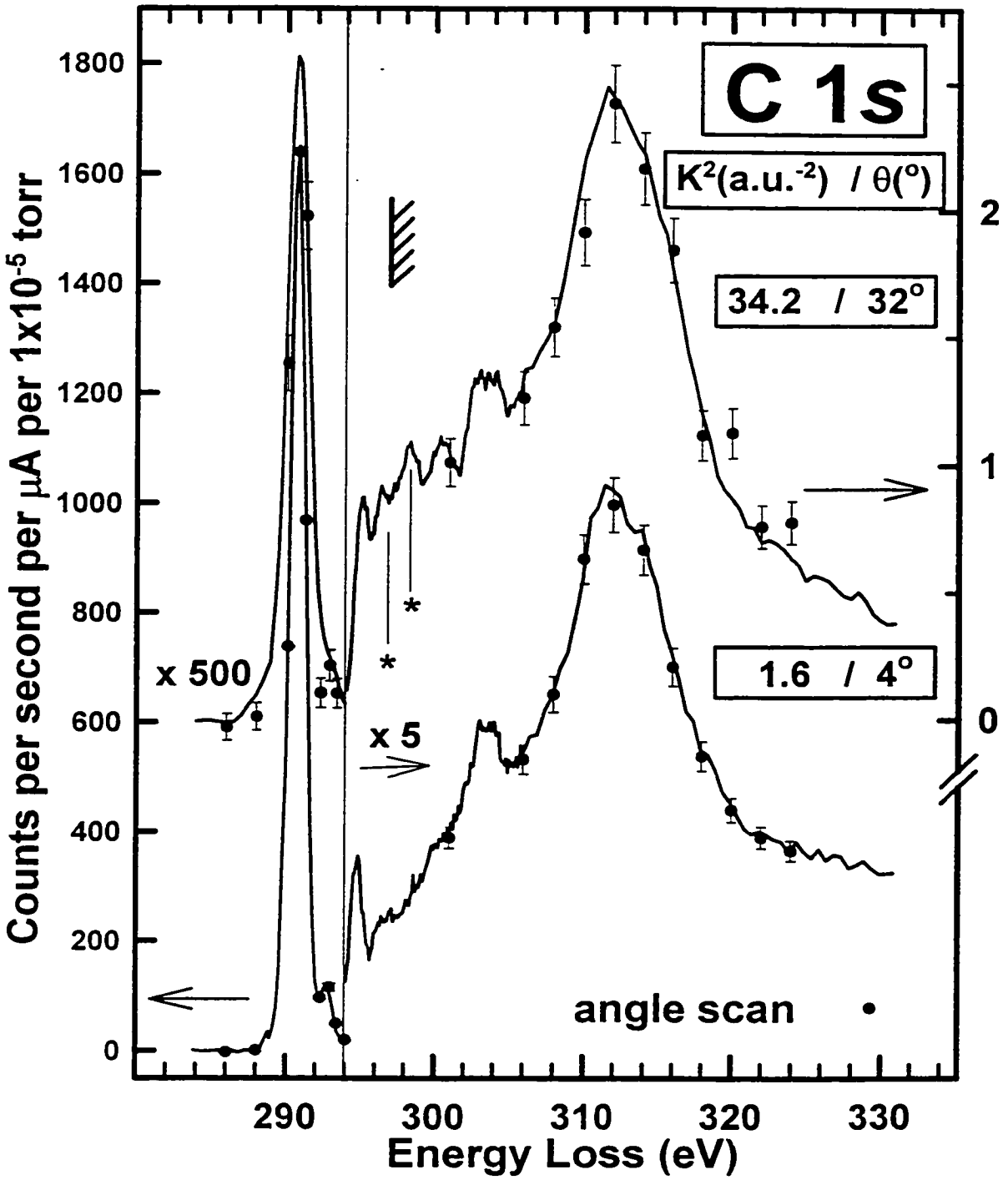

Fig. 6.1 Comparison of C 1*s* energy loss spectra of CO_2 recorded at 4° and 32°. Note the x5 vertical expansion at 294 eV and 500-fold scale factor between the 4° and 32° data. The hatched line indicates the C 1*s* IP as determined by X-ray photoelectron spectroscopy [JBE84].

plotted have been normalized to the beam current and gas pressure, are background subtracted, but they have not been subjected to the geometric or kinematic corrections.

Table 6.1 summarizes the experimental and theoretical energies and assignments of the C 1*s* spectral features. The theoretical and experimental excitation energies agree within 1 eV and there is an excellent match for the C 1*s* ($2\sigma_g^{-1}$, $2\pi_u^*$) transition. The calculated value for the C 1*s* $\rightarrow$ 3*p*σ_u excitation energy is probably too large because this state is the second root of this symmetry in the CI calculations.

The intense peak at 290.74 eV is the $X^1\Sigma_g^+ \rightarrow {}^1\Pi_u$ (C 1*s* $2\sigma_g^{-1}$, $2\pi_u^*$) transition. The other discrete peaks in the C 1*s* spectrum [WB74] are associated with the 3*s* and 3*p* Rydberg states which converge to the carbon 1*s* ionization limit (IP = 297.5 eV [JBE84]). They are much weaker features since the π^* state involves C 1*s* excitation to a valence molecular orbital (principal quantum number, n = 2), while the higher energy Rydberg states are associated with excitation to more diffuse Rydberg orbitals (n = 3, 4).

Surprisingly, the dipole forbidden C 1*s*$\sigma_g \rightarrow$ 3*s*σ_g (**292.7 eV**) Rydberg transition is the strongest of all the Rydberg transitions, even in the dipole regime. This is due to vibronic coupling and breakdown of the Born-Oppenheimer approximation upon which is based the classification of the C 1*s* $\sigma_g \rightarrow$ 3*s*σ_g transition as a dipole forbidden transition. In a study by Kosugi [K96], ion yields in the 90° direction are found to be dominant, indicating that the bending vibration is predominantly coupled with the 3*s*σ_g Rydberg state and the intensity-lending dipole allowed state is the very strong ${}^1\Pi_u$ state at 290.74

Table 6.1 Calculated and observed energies (eV) of C 1*s* spectral features of CO_2.

Energy (eV)					
This work		Literature	Term Value	Width	
Expt.	Theory		(eV)	type[a]	Assignment
290.74[b]	290.89	290.77[c]	6.7	1.20 (G)	$2\sigma_g \rightarrow 2\pi_u^*$
292.7	291.98	292.74[d]	4.8	1.20 (G)	$2\sigma_g \rightarrow 3s\sigma_g$
294.7	294.8	294.96[d]	2.8	1.30 (G)	$2\sigma_g \rightarrow 3p\pi_u$
295.1	296.0[e]		2.4	1.30 (G)	$2\sigma_g \rightarrow 3p\sigma_u$
296.6		296.38[d]	0.9	1.30 (G)	$2\sigma_g \rightarrow$(4*p*+other Ryd.)
		297.5[f]		1.25 (E)	IP
298.0 (sharp)					2e
298 (broad)				5.83 (G)	$2\sigma_g \rightarrow 5\sigma_g^*$
300 (sharp)					2e
303.3		~303[c]		3.64 (G)	2e
312.3		~312[c]		8.72 (G)	$2\sigma_g \rightarrow 4\sigma_u^*$

[a]G = Gaussian profile, E = error function edge shape

[b]All energies were established by calibrating the C 1*s* ($2\sigma_g \rightarrow 2\pi_u^*$) transition to this well-established value [SB84]

[c]Ref. [WB74]

[d]Ref. [MCM&91]

[e]This value may be overestimated as it is the second CI root

[f]Ref. [JBE84]

eV. On the other hand, in the $4s\sigma_g$ Rydberg state, vibronic coupling through the antisymmetric stretching mode is clearly observed in the 0° direction.

More generally, recent work [AKS&95, RDP&92, HSD&93, RDK93, STR&93, UOC&95] has opened up clear evidence of vibronic coupling and Rydberg-valence mixing in inner-shell spectroscopy, specifically in CO_2 [WB74, TKR79, MCM&91, SB76].

The peak observed at **295.62** eV was tentatively assigned to the 3d Rydberg state by Ma *et al.* [MCM&91]. The effective quantum number n* for this peak is 2.56. It is usual that the quantum defects for the *n*d Rydberg series are nearly zero. The n* number for the $3s\sigma_g$ Rydberg state is 1.66 and the n* for the 3p Rydberg state is 2.23. Therefore, it is more reasonable that this peak is assigned to the $4s\sigma_g$ Rydberg excited state. Also, the 3*s* and 4*s* Rydberg excitations do not have the same quantum defects, due to strong valence mixing in the $3s\sigma_g$ Rydberg state as predicted theoretically by Schwarz and Buenker [SB76].

The transition to the $4s\sigma_g$ Rydberg state is also dipole-forbidden and should borrow its intensity from dipole-allowed states through the vibronic coupling as well as the $3s\sigma_g$ Rydberg state. It was observed [K96] that the vibronic coupling through the antisymmetric stretching mode is relatively enhanced in the $4s\sigma_g$ Rydberg excited state probably because the $4s\sigma_g$ state approaches an intensity-lending state with the Σ_u^+ symmetry and goes away from the π^* resonance.

The weak structures indicated by * in Fig. 6.1 just above the C 1*s* IP and the relatively strong signal at 303 eV are double electron excitations - simultaneous C 1*s* → π* excitation and a valence electron excitation.

At both large and small momentum transfer the spectrum is dominated by the intense π* peak at 290.74 eV and by the broad continuum resonance at 312 eV. However there is a dramatic fall-off in scattering intensity as the scattering angle increases - the as-recorded 32° spectrum is about 500-fold weaker than that at 4°. This is partly due to the rapid decrease of the excitation cross section with increasing angle, but it also reflects reduced overlap of the incident electron beam and analyzer acceptance cone. The geometry-corrected cross-section varies by a factor of 360 while the GOS varies by a factor of 15 between these two angles.

Although the spectra at 4° and 32° (Fig. 6.1) seem quite similar, the ratio of the intensity of the $2\pi^*/4\sigma_u^*$ transitions differs by 30% and there are significant changes in the 294 eV to 305 eV region. **Figure 6.2** presents this latter region in greater detail, in comparison to the optical spectrum [GGS&98] (Note that the higher resolution optical data has been broadened to match the lower resolution energy loss data). Careful examination of Figs. 6.1 and 6.2 shows that a SHARP peak appears at 298.2 while the intensity of the sharp peak at 300 eV increases at higher *K*. The sharp features at 296.5, 298.2, 300 and 303 eV are multi-electron excitations superimposed on a broad continuum resonance. In addition to the changes in the relative intensities of the sharp features, a broad structure develops between 296 and 300 eV with increasing momentum transfer. The latter feature is absent at small scattering angles, and gets much stronger at large

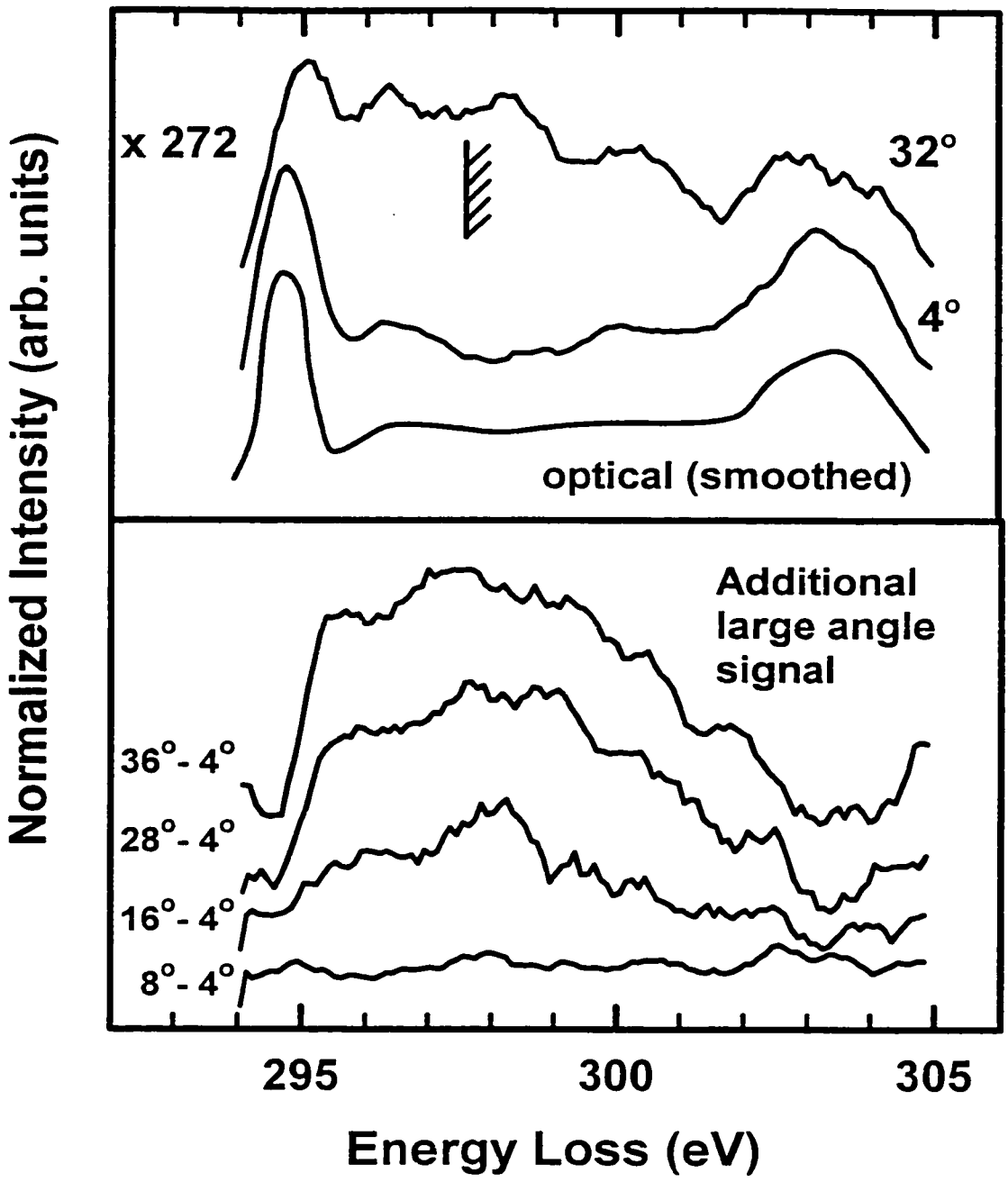

Fig. 6.2 Detail of the 294 to 305 eV region; (top) the data at 4°, 32° and the optical spectrum [GGS&98]; (bottom) higher scattering angle spectra after subtraction of the 4° spectrum. The broad intensity around 298 eV is assigned to the C 1*s* ($2\sigma_g \rightarrow 5\sigma^*_g$) dipole forbidden transition.

angles – characteristic of a dipole-forbidden excitation. In order to better reveal the shape of this additional non-dipole signal, the 4° signal has been subtracted from each of the spectra at higher scattering angles. The difference spectra, smoothed to reduce noise, are shown in the lower panel of Fig. 6.2. The mean energy position of the broad signal is ~ 298 eV and its width is ~ 4 eV FWHM. This broad signal is assigned to the electric dipole forbidden, electric quadrupole allowed, $X\ ^1\Sigma_g^+ \rightarrow (C\ 1s\ \sigma_g^{-1},\ 5\sigma_g^*)\ ^1\Sigma_g^+$ transition.

The residual sharp signal in the difference spectra is believed to be incompletely subtracted double excitation signal because of variations in their K^2 dependence. The second C1s→σ* transition, the dipole allowed C 1s ($2\sigma_g \rightarrow \sigma_u^*$) transition occurs around 312 eV (see Fig. 6.2). Thus the difference in the energies of the C 1s ($2\sigma_g \rightarrow 5\sigma_g^*$) and C 1$s$ ($2\sigma_g \rightarrow 4\sigma_u^*$) excitations is ~ 14 eV. This value is very similar to the σ_g - σ_u energy difference in the O 1s spectrum (16 eV) and that derived from other techniques [HS87, TAP79, FLK84]. This is the first reported observation of the dipole forbidden C 1s → σ* ($5\sigma_g$) transition.

6.2.A.2. O 1s Excitation

Figure 6.3 shows examples of O 1s energy loss spectra of CO_2 recorded under small and large momentum transfer conditions. The experimental and theoretical energies and assignments for the O 1s spectral features are presented in **Table 6.2**. The energies and GOS profiles for excitations from the $1\sigma_g$ and $1\sigma_u$ orbitals to $2\pi_u$, $3s\sigma_g$, $3p\sigma_u$, $3p\pi_u$, and $4s\sigma_g$ orbitals, were calculated within the Generalized Multistructural

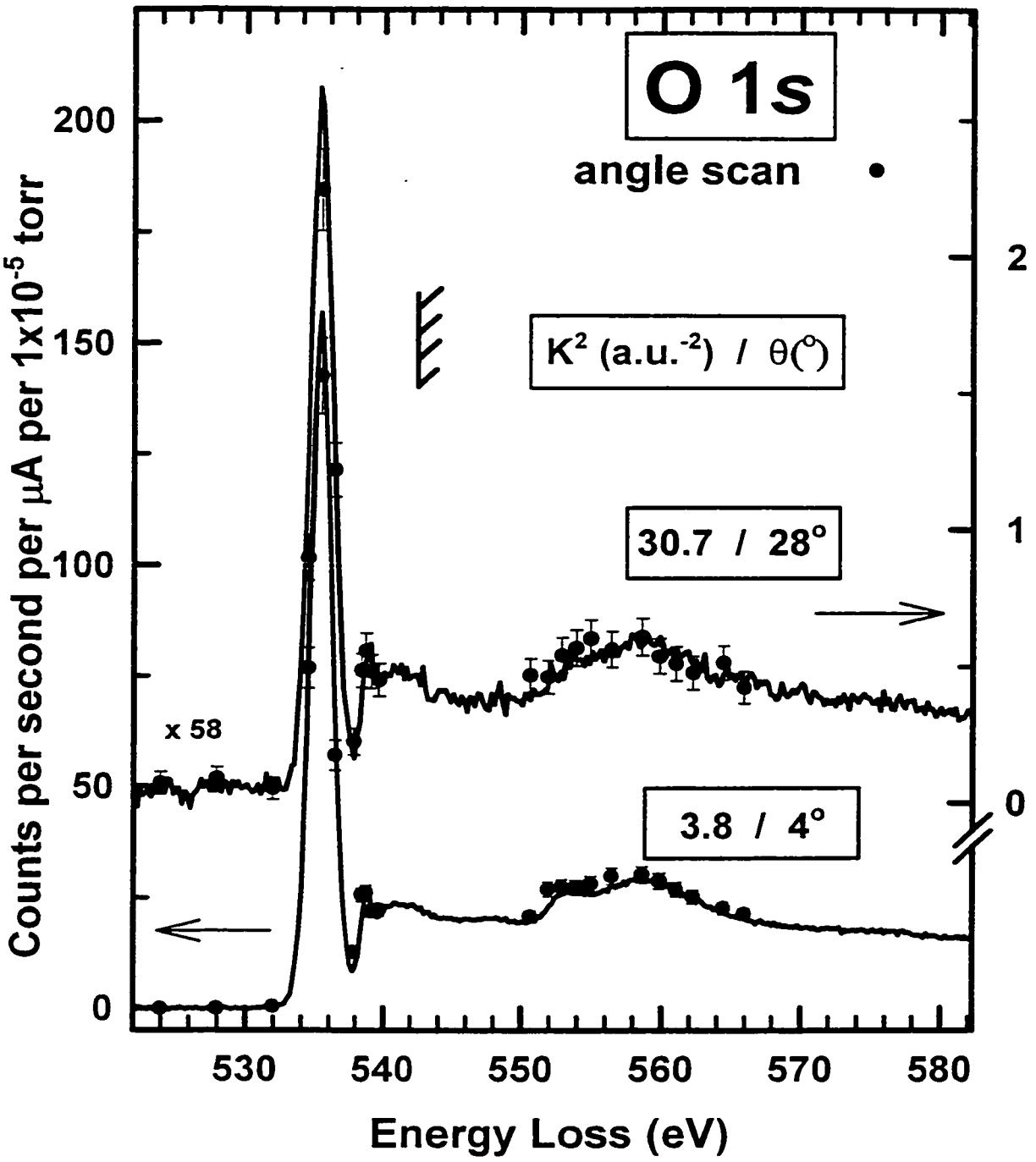

Fig. 6.3 Comparison of the O 1*s* energy loss spectra of CO_2 at 4° and 28°. The hatched line indicates the O 1*s* IP as determined by X-ray photoelectron spectroscopy [JBE84].

Table 6.2 Calculated and observed energies (eV) of O 1*s* spectral features of CO_2.

Energy (eV) This work			Term Value (eV)	Width (type)[a] (eV)	Assignment
Expt.(eV)	Theory(eV)	Literature (eV)[b]			
535.4[c]	535.5	535.4	5.4	1.81 (G)	$1\sigma_g \rightarrow 2\pi_u^*$
	535.7				$1\sigma_u \rightarrow 2\pi_u^*$
-[d]	535.7				$1\sigma_g \rightarrow 3s\sigma_g$
-	536.9				$1\sigma_u \rightarrow 3s\sigma_g$
538.8	538.0	538.7	2.0	0.71 (G)	$1\sigma_u \rightarrow 3p\sigma_u$
"	538.0				$1\sigma_g \rightarrow 3p\sigma_u$
538.8	539.3				$1\sigma_u \rightarrow 3p\pi_u$
"	539.6				$1\sigma_g \rightarrow 3p\pi_u$
538.8	540.3				$1\sigma_g \rightarrow 4s\sigma_g$
"	540.3				$1\sigma_u \rightarrow 4s\sigma_g$
540.3			0.5	1.63 (G)	higher Ryd.
	540.8			1.75 (E)	IP
541.6	541.9			3.88 (G)	$1\sigma_g \rightarrow 5\sigma_g^*$
					$1\sigma_u \rightarrow 5\sigma_g^*$
553.2	553.0			1.96 (G)	2e
558.9	558.0			9.68(G)	$1\sigma_g \rightarrow 4\sigma_u^*$
					$1\sigma_u \rightarrow 4\sigma_u^*$

[a]G = Gaussian profile, E = error function edge shape

[b]Ref. [WB74]

[c]All spectra were calibrated to the O 1*s* ($1\sigma_g \rightarrow 2\pi_u^*$) transition at 535.4 eV [SB84]

[d]If the assignment of the 539 eV peak is correct (mainly $4s\sigma_g$) then the position of the $3s\sigma_g$ transition is as-yet unknown. It may be masked by the high energy side of the strong $2\pi_u^*$ feature.

Method [ETH&99]. For each final state the energy difference between excitations from the $1\sigma_g$ and $1\sigma_u$ orbitals are less than 0.3 eV, except for the $3s\sigma_g$ final state where it is equal to 1.2 eV. As for the C 1*s* region, the theoretical and experimental O 1*s* energy values agree within 1 eV except for the $4s\sigma_g$ final states. The $4s\sigma_g$ is the second CI root with σ_g symmetry and therefore the excitation energy may be less precise.

The spectroscopic interpretation of the O 1*s* spectrum of CO_2 has been described in detail elsewhere [GGS&98]. The O 1*s* spectra at large and small momentum transfer are quite similar, aside from the change in intensity. Between 4° and 28° the as-recorded intensity drops by a factor of 58, the geometry-corrected cross-section varies by a factor of 25, and the GOS ratio is ~ 3, after the kinematic correction. (Note that the relative decline in the O 1*s* signal with increasing momentum transfer is much less than that observed in the C 1*s* case).

At both small and large angle, the O 1*s* spectrum is dominated by excitations to the $2\pi_u$* feature at 535.4 eV.

Initially, the second peak at 539 eV was attributed to overlap of the $3p\sigma_u$ and $3p\pi_u$ Rydberg states [CLL75]. Later, this feature was reassigned to the overlap of the 3*s* and 3*p* Rydberg states [SYK&89]. Symmetry resolved ion-yield studies [BSS95] have shown that the 539 eV peak results mainly from excitations to orbitals of σ symmetry. Based on a combination of theory and X-ray emission spectroscopy, Gunnelin *et al.* [SYK&89] have confirmed that the 539 eV peak corresponds to excitation to states of mainly σ symmetry, and they have assigned it to a combination of $3p\sigma_u$ and $4s\sigma_g$ Rydberg states. They suggest that the $4s\sigma_g$ makes the stronger contribution and that the $3p\sigma_u$ transition

occurs at slightly lower energy than the $4s\sigma_g$ transition. The present theoretical OOS values of the $3p\sigma_u$, $3p\pi_u$ and $4s\sigma_g$ optically allowed excitations are 0.0020, 0.0016 and 0.0039 respectively, confirming that the $4s\sigma_g$ is the strongest among the three optically allowed excitations that contribute to the 539 eV band. The theoretical MC-CI OOS values of Gunnelin *et al.* [SYK&89] are respectively 0.0006, 0.0001 and 0.0047. The agreement between the present result and that of Gunnelin *et al.* [SYK&89] for the $4s\sigma_g$ process is good, but for the other two processes, calculations predict larger OOS values.

The $5\sigma_g$* shape resonance occurs at 541.6 eV, just above the ionization limit (540.8 eV [JBE84]).

At higher energies, there are weak contributions from double excitations around 553 eV followed by the strong $4\sigma_u$* shape resonance at 559 eV. The σ_g and σ_u continuum resonances are both observed at all scattering angles since the O 1*s* ($1\sigma_u \rightarrow 5\sigma_g$*) and the O 1*s* ($1\sigma_g \rightarrow 4\sigma_u$*) are electric dipole allowed. It is interesting that the higher energy O 1*s* ($1\sigma_g \rightarrow 4\sigma_u$*) resonance is stronger than the lower energy O 1*s* ($1\sigma_u \rightarrow 5\sigma_g$*) resonance. Normally the lowest energy core excitation in a given manifold is the strongest on account of core hole relaxation. Investigation of the spatial distributions of the $5\sigma_g$* and $4\sigma_u$* orbitals may explain this anomaly.

6.2.B Generalized Oscillator Strengths (GOS)

Examples of the curve fits used to extract integrated peak areas from the experimental C 1*s* and O 1*s* spectra are presented in **Figure 6.4** while the fit parameters

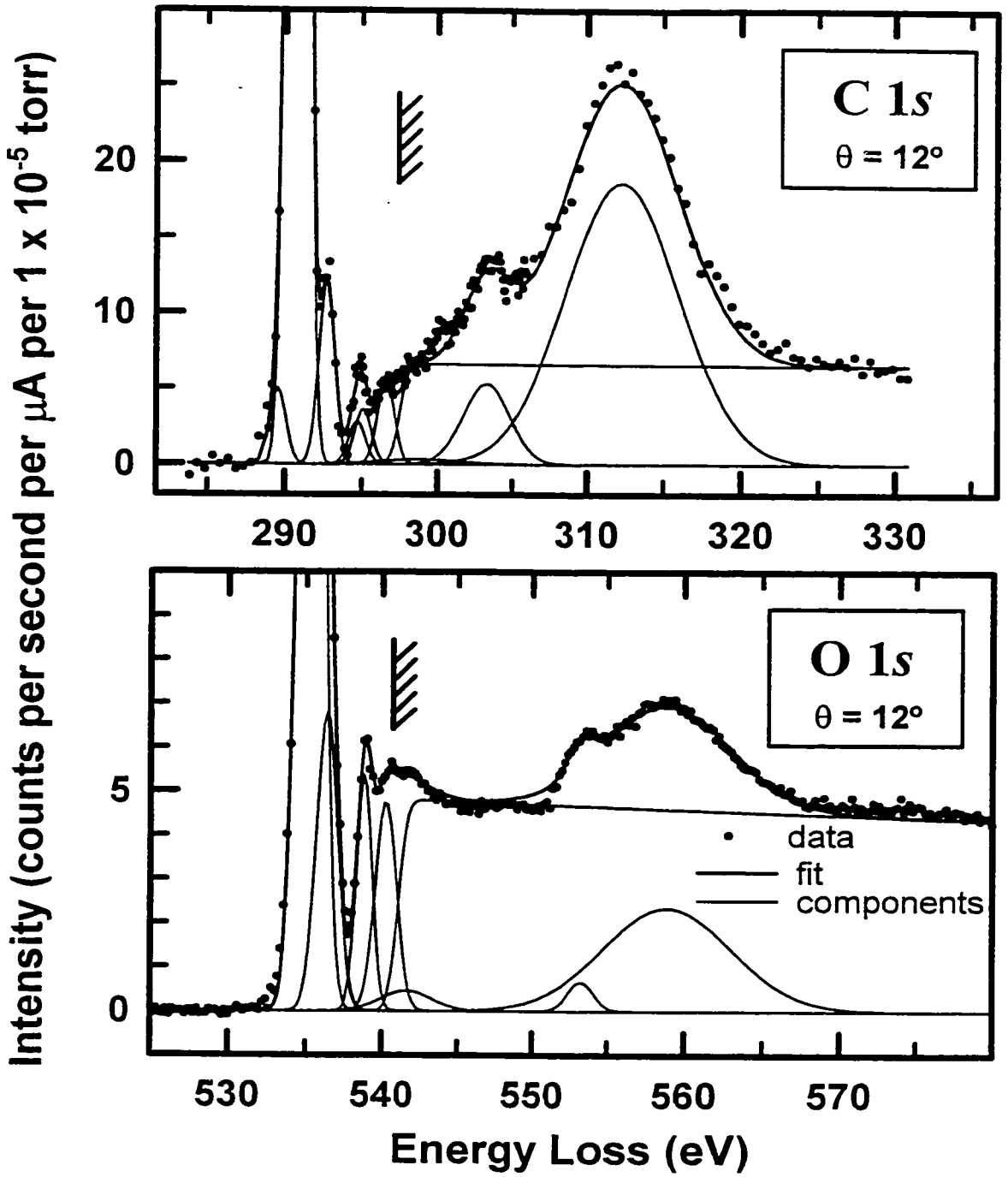

Fig. 6.4 Curve fits to the C 1*s* and O 1*s* spectra recorded at 12°, using the standardized multi-file curve-fit approach described in the text. The line through the data points represents the least-squares fit; each peak is represented by a Gaussian function; the continua are represented by an error function.

are summarized in the spectral assignment tables, 6.1 and 6.2. The curve fits at all angles were of similar quality to those displayed in Fig. 6.4.

6.2.B.1. C 1*s* GOS profiles

GOS profiles, up to K^2 = 65 a.u.$^{-2}$, were derived for all resolved C 1*s* spectral features using curve fits to the measured spectra and the procedures outlined in chapter 4.

Figure 6.5 compares the experimental and theoretical GOS profiles for the C 1*s* ($2\sigma_g \rightarrow 2\pi_u^*$) transition for K^2 values between 1.5 and 65 a.u.$^{-2}$. **Figure 6.6** plots the experimental and theoretical GOS profiles for the C 1*s* ($2\sigma_g \rightarrow 3s\sigma_g$) transition. **Figure 6.7** plots the experimental and theoretical GOS profiles for the C 1*s* ($2\sigma_g \rightarrow 3p\pi_u$) and C 1*s* ($2\sigma_g \rightarrow 3p\sigma_u$) transitions, and the experimental GOS profile for the C 1*s* ($2\sigma_g \rightarrow 5\sigma_g^*$) excitation. **Figure 6.8** presents the experimental GOS profiles for C 1*s* ($2\sigma_g \rightarrow$ higher Rydberg excitations), for C 1*s* ($2\sigma_g \rightarrow$ double electron excitation), for continuum C 1*s* ($2\sigma_g \rightarrow 4\sigma_u^*$) shape resonance, and the non-resonant C 1*s* continuum integrated from 326 to 330 eV. In most cases Lassettre fits to the GOS are also plotted. The Lassettre parameters are summarized in **table 6.3**.

Figure 6.5 shows that there is good agreement between the present and previous [BBS91] experimental results, as well as the present and previous [MB93] theoretical results for the C1*s* ($2\sigma_g \rightarrow 2\pi_u^*$) transition. It is surprising that the experimental and theoretical results for the GOS are in such good agreement to such high momentum transfer. A similar level of agreement is seen in Figure 6.7 for the C1*s* ($2\sigma_g \rightarrow 3p\pi_u$) excitations.

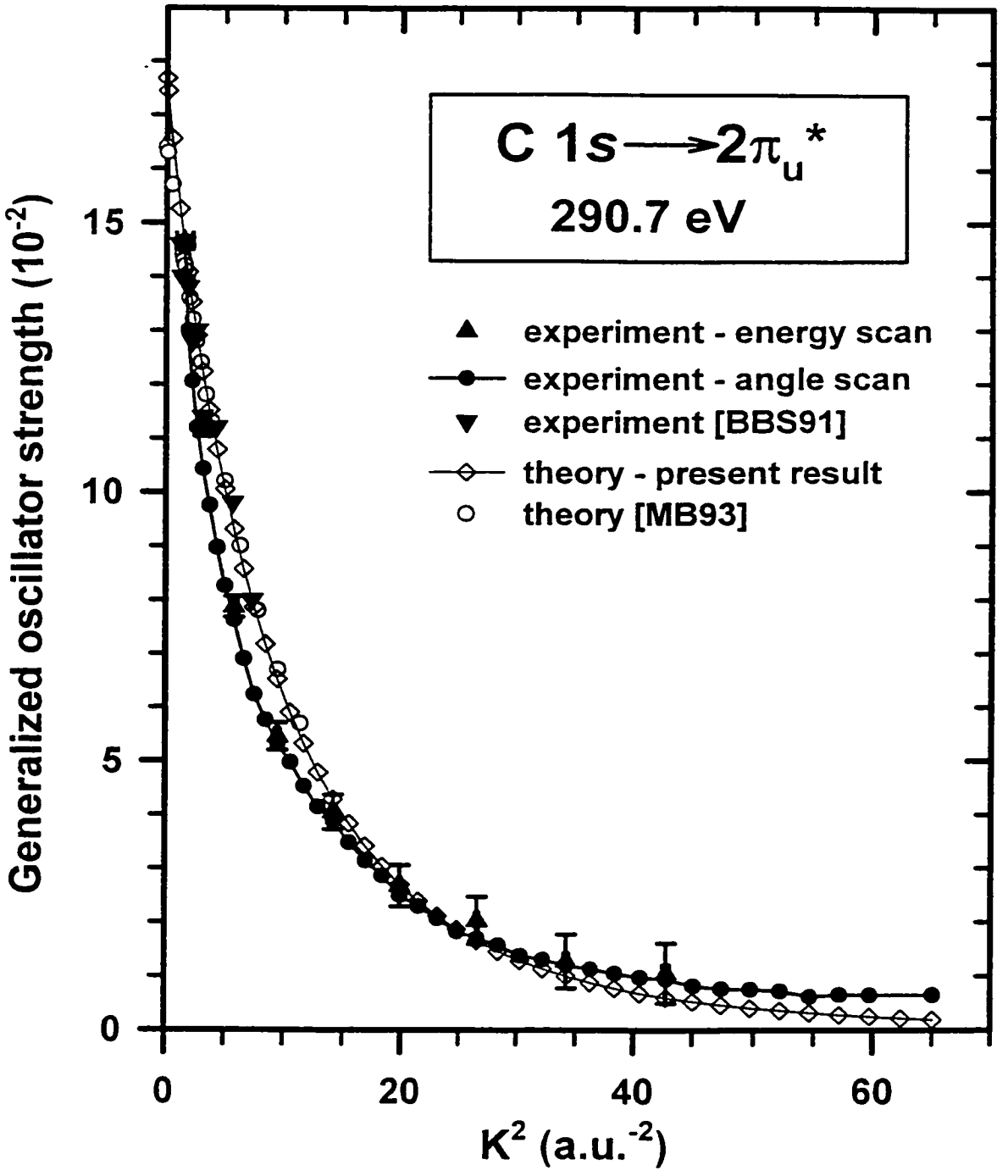

Fig. 6.5 Experimental and computed GOS profiles for the C 1*s* ($2\sigma_g \longrightarrow 2\pi^*_u$) transition, in comparison to previously reported experimental [BBS91] and computed values [MB93].

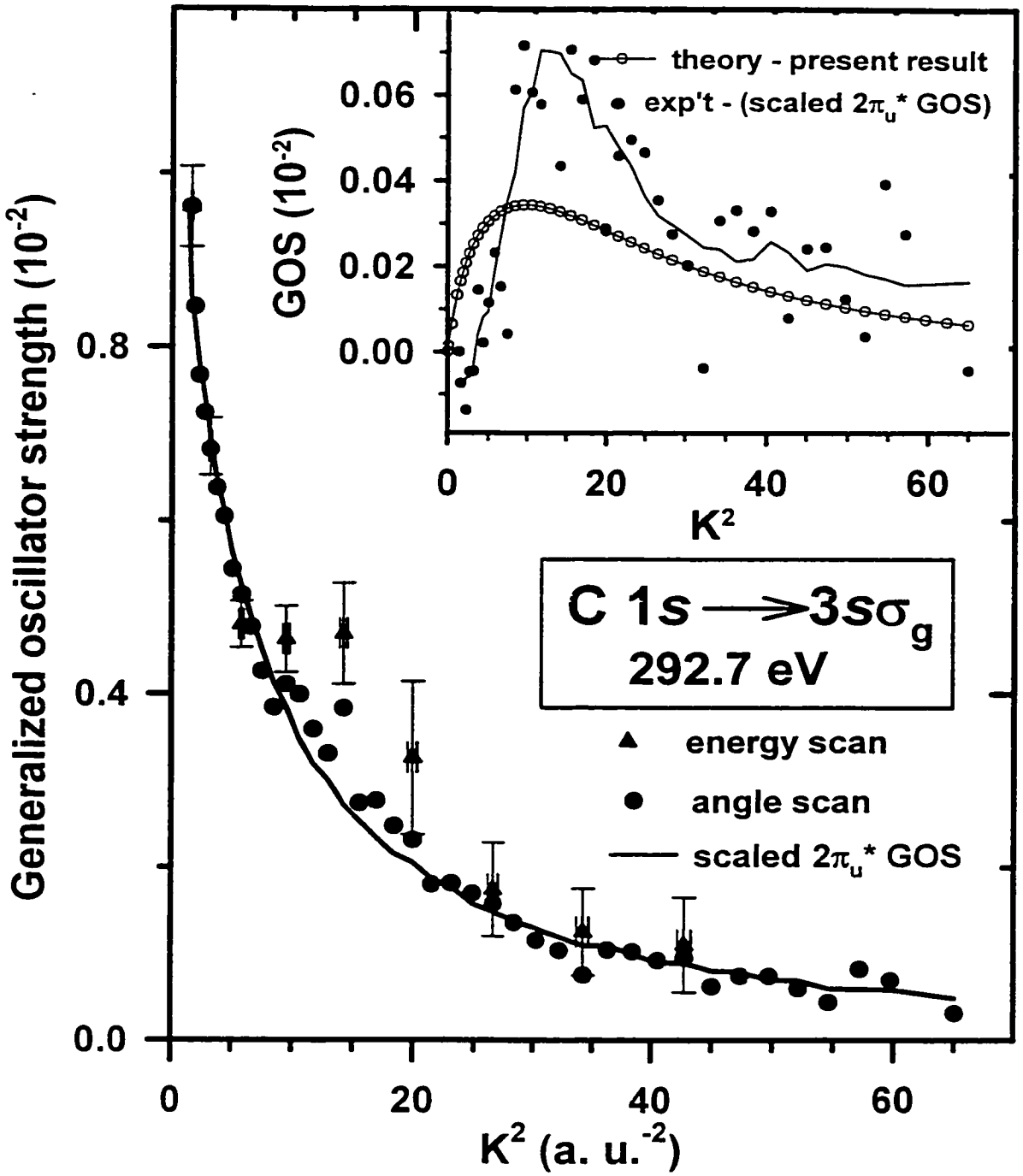

Fig. 6.6 Experimental GOS profile for the C 1*s* ($2\sigma_g \rightarrow 3s\sigma_g$) transition. The insert plots the computed GOS profile for the direct quadrupole transition in comparison to an estimate of the non-dipole component of the C 1*s* ($2\sigma_g \rightarrow 3s$) GOS generated by subtracting a scaled version of the GOS for the C 1*s* ($2\sigma_g \rightarrow 2\pi^*_u$) transition, as an estimate of the dipole vibronic component.

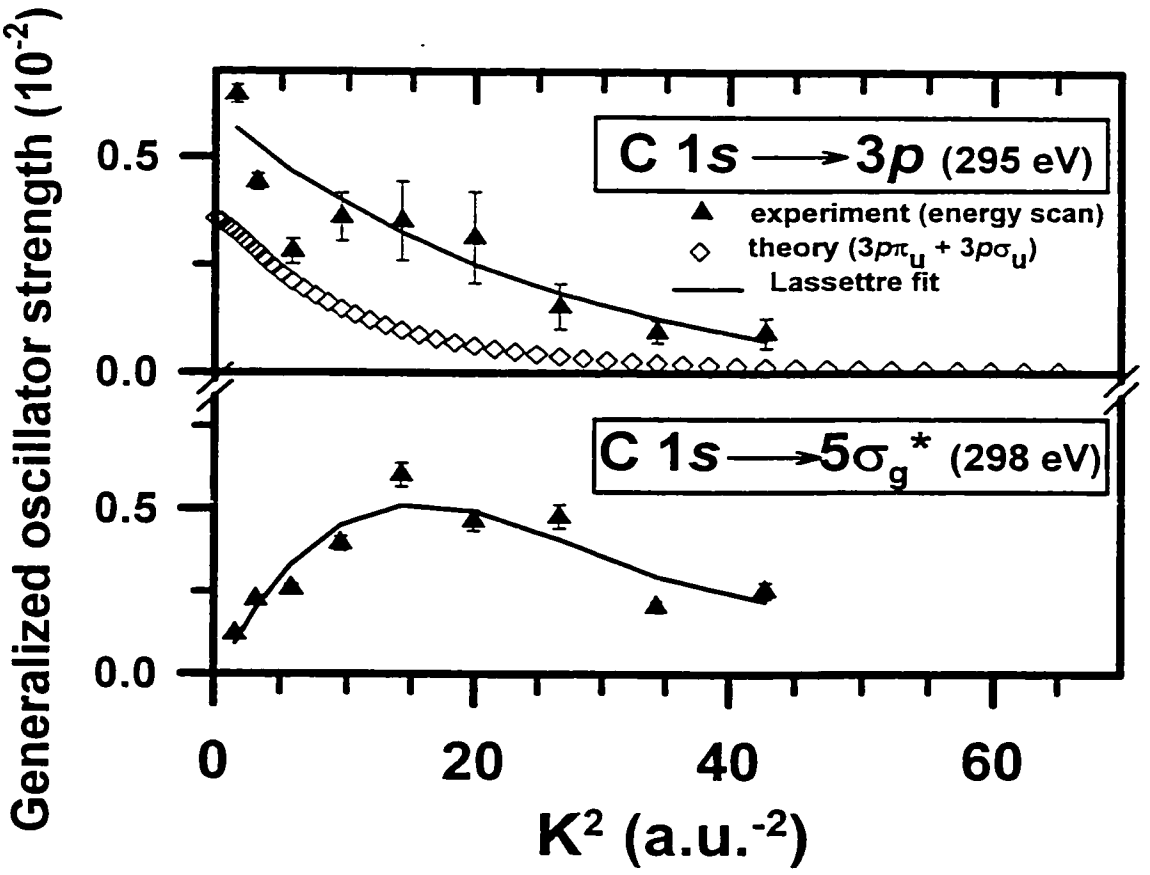

Fig. 6.7 (upper) Experimental and computed GOS profiles for the C 1*s* ($2\sigma_g \rightarrow 3p\pi_u/3p\sigma_u$) transition. (lower) Experimental GOS profile for the broad signal at 298 eV, assigned as the C 1*s* ($2\sigma_g \rightarrow 5\sigma^*_g$) resonance. The lines correspond to semi-empirical fits using Lassettre series.

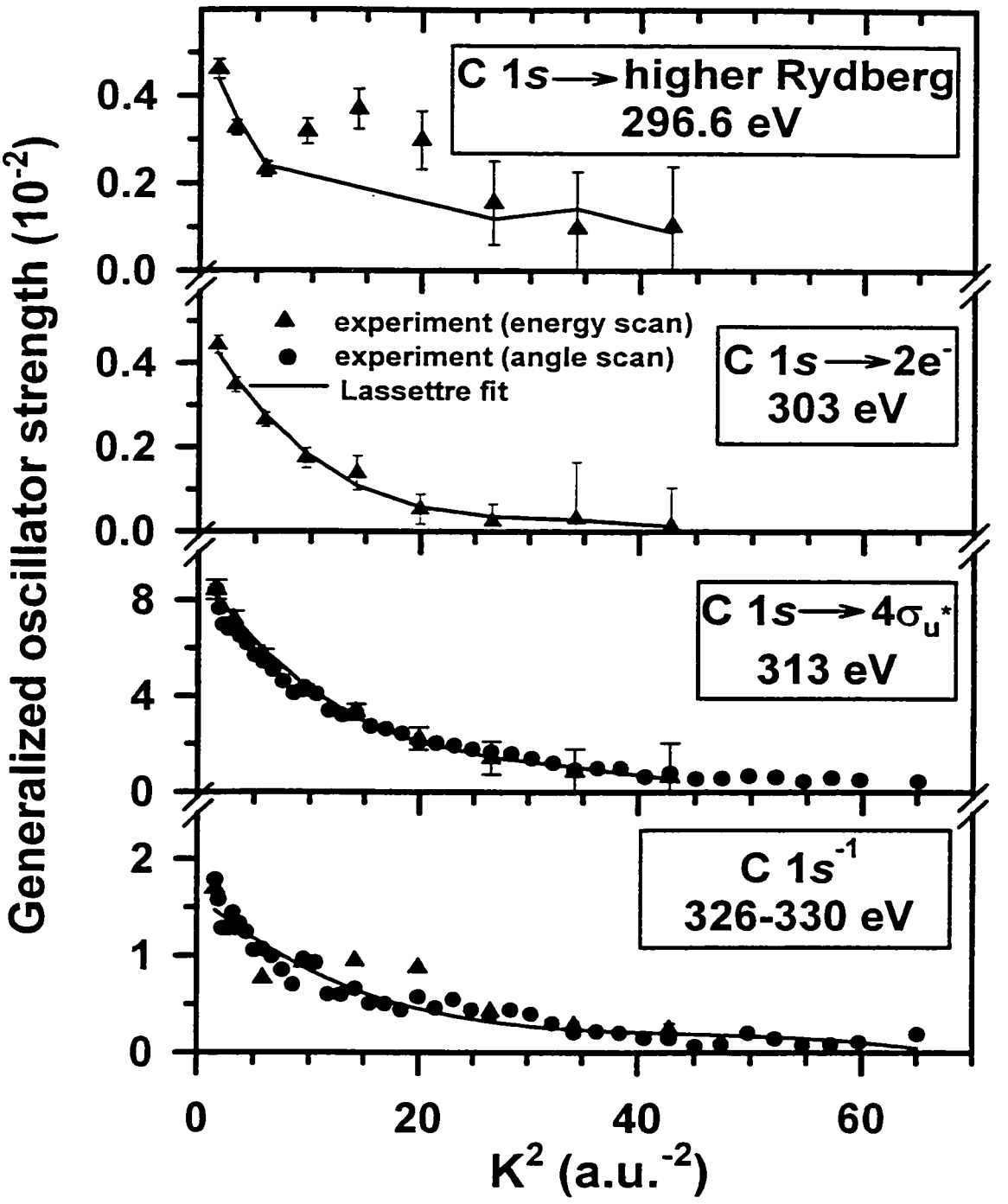

Fig. 6.8 Experimental GOS profiles for the C 1*s* ($2\sigma_g$→ higher Rydberg), the C 1*s* ($2\sigma_g$→ double excitation), the C 1*s* ($2\sigma_g$→ $4\sigma^*_u$) and the C 1*s* continuum integrated over 326-330 eV.

Table 6.3 Lassettre parameters for GOS for C 1*s* and O 1*s* core excitations of CO_2

		f_0 x10^{-2}	f_1	f_2	f_3 x10	f_1/f_0 x10	f_2/f_0 x10^2	f_3/f_0 x10^3
C 1*s*	$3p\pi_u$	0.4	-0.2	5.1	-5.2	-5.1	13	-18
	$3p\sigma_u$	0.2	-0.02	0.1	-3.4	-1.0	0.5	-0.2
	$5\sigma_g$*	0.03	0.6	-15	11	180	-470	350
	R	0.5	-0.4	13	-12	-8.1	24	-52
	$2e^-$	0.5	-0.3	8.1	-6.8	-6.7	17	-14
	$4\sigma_u$*	9.3	-5.8	150	-140	-6.2	16	-15
O 1*s*	$2\pi_u$*	11	-8.4	300	-410	-7.6	28	-38
	R	1.7	-1.6	63	-8.1	-9.4	37	-47
	$5\sigma_g$*	0.8	-0.8	34	-43	-10	43	-55
	$2e^-$	0.4	-0.3	9.7	-9.8	-7.9	25	-25
	$4\sigma_u$*	4.9	-3.9	120	-130	-7.9	25	-26

This is surprising since, although the target wave functions were carefully constructed considering relaxation and correlation effects, the FBA was used to describe the collision process between the incident electron and the target. The FBA considers only the first order term in the Born expansion for the interaction potential between the incident electron and the molecule. For this reason, it should not describe properly situations where the interaction is strong, which is the situation expected for large scattering angle events. For valence excitation with high energy electron impact, the FBA result agrees with experimental results only for small values of the transferred momentum (typically up to $K^2 < 2 - 5$ a.u.$^{-2}$) [RBB98]. For larger values of the transferred momentum and scattering angles the agreement between the experimental and the FBA result is generally poor because it corresponds to a situation where classically the incident electron penetrates further into the molecule, which means that the interaction is stronger. Theoretical GOS for valence excitation in the higher momentum transfer regime must consider higher order terms in the Born expansion or through other methods such as close-coupling or distorted wave calculations.

In a previous theoretical and experimental study of the GOS for inner-shell excitation of C_2H_2 [MBB&94], unexpectedly good agreement, up to $K^2 \approx 13$ a.u.$^{-2}$ was also found. It is surprising to observe in Figures 6.5 and 6.7 relatively good agreement between the experimental and theoretical results for even higher values of K^2, that is, up to $K^2 = 60$ a.u.$^{-2}$. This suggests that the dynamics of the collision process for inner-shell excitation may be qualitatively different from those for valence excitation. The GOS for

inner shell excitation of other molecules should be measured and compared to GOS computed within the FBA to see if this is a general phenomenon.

The experimental and theoretical GOS profiles for the C 1*s* ($2\sigma_g \rightarrow 3s\sigma_g$) transition (Figure 6.6) are in strong disagreement. This is because, although the C 1*s* ($2\sigma_g \rightarrow 3s\sigma_g$) transition is electronically dipole forbidden, there is strong vibronic coupling to the intense near by C 1*s* ($2\sigma_g \rightarrow 2\pi_u^*$) excitation [K96]. The vibronic channel has not been included in the present calculation, which only reports the GOS for the direct quadrupole excitation which has a predicted value of zero at $K = 0$, increases to a maximum at $K^2 \sim 8$ a.u^{-2}, and then decreases – a behavior typical of an optically forbidden process [TFT&95, FTT&95], rather than the observed monotonically decreasing GOS, which is typical of a dipole allowed process. Since the main intensity of the C 1*s* ($2\sigma_g \rightarrow 3s\sigma_g$) transition comes from the vibronic coupling to the C 1*s* ($2\sigma_g \rightarrow 2\pi_u^*$) excitation, the GOS shape for the 3*s* vibronic component might be similar to that for the $2\pi^*$ GOS. Making this assumption, the GOS for the direct C 1*s* ($\sigma_g \rightarrow 3s\sigma_g$) quadrupole component was estimated by subtracting the GOS for the C 1*s* ($2\sigma_g \rightarrow 2\pi_u^*$) excitation scaled to that of the 3*s* in the low momentum transfer region, as an estimate of the vibronic signal. The results of this treatment are shown in the insert to Figure 6.6. Although the agreement is by no means perfect, the residual is at a similar intensity and roughly similar shape to that calculated for the direct quadrupole C 1*s* ($2\sigma_g \rightarrow 3s\sigma_g$) transition.

The upper panel of Figure 6.7 compares the C 1*s* ($2\sigma_g \rightarrow 3p$) theoretical GOS profile to the experimental GOS profile for the feature at 294.7 eV. There is relatively

good agreement up to very high values of momentum transfer. Both theoretical and experimental results show that the major contribution to the intensity of the C 1*s* ($2\sigma_g \rightarrow 3p$) transition comes from the C 1*s* ($2\sigma_g \rightarrow 3p\pi_u$) channel, while the C 1*s* ($2\sigma_g \rightarrow 3p\sigma_u$) channel has a significantly smaller contribution. The lower panel of Figure 6.7 shows the experimental GOS derived for the broad signal around 298 eV, assigned to C 1*s* ($2\sigma_g \rightarrow 5\sigma_g$) $^1\Sigma_g^+$ excitation. The dipole forbidden character of this quadrupole excitation is clearly indicated by the shape of its GOS profile which extrapolates to zero for small momentum transfer, increases to a maximum at $K^2 \sim 10$ a.u.$^{-2}$, then decreases again at higher values of K^2. This is the expected behavior for the GOS of an electric dipole forbidden, electric quadrupole allowed transition. Two σ-shape resonances have been predicted for core ionization of CO_2 [DDH82, LM82]. The well known C 1*s* ($2\sigma_g \rightarrow 4\sigma_u^*$) shape resonance is dipole allowed. The second one is the C 1*s* ($2\sigma_g \rightarrow 5\sigma_g^*$) shape resonance which was observed at 298 eV for the first time in the present work.

Figure 6.8 shows the experimental GOS for C 1*s* ($2\sigma_g \rightarrow$ higher Rydberg excitations), for C 1*s* ($2\sigma_g \rightarrow$ double excitation), for continuum C 1*s* ($2\sigma_g \rightarrow 4\sigma_u^*$) shape resonance, and for the C 1*s* continuum integrated from 326 to 330 eV. Each of these GOS profiles decreases smoothly from a maximum value at $K^2 = 0$, consistent with dipole allowed transitions. There are no calculated values for the GOS for these features since they correspond either to unresolved high-*n* Rydberg transitions or to continuum processes, neither of which the theoretical methodology is not currently equipped to handle.

6.2.B.2. O 1*s* GOS profiles

Figure 6.9 presents all of the theoretical GOS profiles for O 1*s* excited CO_2. For each final orbital the individual components and the sum of the ($1\sigma_g$ + $1\sigma_u$) components are plotted. Both experiment and theory indicate that the GOS for the 535 eV peak – the sum of the ($1\sigma_g$ + $1\sigma_u$) contributions - has the overall form of an optically allowed process. Calculations predict that the dipole forbidden O 1*s* ($1\sigma_u \rightarrow 2\pi_u$) channel makes contributions of similar magnitude to the dipole allowed O 1*s* ($1\sigma_g \rightarrow 2\pi_u$) channel at all except very low momentum transfer (K^2 < 2 a.u.$^{-2}$), where there is a small drop in intensity as the quadrupole channel turns off. The energy difference between the O 1*s* ($1\sigma_u \rightarrow 2\pi_u$) and the O 1*s* ($1\sigma_g \rightarrow 2\pi_u$) transition is small, 0.2 eV according to the present calculations, as reported previously [MBN95], and thus they are not resolved. The existence of strong quadrupole contributions and overlap with the dipole partner is predicted not only for the O 1*s* $\rightarrow \pi^*$ transition, but also for all of the Rydberg states of O 1*s* excited CO_2, except the $3p\sigma_u$.

Table 6.4 summarizes the theoretical and the experimental OOS for the O 1*s* ($1\sigma_g$) $\rightarrow 2\pi_u$ transition. The present GMS theoretical result for the $2\pi^*$ OOS matches the values derived from small angle EELS [MCI&87] and a recent optical measurement [MCM&91]. The early report by Sivkov et al. [SAV&84] is clearly in error, possibly due to absorption saturation.

Figure 6.10 plots the experimental GOS of the $2\pi_u^*$ band at 535.4 eV compared with the sum of the theoretical values for the $1\sigma_g \rightarrow 2\pi_u^*$ and $1\sigma_u \rightarrow 2\pi_u^*$ processes. The

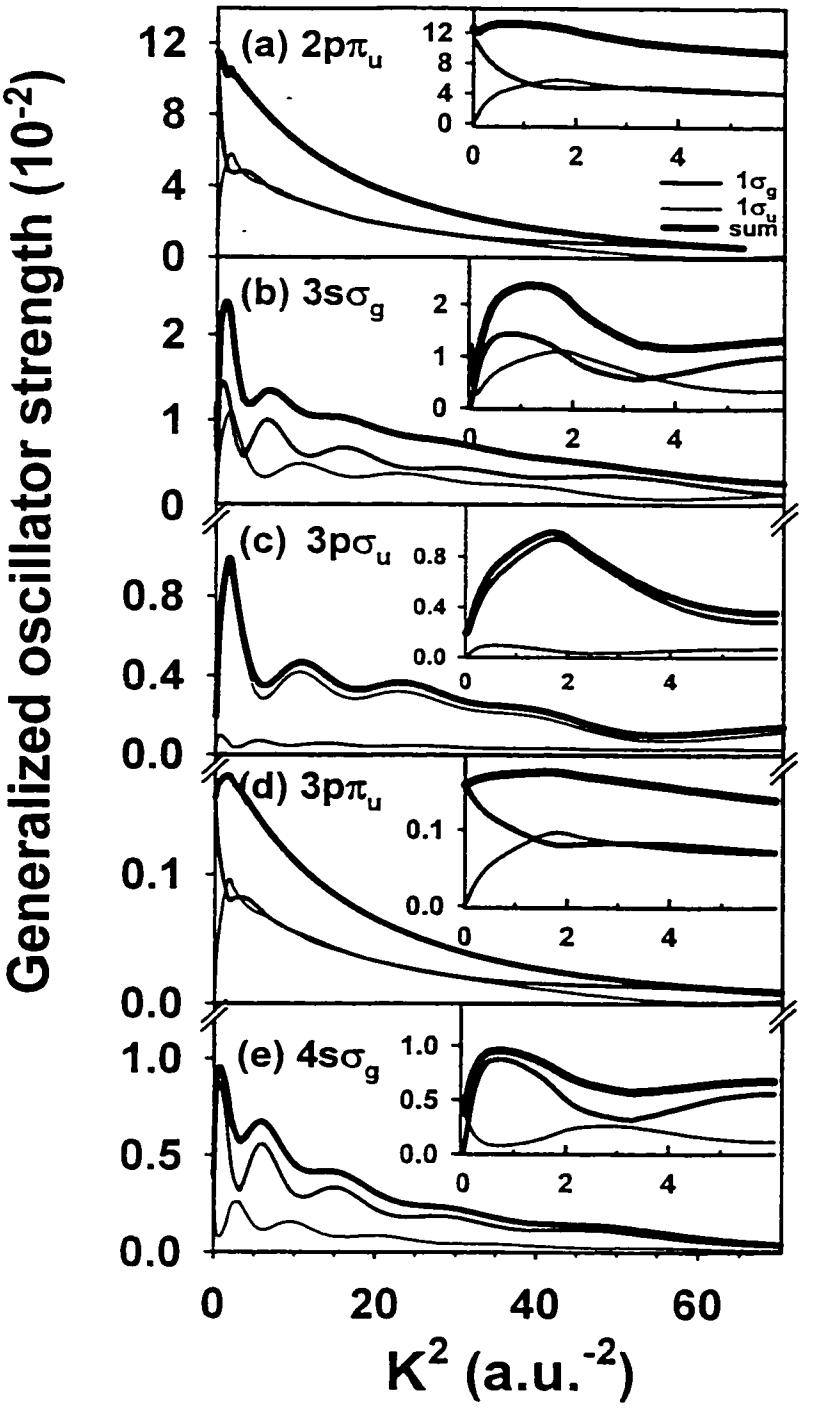

Fig. 6.9 Theoretical results for the O 1*s* GOS profiles. (a) $(1\sigma_g,1\sigma_u) \rightarrow 2\pi^*_u$ excitations; (b) $(1\sigma_g,1\sigma_u) \rightarrow 3s\sigma_g$ excitations; (c) $(1\sigma_g,1\sigma_u) \rightarrow 3p\sigma_u$ excitations; (d) $(1\sigma_g,1\sigma_u) \rightarrow 3p\pi_u$ excitations; (e) $(1\sigma_g,1\sigma_u) \rightarrow 4s\sigma_g$ excitations, together with the sum of the $(1\sigma_g+1\sigma_u)$ for each final orbital.

Table 6.4 Optical Oscillator Strengths (OOS) for $1s \rightarrow \pi^*$ excitations in CO_2

			OOS	
	Method	Ref.	C 1*s*	O 1*s*
theory	HF-FC[1]	MB93	0.257	0.125
	CI-FC[2]	MB93	0.233	0.147
	HF-R[3]	MB93	0.169	0.092
	CI-R[4]	MB93	0.164	0.12
	GMS-2S[5]	MB93		0.088
	GMS-3S[5]	MB93		0.084
	GMS-CI[5]	MB93		0.093
	GMS-CI	(present work)		0.115
Exp't	EELS	MCI&87	0.160	0.12-0.13
	Photoabsorption	SAV&84	0.14	0.062[6]
	Photoabsorption	MCM&91		0.115(3)

[1]Hartree-Fock frozen-core approximation
[2]Configuration interaction frozen-core approximation
[3]Hartree-Fock approximation allowing all the atomic or molecular orbits to relax
[4]Configuration interaction approximation allowing all the atomic or molecular orbits to relax
[5]Generalized multistructural wavefunctions of differing quality
[6]Direct optical measurement; the OOS was measured from the peak area in fig. 2 of [SAV&84]; comparison of the spectral intensities to those from atomic calculations indicate problems with this data, possibly due to absorption saturation.

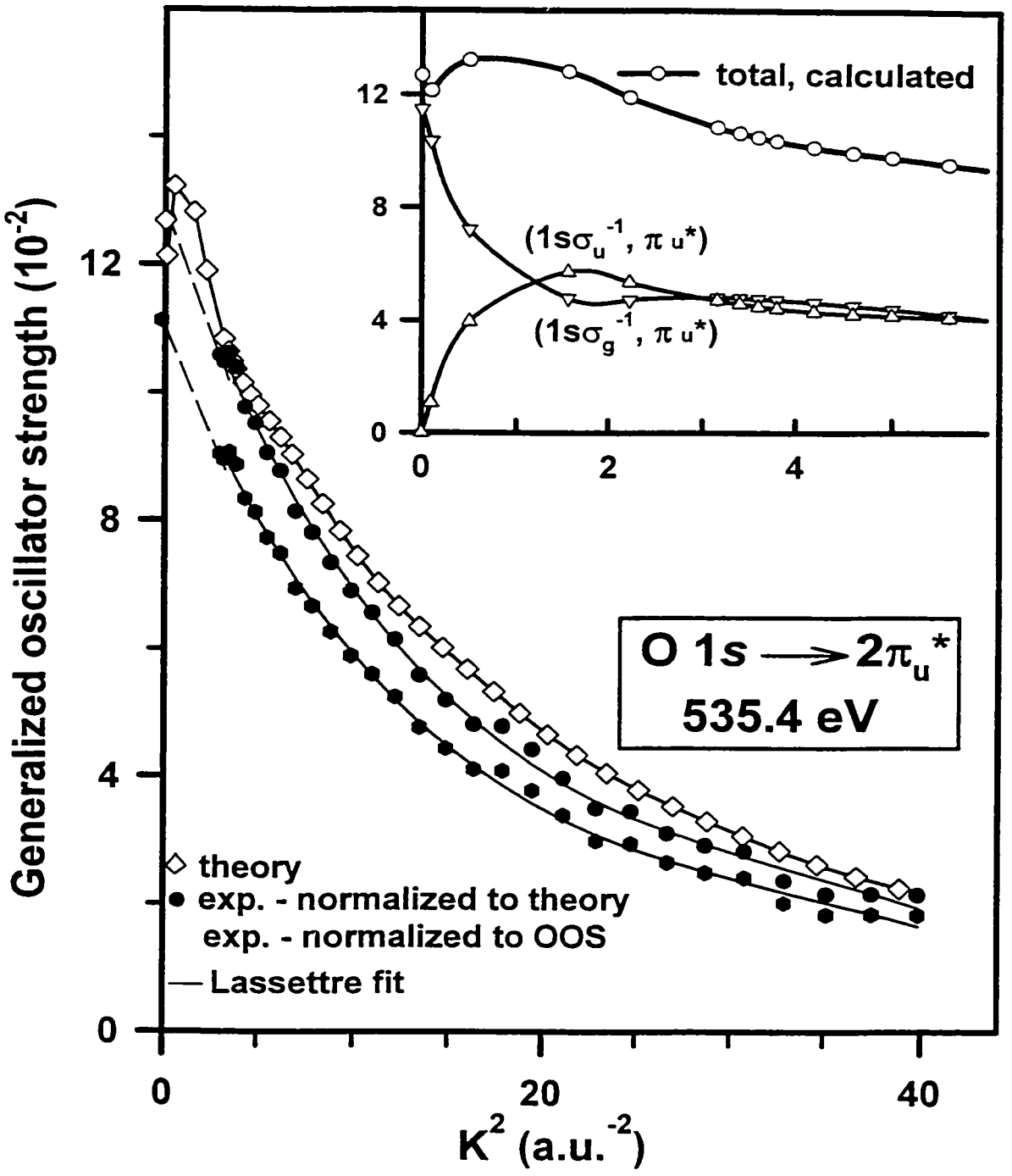

Fig. 6.10 Experimental GOS profiles for the O 1*s* ($1\sigma_g \rightarrow 2\pi_u$) transition normalized in two different ways (see text), compared to the calculated GOS. The theory profile includes the sum of the computed GOS for the O 1*s* $1\sigma_g \rightarrow 2\pi^*_u$ and $1\sigma_u \rightarrow 2\pi_u$ transitions. The insert shows the components and the sum for the theoretical values in the low-K region.

present theoretical results show that the 1*s* ($1\sigma_g \rightarrow \pi_u^*$) excitation is the major contribution to spectra obtained at very low K but for $K^2 > 3$ a.u.$^{-2}$, the contribution of the O 1*s* ($1\sigma_u \rightarrow \pi_u^*$) quadrupole transition is similar to that of the O 1*s* ($1\sigma_g \rightarrow \pi_u^*$) dipole transition. The very rapid turn-on of strong quadrupole contributions at small K^2 complicates the derivation of accurate GOS from the experimental measurements. Normally absolute GOS scales are set by extrapolating the relative GOS to $K^2 = 0$ and normalizing to experimental OOS values for the strongest process, the $2\pi^*$ band in this case. However, according to calculations, the optically forbidden $1\sigma_u \rightarrow 2\pi_u^*$ contributes strongly even below the minimum K^2 measured experimentally (~ 3 a.u.$^{-2}$). This leads to rapid variation of the GOS in the low-K^2 region and casts doubt on the validity of normalization via extrapolation of the measured relative GOS to $K^2 = 0$. To resolve this issue, low–K measurements between 1 and 3 a.u.$^{-2}$ are needed, but these cannot be made currently owing to voltage limitations of the apparatus. Instead, normalization to the theoretical results was also considered. In addition to the GOS derived by the normal extrapolation procedure, Figure 6.10 plots the GOS derived by normalizing to the theoretical value at $K^2 = 3.6$ a.u.$^{-2}$. Irrespective of the absolute scale, the experimental and computational results show good agreement in the overall shape of the GOS profile for the $2\pi_u^*$ state. Considering the GOS derived by normalization by the theoretical results, the experimental and computed GOS agree within ~ 10%. As for C 1*s* excitation, the shapes of the experimental and calculated O 1*s* GOS profiles agree to very large K^2 values, in apparent contradiction to an anticipated breakdown of the first Born approximation (see the discussion presented in section 6.3.B.1).

Experimental evidence for the predicted large quadrupole contribution is provided by a comparison of the relative shapes of the C 1*s* and O 1*s* $2\pi_u^*$ GOS profiles. Even the as-recorded data (Figs. 6.1, 6.3) shows that the decrease in signal to large momentum transfer is much gentler in the O 1*s* than the C 1*s* spectrum, suggesting there may be additional contributions at larger momentum transfer for O 1*s* excitation.

Figure 6.11 presents the ratio of the GOS for the O $1s \rightarrow 2\pi^*$ to that for the C $1s \rightarrow 2\pi^*$ transition for both experiment and theory. As K^2 increases, the ratio increases, indicating the O $1s \rightarrow 2\pi^*$ transition becomes relatively stronger at larger K^2. For $K^2 = 0$ both the C 1*s* and the O 1*s* GOS have only the allowed $\sigma_g \rightarrow 2\pi_u^*$ component. As K^2 increases, the optically forbidden O 1*s* ($\sigma_u \rightarrow 2\pi_u^*$) component also contributes to the experimental GOS for the O $1s \rightarrow 2\pi_u^*$ band and, thus the ratio between the O 1*s* $\{(\sigma_g \rightarrow 2\pi_u^*) + (\sigma_u \rightarrow 2\pi_u^*)\}$ and the C 1*s* ($\sigma_g \rightarrow 2\pi_u^*$) GOS increases. The increase in the ratio between the O 1*s* and the C 1*s* GOS as a function of K^2 is a manifestation of the contribution of the optically forbidden O 1*s* ($1\sigma_u \rightarrow 2\pi_u^*$) process.

This is perhaps the most direct experimental evidence for the strong electric quadrupole O 1*s* excitations predicted by the calculations.

Figure 6.12 compares the experimentally derived GOS profile of the 538.8 eV band with the sum of the theoretical results for the O 1*s* ($1\sigma_g \rightarrow 3p\sigma_u$), O 1*s* ($1\sigma_u \rightarrow 3p\sigma_u$), O 1*s* ($1\sigma_g \rightarrow 3p\pi_u$), O 1*s* ($1\sigma_u \rightarrow 3p\pi_u$), O 1*s* ($1\sigma_g \rightarrow 4s\sigma_g$) and O 1*s* ($1\sigma_u \rightarrow 4s\sigma_g$) processes. The calculated contributions to the overall GOS at this energy come from six different excitation processes, 3 optically allowed and 3 optically forbidden. Calculations

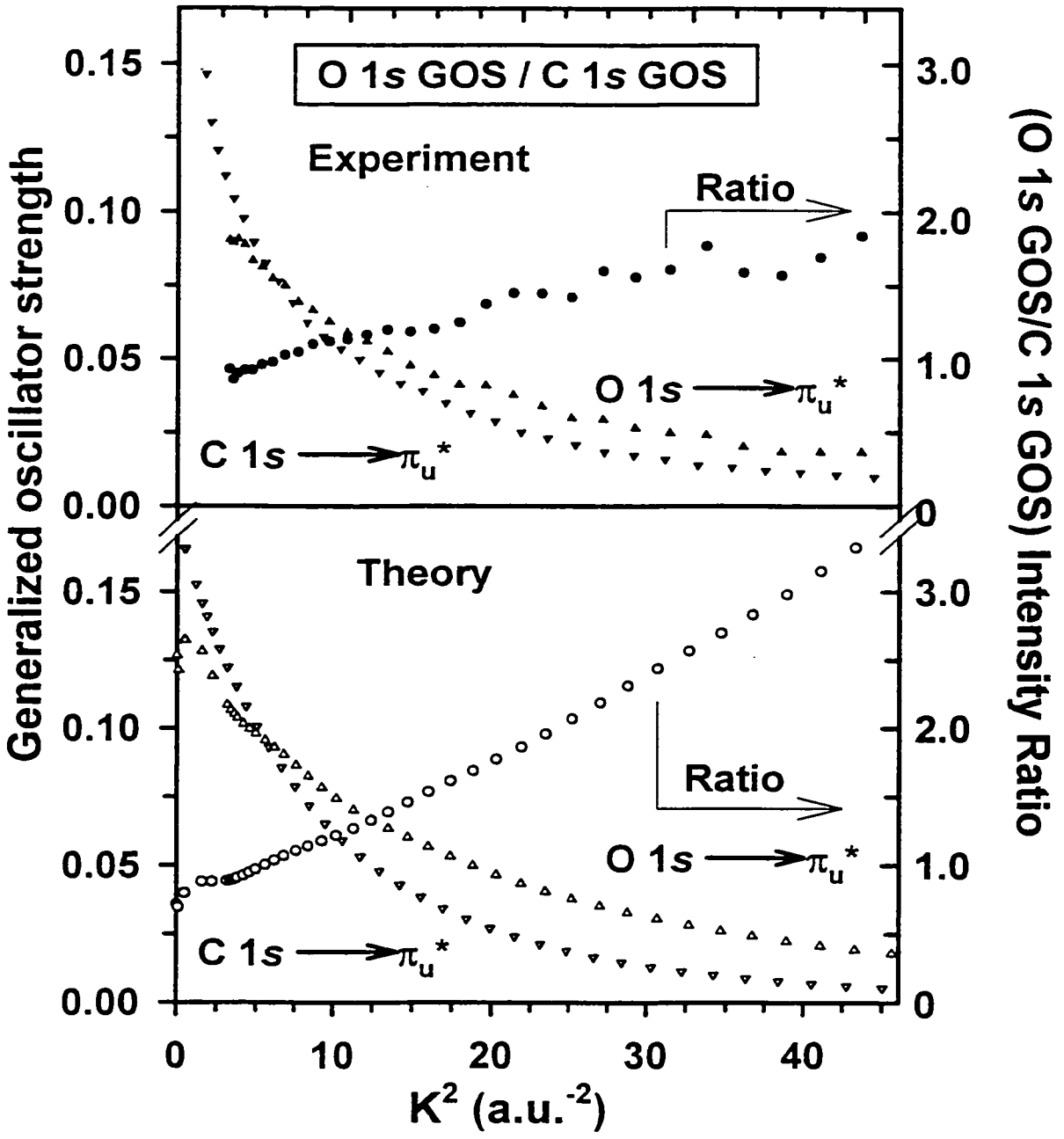

Fig. 6.11 Momentum transfer dependence of the GOS profiles of O $1s \rightarrow 2\pi^*_u$ and C $1s \rightarrow 2\pi^*_u$ transitions and their ratio (upper, experimental; lower, theoretical).

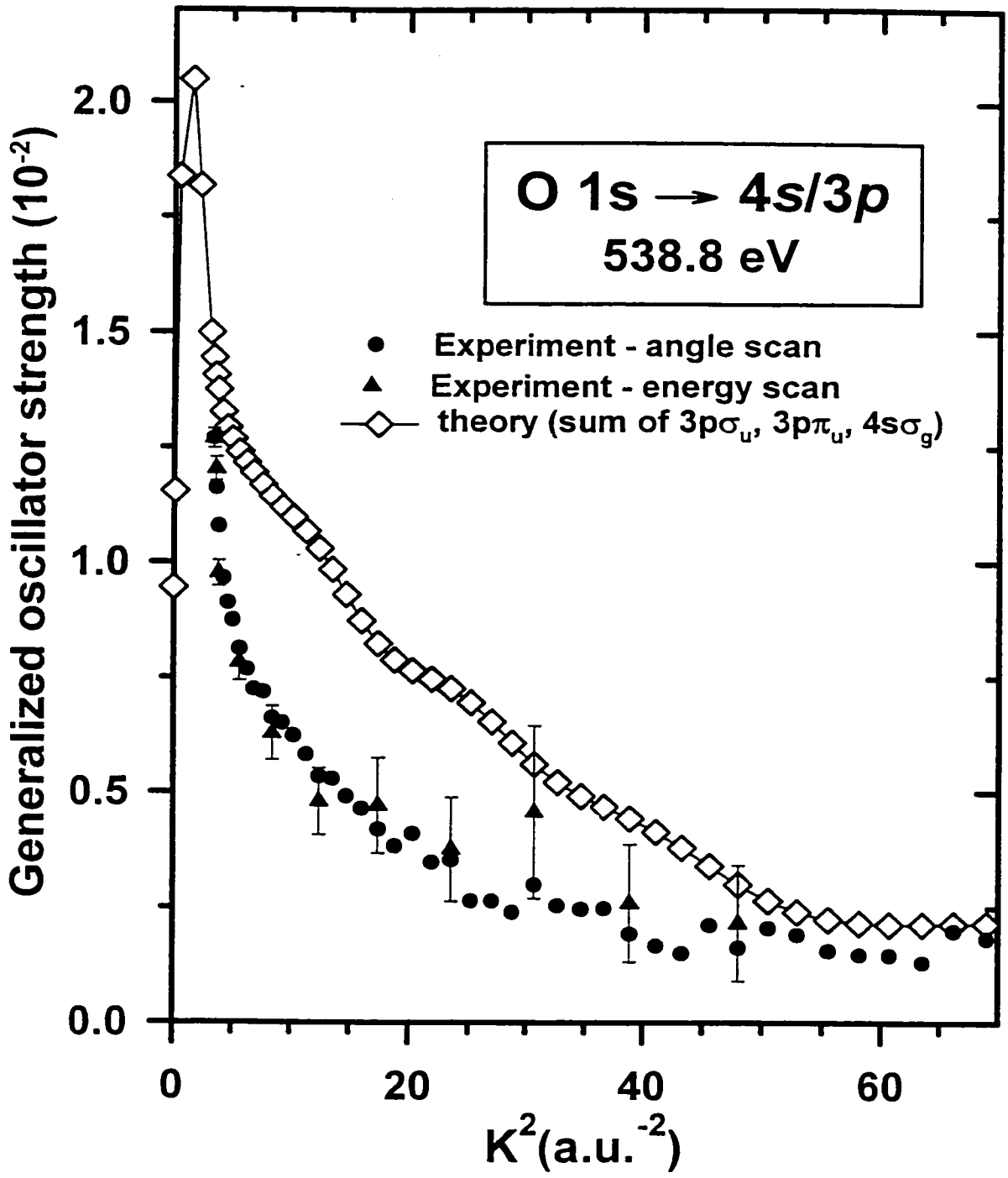

Fig. 6.12 Experimental GOS profile of the 538.8 eV band compared to the sum of the GOS calculated for the O 1*s* ($1\sigma_g \rightarrow 3p\sigma_u$), O 1*s* ($1\sigma_u \rightarrow 3p\sigma_u$), O 1*s* ($1\sigma_g \rightarrow 3p\pi_u$), O 1*s* ($1\sigma_u \rightarrow 3p\pi_u$), O 1*s* ($1\sigma_g \rightarrow 4s\sigma_g$) and O 1*s* ($1\sigma_u \rightarrow 4s\sigma_g$) transitions.

(Figure 6.9) show that the optically forbidden $3p\pi_u$ and $4s\sigma_g$ excitations contribute significantly at non-zero momentum transfer, and suggest that all 3 final states ($3p\sigma_u$, $3p\pi_u$ and $4s\sigma_g$) are present in the unresolved signal.

Figure 6.13 shows the experimental GOS profiles for the O 1*s* ($1\sigma_u \rightarrow$ Rydberg resonance) at 540.3 eV, the O 1*s* ($1\sigma_u \rightarrow 5\sigma_g^*$) resonance at 541.6 eV, the O 1*s* double excitation at 553.2 eV, the O 1*s* ($1\sigma_g \rightarrow 4\sigma_u$) resonance at 559 eV, and the O 1*s* continuum GOS integrated between 576 eV and 580 eV. All five of these features have similar GOS shapes. In fact, the GOS for all O 1*s* excitation and ionization channels decrease continuously with increasing momentum transfer, with a similar shape in each case. Where fit, the Lassettre parameters for the GOS for O 1s excitation are summarized in table 6.3.

6.3. Summary

Absolute GOS profiles up to $K^2 = 70$ a.u.$^{-2}$ have been derived experimentally for all resolved C 1*s* and O 1*s* excitation and ionization features, while absolute GOS profiles have been computed for all discrete core excitations of CO_2. These results greatly extend previously available GOS data for CO_2. In the C 1*s* regime there is generally good agreement between experiment and theory, aside from a discrepancy of the GOS for the C $1s \rightarrow 3s\sigma_g$ which has a vibronic contribution not considered in these calculations. In the O 1*s* regime there is also reasonable agreement between experiment and theory for the shape of the GOS for the O $1s \rightarrow 2\pi^*$ transition, but the absolute magnitude is somewhat uncertain, as discussed above. Comparison of experimental and theoretical

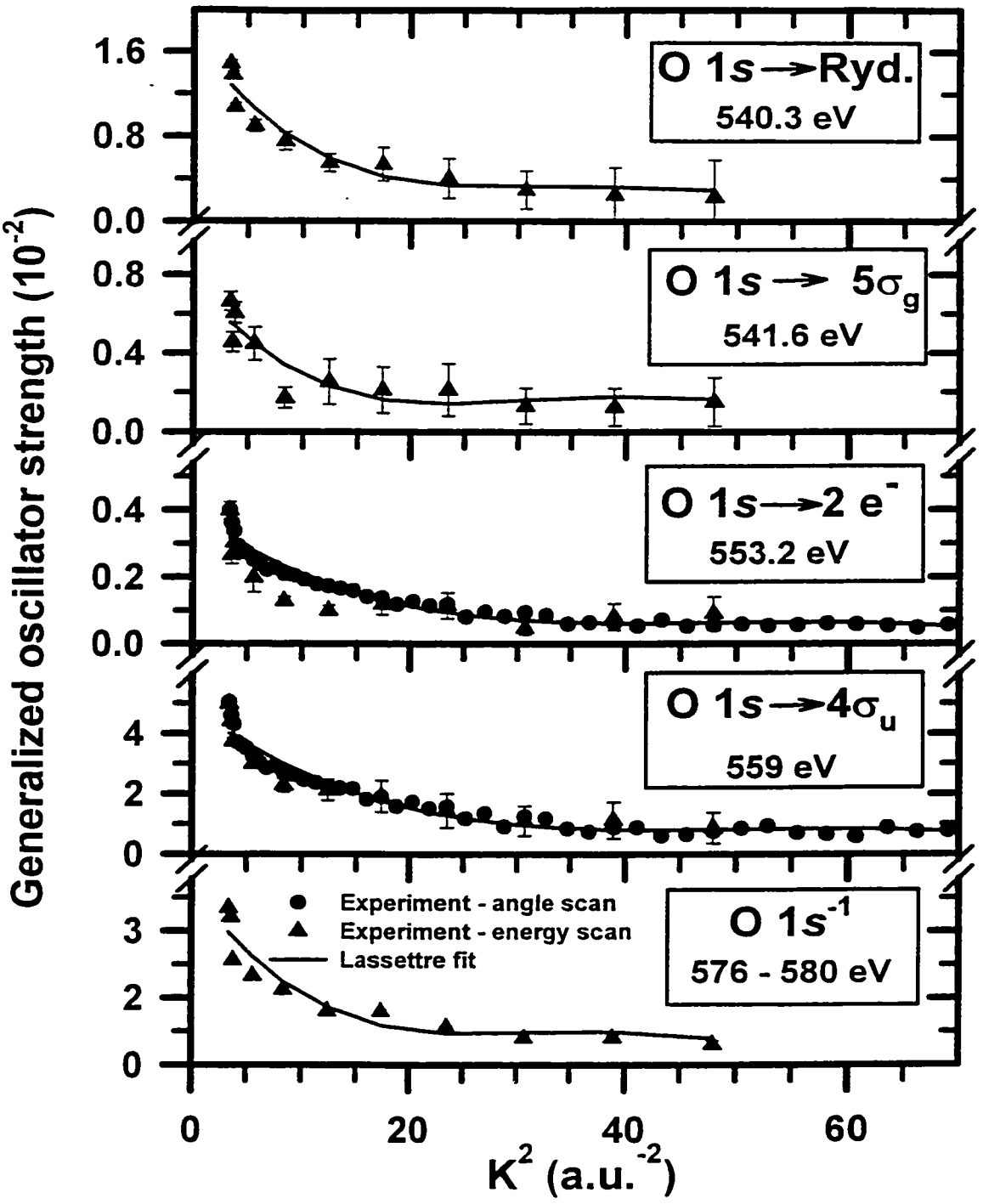

Fig. 6.13 Experimental GOS profiles for O 1*s* ($1\sigma_{g,u} \rightarrow$ Rydberg) (540.3 eV), O 1*s* ($1\sigma_{g,u} \rightarrow 5\sigma^*_g$) (541.6 eV), O 1*s* double excitation (553.2 eV) transitions, the O 1*s* ($1\sigma_{g,u} \rightarrow 4\sigma^*_u$) shape resonance (559 eV) and the O 1s continuum integrated between 576 and 580 eV.

GOS results over an extended range of transferred momentum has suggested that the first Born approximation may hold to much larger K^2 values for inner-shell than for valence shell excitation. For the first time, we have observed the C 1*s* ($2\sigma_g \rightarrow 5\sigma_g^*$) $^1\Sigma_g^+$ resonance at 298 eV.

Chapter 7

EXPERIMENTAL STUDY OF GENERALIZED OSCILLATOR STRENGTHS FOR C 1*s*, S 2*p* AND O 1*s* IN CS_2 AND COS

The generalized oscillator strength (GOS) profiles in the momentum transfer range (K) of (2 a.u.$^{-2}$ < K^2 < 40 a.u.$^{-2}$) for all resolved S 2p, C 1s, and O 1s transitions of carbon disulfide (CS_2) and carbonyl sulfide (COS) are presented for the first time. For CS_2, inner-shell triplet states have also been observed by measuring near threshold C 1s energy loss spectra using a wide range of angles (4 °– 20 °) and impact energies (130 – 1300 eV).

7.1. Introduction

The molecules CO_2, COS and CS_2 are closely related triatomic linear molecules. A detailed experimental and theoretical study of generalized oscillator strengths for C 1*s* and O 1*s* excitation in CO_2 has been presented in the previous chapter. This chapter presents the complementary results for the CS_2 and COS molecules. In addition to observations of quadrupole transitions, singlet-triplet transitions have been also observed in CS_2 and used to aid spectral assignment.

The literature on the core excitation spectra of CS_2 [H87, PL84, NHD&88, WB74] and COS [HK87, PL84, NHD&88, WB74, YK87, SYK&89] contain inconsistencies in both spectral shapes and interpretation. In particular the positions of the core $\rightarrow \sigma^*$ excitations are not well established. One goal of this study is to provide a consistent spectral interpretation of the core excitation spectra. The momentum transfer dependence, comparison of the core excitation spectra at all edges and comparison with *ab initio* calculations are used to help identify the locations of core $\rightarrow \sigma^*$ transitions. A previous study on CO_2 [ETH&99] was able to find the dipole forbidden, quadrupole allowed C 1s $\rightarrow 5\sigma_g^*$ by means of the GOS determination. A similar situation may exist in CS_2 which is valence isoelectronic and iso-symmetric to CO_2. The GOS profiles were used to characterize the π^*, $\sigma^*_{C\text{-}S}$ and $\sigma^*_{C\text{-}O}$ states of the three closely related molecules, CO_2, CS_2 and COS.

7.2. Results and Discussion: Spectroscopy

7.2.1. Carbon Disulfide (CS_2)

Carbon disulfide, a linear, 16 valence electron system isoelectronic with CO_2, N_2O and COS, is a molecule of astrophysical and astronomical interest [H71a]. Its ground state electronic configuration is:

$$S_{1s}^{4}\, C_{1s}^{2}\, S_{2s}^{4}\, S_{2p}^{12}\, (5\sigma_g)^2\, (4\sigma_u)^2\, 6\sigma_g^2\, 5\sigma_u^2\, 2\pi_u^4\, 2\pi_g^4, \quad X\ {}^1\Sigma_g^+$$

Within a minimal basis set, an LCAO-MO description predicts the existence of four vacant molecular orbitals, two of which are degenerate with π_u symmetry, while the other

two have σ_g and σ_u symmetry. The lowest unoccupied molecular orbitals in CS_2 are thus expected to be $3\pi_u$, $7\sigma_g$ and $6\sigma_u$, analogous to the $3\pi_u$, $5\sigma_g$ and $5\sigma_u$ of CO_2 [ETH&99].

7.2.1.1. Carbon 1*s* Excitation

Figure 7.1 presents C 1*s* spectra of CS_2 recorded under small (θ = 4°, K^2 = 1.5 a.u.$^{-2}$) and large (θ = 24°, K^2 = 20 a.u.$^{-2}$) momentum transfer conditions. The spectra were obtained with a final electron energy of 1300 eV. The general features are in agreement with the literature [HK87, WB74]. The spectra were calibrated using the energy of 286.1 eV for the (C 1*s* $\rightarrow$ $3\pi_u$*) $^1\Pi_u$ state reported by Wight and Brion [WB74]. **Table 7.1** summarizes the energies of the C 1*s* spectral features derived from the constrained multiple file curve-fit analysis.

At both angles, the spectrum is dominated by the intense feature at 286.1 eV (peak 2). However there is a dramatic fall-off in intensity as the scattering angle increases - the as-recorded 24° spectrum is about 100-fold weaker than that at 4°. This is partly due to the rapid decrease of the excitation cross section with increasing angle, but it also reflects reduced overlap of the incident electron beam and analyzer acceptance cone [EFT&99]. The dominant peak is the $X^1\Sigma_g^+ \rightarrow {}^1\Pi_u$ (C 1*s* $2\sigma_g^{-1}$, $3\pi_u$*) transition, analogous to the first discrete peak in the C 1*s* spectrum of CO_2 [ETH&99].

Figure 7.2 shows an expanded presentation of the discrete region of C 1*s* spectra of CS_2 acquired with final energies of 1300eV and 130eV above threshold at 4°, 130 eV

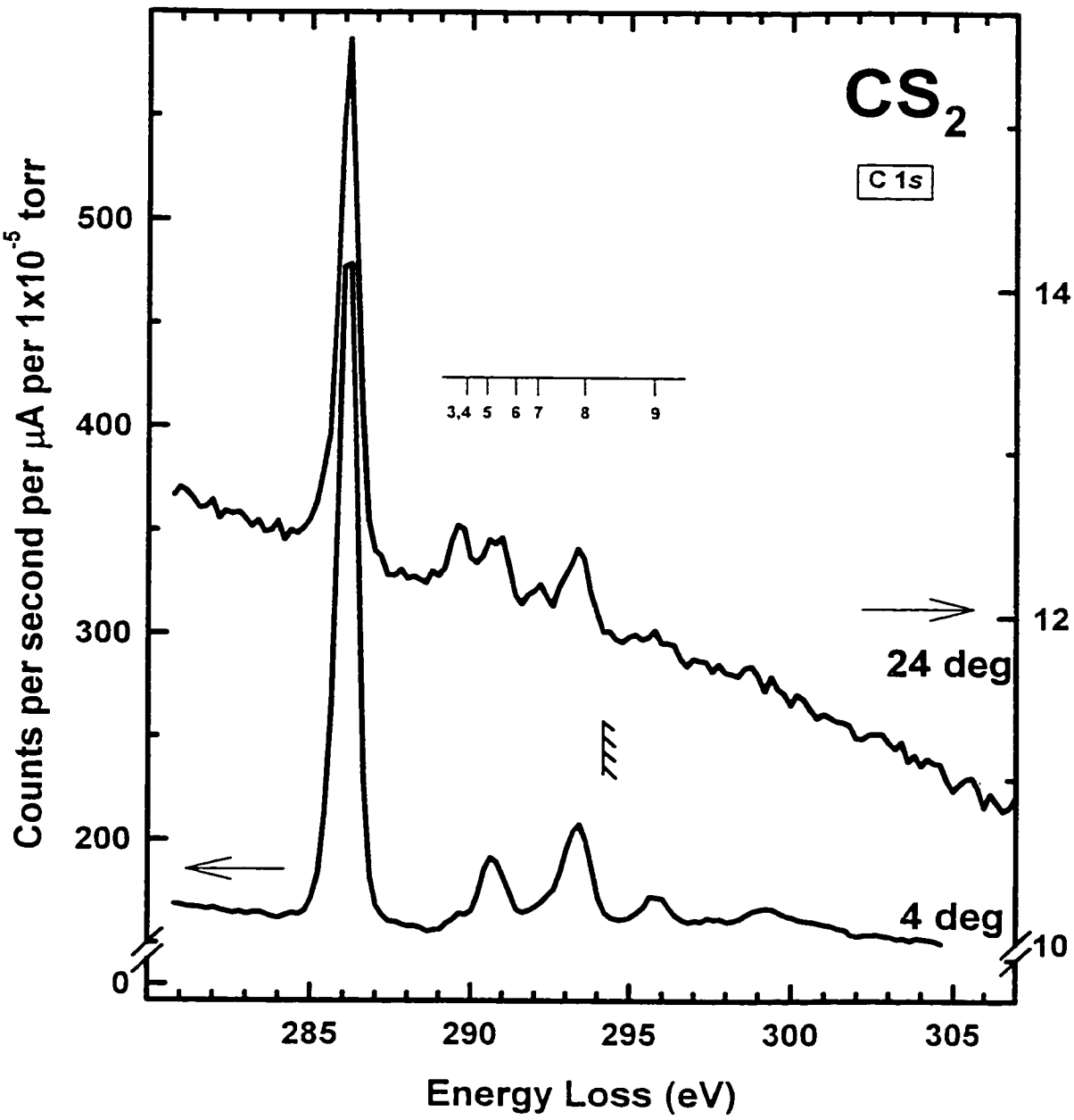

Fig. 7.1 Comparison of the C 1*s* energy loss spectra of CS_2 recorded at a final energy of 1300 eV at 4° (K^2 = 1.5 a.u.$^{-2}$) and 24° (K^2 = 20 a.u.$^{-2}$). The hatched line indicates the C 1*s* IP.

Table 7.1 Energies, line shapes, widths and assignments of features of the C 1*s* spectra of CS_2.

Peak	Energy (eV)		Term Value	Line type[b]	Width	Assignment
	This work	Literature				
1	285.7	285.2[a]	7.9	G	0.85	$3\pi_u^*$ ($^3\Pi$)
2	286.1	286.1[c]	7.0	G	0.60	$3\pi_u^*$ ($^1\Pi$)
3	289.5	288.9[a]	4.2			
4	289.6	289.6[a]	3.5	G	0.63	$3s\sigma_g$
5	290.7	290.6[a]	2.5	G	1.16	$3p\pi_u$
6	292.1	292.4[a]	0.7	G	1.16	σ_g^* ($^1\Sigma_g$)
		293.1[d]		E	1.25	IP
7	293.3	293.4	-0.3	G	1.00	$6\sigma^*_u$
8	295.8	295.8	-2.7	G	0.88	[g]$2e^-$
		297.3				[g]$2e^-$
9	299.6	299.4[e]	-6.3	G	4.64	[g]$2e^-$

[a]Ref. [HK87]
[b]G = Gaussian profile, E = error function edge shape
[c]All energies were established by calibrating the C 1*s* → $3\pi_u^*$ transition to this value [WB74]
[d]Ref. [AGA&72]
[e]Ref. [WB74]
[f]Ref. [NHD&88]
[g]Ref. [KEH&98]

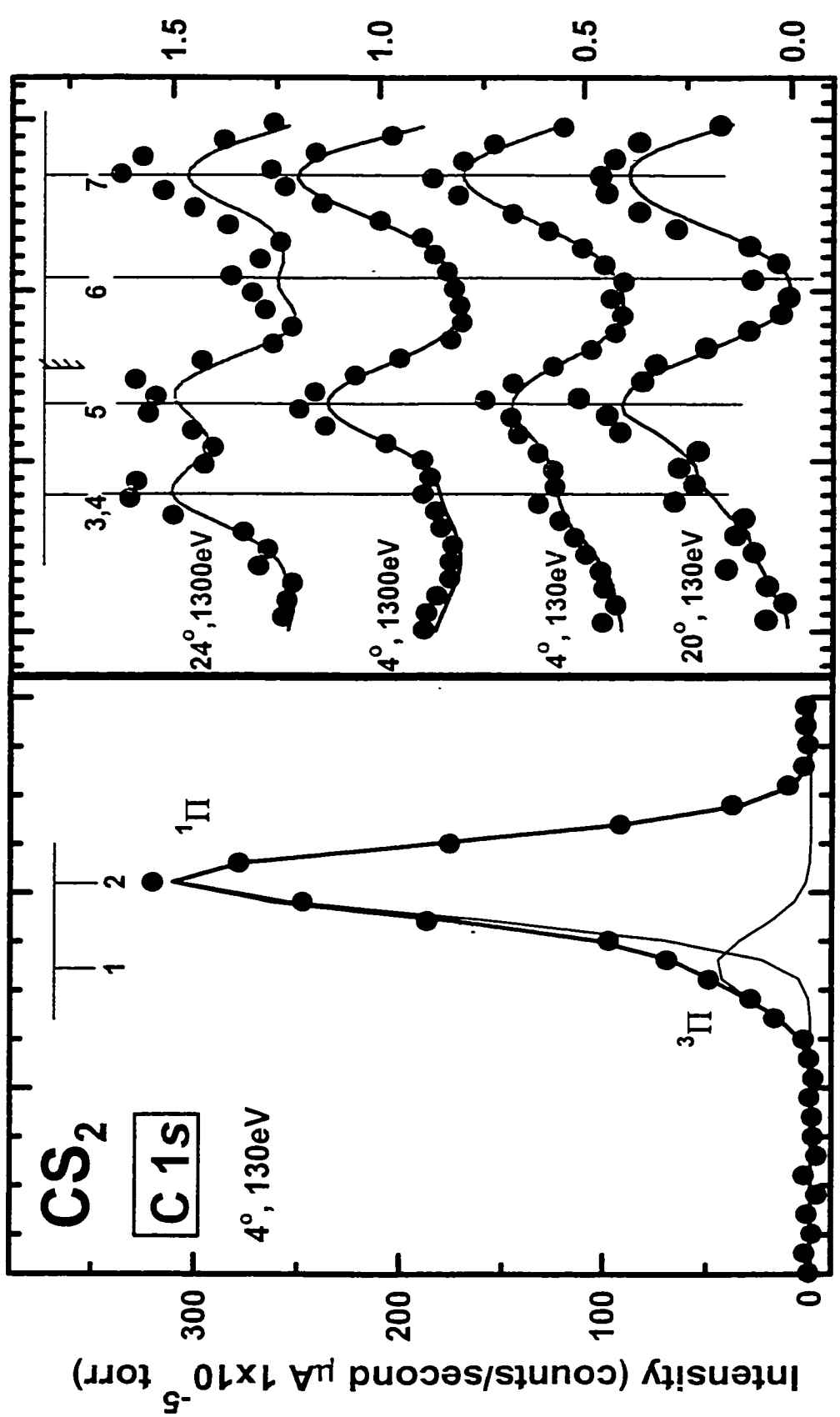

Fig. 7.2 (left) Electron Energy Loss spectra of CS_2 in the region of the (C $1s^{-1}$, π^*)$^3\Pi$ and $^1\Pi$ states recorded at scattering angle 4° and 130 eV final energy. (right) Detail of the 288-294 eV energy loss recorded under a variety of scattering angles and impact energy conditions.

above threshold at 20° and 1300 eV above threshold at 24°. These values were chosen to enhance selectively specific classes of transitions. Thus, the (130 eV, 20°) conditions highlights triplet states associated with both dipole and quadrupole allowed transitions to valence-like final states. At (130 eV, 4°), just the triplet states associated with dipole allowed transitions are expected. Indeed, on the low energy side of the peak 2, there is another peak (peak 1) at an energy of 285.2 eV, previously reported and assigned to the triplet state associated with the C $1s \rightarrow (3\pi_u^*)\ ^3\Pi_u$ configuration by Harrison and King [HK87]. At (1300 eV, 4°) the spectrum should be dominated by the electric dipole transitions alone. Finally, at (1300 eV, 24°) the experimental conditions are favorable for non-dipole transitions to appear.

As noted, the spectroscopic challenge is the identification of the C $1s \rightarrow \sigma^*$ transitions. In the initial analysis, Wight and Brion [WB74] did not propose any σ^* assignments, but rather attributed the non-π^* features to Rydberg states or left them unassigned. Nenner *et al.* [NHD&88] proposed assignment of the dipole forbidden C $1s \rightarrow 7\sigma_g^*$ transition to a very weak feature observed by Wight and Brion at 289.6 eV [WB74]. This feature corresponds to that labeled (3,4) in the present work. On examining the large impact energy spectra, the features at 289.6 eV (features 3,4) and 292.1 (feature 6) increase in relative intensity at large scattering angles, a typical signature of a non-dipole transition. There are two candidate states that one might consider for these features, one the C $1s \rightarrow 7\sigma_g^*$ transition, the other the C $1s \rightarrow 3s\sigma_g^*$ transition. The 292.1 eV is too high in energy to be the $3s\sigma_g$ state. Thus the 289.6 eV

peak could be the $3s\sigma_g$ Rydberg state and the 292.1 eV peak, the ($C1s$, $7\sigma_g^*$) state. Considerable intensity is also observed in the near threshold spectra, (130 eV, 4°) and (130 eV, 20°). The center of the (3,4) peak in the lower impact energy spectra seems to be slightly lower than in the higher impact spectra. Thus, there could be also a contribution from a $^3\Sigma$ ($C1s$, $3s\sigma_g^*$) state. If so, the singlet-triplet splitting is small, indicative of a low degree of C $1s \rightarrow 3s\sigma^*$ overlap, as expected for a Rydberg transition.

Either one of the prominent features at 290.7 eV (peak 5) and 293.3 eV (peak 7) could be candidates for the dipole allowed C $1s \rightarrow 5\sigma^*$ transition. The 290.7 eV peak is at the expected position for the dipole allowed $3p\pi_u$ Rydberg transition, which are frequently quite intense. Thus we attribute the 290.7 eV to the ($C1s^{-1}$, $3p\pi_u$) Rydberg state and the 293.3 eV peak to the (C $1s^{-1}$, $5\sigma_u^*$) state. One must also consider the possibility of Rydberg valence mixing [SBT&88, HHS86, DTH90].

The features at 295.8 eV (peak 8) and 299.6 eV (peak 9) in Fig. 7.1 are assigned to multi-electron excitations. More specifically, these two resonances, together with another one at ~297.3 eV [KEH&98] that could not be resolved, are formed by transitions to the π^* state associated with the shake-up of the outer valence electrons ($2\pi_g$, $2\pi_u$, $5\sigma_u$ and $6\sigma_g$) to closely lying antibonding levels ($3\pi_g$, $3\pi_u$, $6\sigma_u$ and $7\sigma_g$).

7.2.1.2. Sulfur 2*p* Excitation

Figure 7.3 presents the S $2p$ energy loss spectra of carbon disulfide recorded under dipole ($\theta = 4°$, $K^2 = 0.85$ a.u.$^{-2}$) and non-dipole ($\theta = 20°$, $K^2 = 13$ a.u.$^{-2}$) conditions.

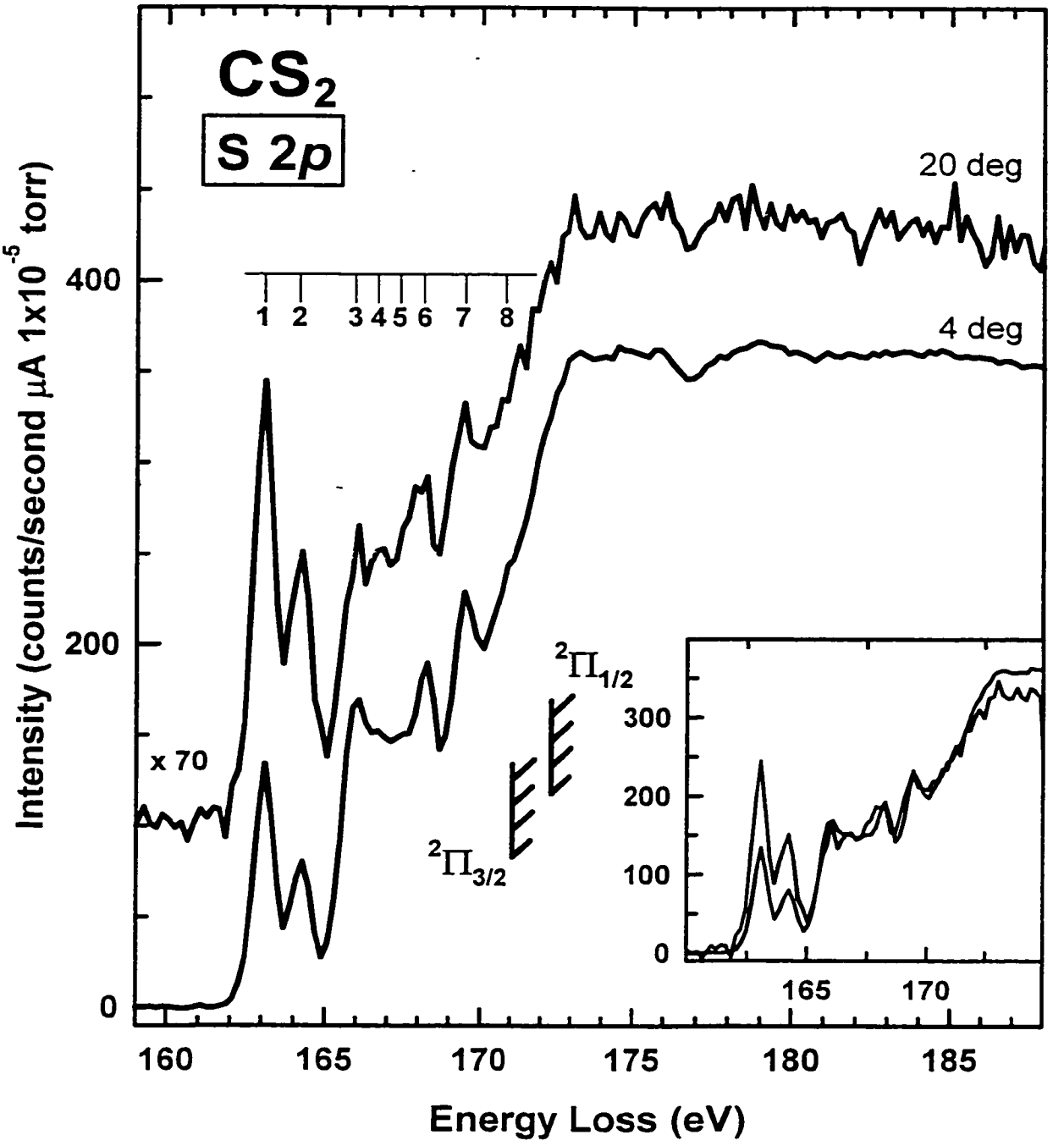

Fig. 7.3 Comparison of S 2*p* energy loss spectra of CS_2 recorded with final energy of 1300 eV at 4° (K^2 = 0.85a.u.$^{-2}$) and 20° (K^2 = 13 a.u.$^{-2}$). The hatched line lines indicate the S 2*p* IP.

The spectra have been normalized to the beam current, pressure and time, and background subtracted, but they have not been subjected to the geometric or kinematic corrections. **Table 7.2** summarizes the energies of the S 2*p* spectral features derived from the constrained multiple file curve-fit analysis.

The lowest energy discrete peaks observed at 163.1 eV (peak 1) and 164.2 eV (peak 2) in the S 2*p* spectrum are associated with promotion of the sulfur 2*p* electrons to the vacant $3\pi_u^*$ valence molecular orbital. The energy separation between them (~ 1.1 eV) corresponds to that of the S 2*p* spin-orbit splitting (~1.2 eV). The intensity of these two features increases at higher scattering angle, suggesting there may be a mix of states, including one or more of non-dipole character, and not a single dipole allowed transition. Because CS_2 belongs to the $D_{\infty h}$ point group and the S 2*p* orbitals are of symmetry π_u, π_g and σ_g, there could be a strong non-dipole contribution from $\pi_u \rightarrow 3\pi_u$ transitions that increases the intensity of these peaks over that of the dipole allowed $\pi_g \rightarrow 3\pi_u$ and $\sigma_g \rightarrow 3\pi_u$ transitions.

The energy feature located at 165.9 eV (peak 3) is assigned to the $2p_{3/2} \rightarrow 7\sigma_g^*$ transition. The S $2p_{1/2} \rightarrow \sigma_g^*$ transition should then appear around 167 eV, as suggested by Karawajczyk *et al.* [KEH&98], assuming similar separation of the $\pi^*_{1/2}$ and $\sigma^*_{1/2}$, and the $\pi^*_{3/2}$ and $\sigma^*_{3/2}$ states.

The line at 166.6 eV (peak 4) is assigned to the $4s\sigma_g$ Rydberg state, while the feature at 167.5 eV (peak 5) is associated with transitions into lower Rydberg orbitals of *p* symmetry, split into π_u and σ_u, components that cannot be resolved.

Table 7.2 Energies, line shapes, widths and assignments of features of the S 2*p* spectra of CS_2.

Peak	Energy (eV)		Term Value				Assignment	
	This work	Literature	$T_{3/2}$	$T_{1/2}$	Line type[b]	Width	$2p_{3/2}$	$2p_{1/2}$
1	163.1	163.1[c]	6.7		G	0.78	$3\pi_u^{*e}$	
2	164.2	164.2[a]		6.8	G	0.78		$3\pi_u^{*e}$
3	165.9	165.9[a]	3.9		G	1.04	$7\sigma_g^{*e}$	
4	166.6	166.5[a]		3.3	G	0.90	$4s\sigma_g^{e}$	
		167.0[e]						$7\sigma_g^{*e}$
5	167.5	167.4[a]	2.4		G	1.08	$4p\pi_u^{e}$ /$4p\sigma_u^{e}$	
		167.6[e]						$4s\sigma_g^{e}$
		167.8[e]					$3d\sigma_g^{e}$	
6	168.3	168.2[a]	1.6		G	0.61	$3d\pi_g^{e}$ /$3d\delta_g^{f}$ /$5s\sigma_g^{e}$ /$5p\pi_u^{e}$ /$3d\delta_g^{e}$	
		168.5[e]					$5p\sigma_u^{e}$	$4p\pi_u^{e}$
		168.7[e]						$4p\sigma_u^{e}$
		169.0[e]						$3d\sigma_g^{e}$
		169.1[e]						$3d\pi_g^{e}$
7	169.5	169.5[a]		1.5	G	1.64		$5s\sigma_g^{e}$ /$3d\delta_g^{e}$ /$5p\sigma_u^{e}$
		169.8[d]			E	1.25	$IP_{3/2}$	
		169.9[e]						$4d\pi_g^{e}$
8	170.8	170.8[a]		0.2	G	0.53		$4d\delta_g^{f}$
		171.0[d]			E	1.25		$IP_{1/2}$
		177.1[a]	-7.3	-6.1				$\sigma^*_u{}^{g}$

[a]Ref. [WB74]
[b]G = Gaussian profile, E = error function edge shape
[c]All energies were established by calibrating the S $2p_{3/2} \rightarrow 3\pi_u^*$ transition to this value [WB74]
[d]Ref. [AGA&72]
[e]Ref. [KEH&98]
[f]Ref. [KGM77]
[g]Ref. [NHD&88]

The structure at 168.3 eV (peak 6) corresponds to 3*d*-Rydberg states from S $2p_{3/2}$, split into components $3d\sigma_g$, $3d\pi_g$ and $3d\delta_g$, which again, the spectrometer cannot resolve, and a series of 5*s*- and 5*p*- Rydberg states [KEH&98].

The feature that is observed at 169.5 eV (peak 7) is assigned by Karawajczyk *et al.* [KEH&98] to a series of Rydberg transitions (3*d*-, 5*s*- and 5*p*-) from S $2s_{1/2}$, while the 4*d*-Rydberg transition from S $2s_{1/2}$ is located at 170.8 eV (peak 8).

The location of the σ_u^* is perhaps further away in the continuum, around 177.1 eV [NHD&88].

7.2.2. Carbonyl Sulfide (COS)

The ground state electronic configuration of COS is:

$$S_{1s}^2\, O_{1s}^2 C_{1s}^2\, S_{2s}^2\, S_{2p}^6\, (6\sigma)^2\, (7\sigma)^2\, (8\sigma)^2\, (9\sigma)^2\, (2\pi)^4\, (3\pi)^4, \quad {}^1\Sigma^+$$

7.2.2.1. Carbon 1*s* Excitation

Figure 7.4 presents the C 1*s* spectra recorded under small ($\theta = 4°$, $K^2 = 1.5$ a.u.$^{-2}$) and large ($\theta = 28°$, $K^2 = 26$ a.u.$^{-2}$) momentum transfer conditions. The spectra were obtained with a final energy of 1300 eV above threshold. The general features are in agreement with the literature [HK87, WB74, TKR79]. **Table 7.3** summarizes the energies and tentative assignments of the C 1*s* spectral features.

The intense peak observed at 288.2 eV (peak 2) is the C $1s \rightarrow \pi^*$ transition and the peak due to this transition dominates the spectrum, similar to the C 1*s* spectra of CO_2

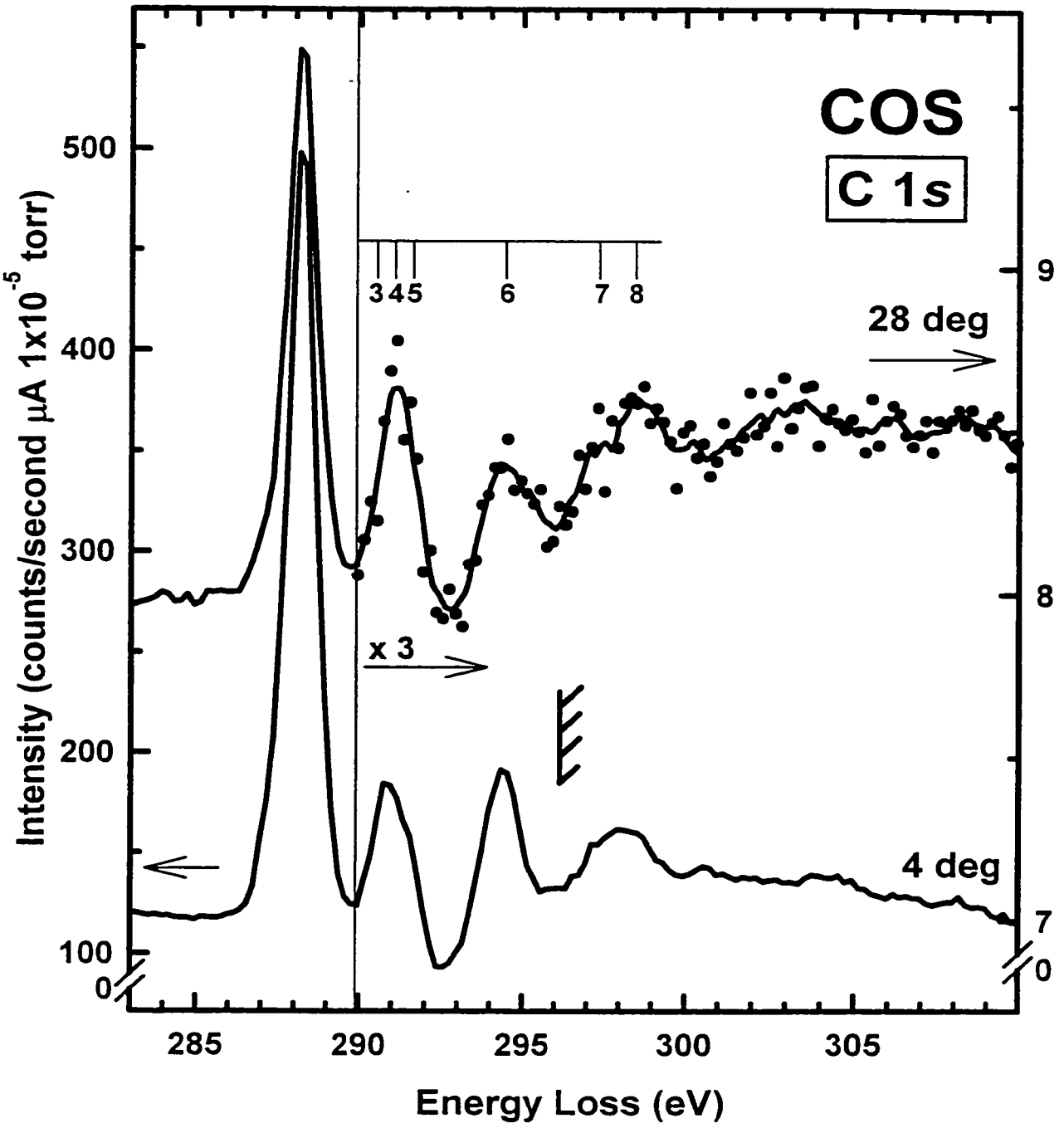

Fig 7.4 C 1*s* energy loss spectra of COS recorded using a final electron energy of 1300 eV at 4° (K^2 = 1.6 a.u.$^{-2}$) and 28° (K^2 = 26 a.u.$^{-2}$).

Table 7.3 Energies, line shapes, widths and assignments of features of the C 1*s* spectra of COS.

Peak	Energy (eV)		Term Value	Line type[b]	Width	Assignment
	This work	Literature				
1	287.1	287.1[a]	8.1	G	0.68	$4\pi^*$ ($^3\Pi$)
2	288.2	288.2[c]	7.0	G	1.06	$4\pi^*$ ($^1\Pi$)
3	290.7	290.7[a]	4.5	G	0.80	$10\sigma^*$ ($^3\Sigma$)
4	291.0	291.0[a]	4.2	G	1.82	3*p*
5	291.5	291.5[a]	3.7	G	0.72	$10\sigma^*$ ($^1\Sigma$)
		293.9[a]	1.3	G	1.16	R
6	294.4	294.4[d]	0.8	G	1.25	$10\sigma^*$+R
		295.2[e]		E	1.25	IP
7	297.5	297.5[d]	-2.3	G	0.92	$2e^-$
8	298.3	298.3[d]	-3.1	G	1.37	$2e^-$
9	305.1	304.6[f]	-9.4			2e
		~309[f]	-14			2e
		~314[f]	-19			$11\sigma^*$

[a]Ref. [HK87]
[b]G = Gaussian profile, A = arctangent edge shape
[c]All energies were established by calibrating the C 1*s* → $4\pi^*$ transition to this value [WB74]
[d]Ref. [WB74]
[e]Ref. [AGA&72]
[f]Ref. [MHB&89]

[ETH799] and CS_2 [HK87, WB74]. As with CO_2 and CS_2, the π^* term value is about 7 eV below the edge. Its triplet counterpart is observed at 287.1 eV (peak 1) [HK87].

With respect to the σ^* resonances, the lower symmetry of COS should allow both the $1\sigma^*$ and $2\sigma^*$ features to be detected in dipole allowed experimental conditions.

For the two relatively strong bands around 291.5 eV (peak 5) and 294.4 eV (peak 6), one possibility is that the two strong discrete features in COS are also Rydberg-valence mixed states, with the intensity derived from the $10\sigma^*$ orbital in COS. One might then expect a σ^* resonance of large σ^*(C-O) character to appear at higher energy, probably around 314 eV.

The peak at 291 eV (peak 4) is probably associated with $3p$ excitation, while the structures at 297.5 eV (peak 7) and 298.3 eV (peak 8) are assigned to multi-electron excitations.

7.2.2.2. Sulfur $2p$ Excitation

Figure 7.5 presents the S $2p$ energy-loss spectra of COS recorded under dipole ($\theta = 4°$, $K^2 = 0.86$ a.u.$^{-2}$) and non-dipole ($\theta = 24°$, $K^2 = 18$ a.u.$^{-2}$) conditions. The spectra plotted have been normalized to the beam current, pressure and time, and background subtracted, but they have not been subjected to the geometric or kinematic corrections. **Table 7.4** lists the energies and possible assignments of peaks.

As in the case of CS_2, the S $2p$ spectrum of COS exhibits a distinctive pattern of discrete transitions. The lowest energy discrete peak observed at 164.2 eV (peak 1) in the S $2p$ spectrum is associated to S $2p_{3/2} \rightarrow \pi^*$ transitions, analogous to the S $2p$ spectrum of

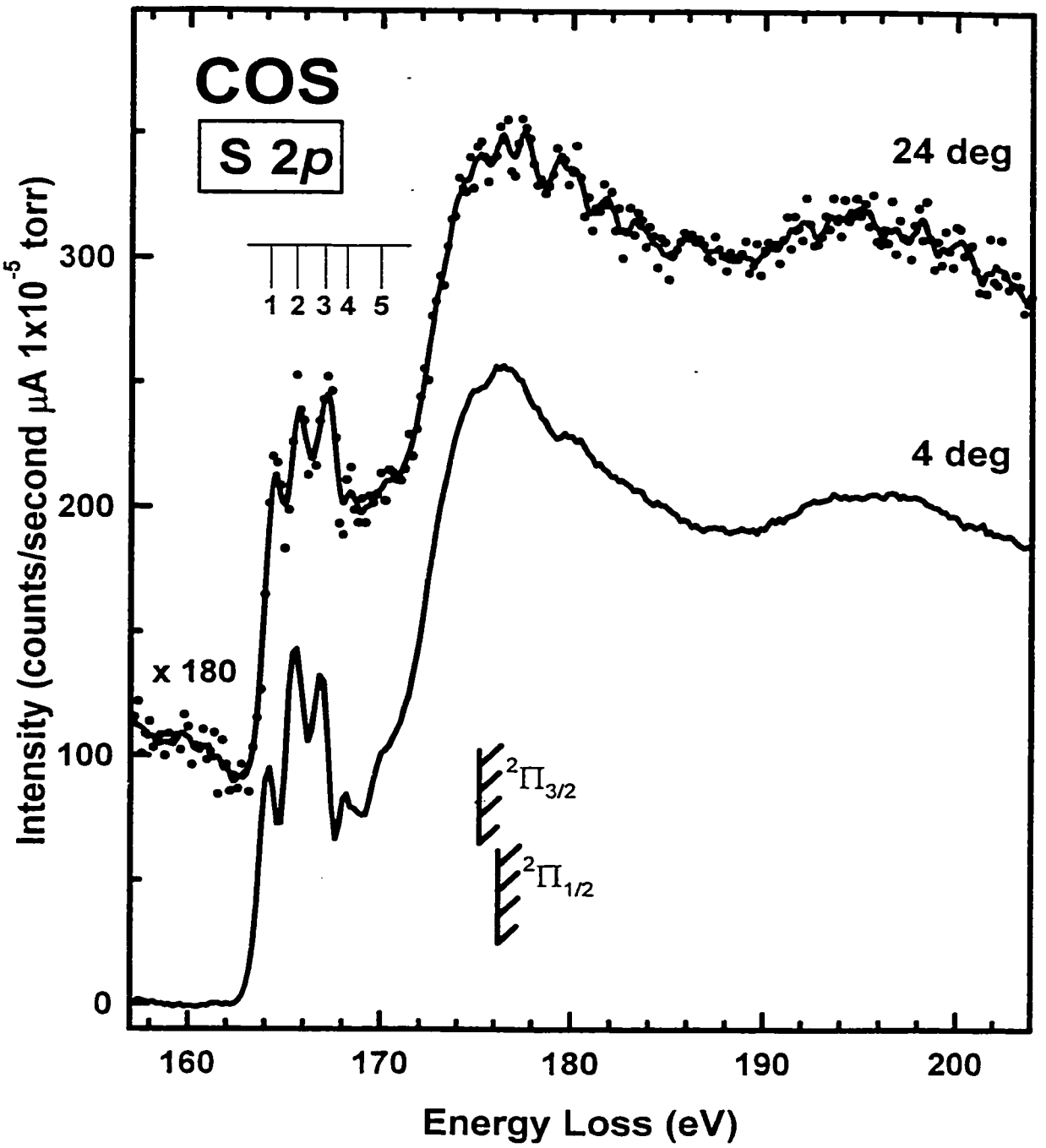

Fig 7.5 S 2*p* energy loss spectra of COS recorded using a final electron energy of 1300 eV at 4° (K^2 = 0.9 a.u.$^{-2}$) and 24° (K^2 = 18 a.u.$^{-2}$).

Table 7.4. Energies, line shapes, widths and assignments of features of the S 2*p* spectra of COS.

Peak	Energy (eV)		Term Value		Line type[b]	Width	Assignment	
	This work	Literature[a]	$T_{3/2}$	$T_{1/2}$			$2p_{3/2}$	$2p_{1/2}$
1	164.2	164.2[c]	6.4		G	1.01	$4\pi^{*c}$	
2	165.5	165.6		6.2	G	1.27		$4\pi^{*c}/10\sigma^*$
3	166.8	166.9	3.7		G	1.11	$4s/10\sigma^*$	
4	168.1	168.1	2.5	3.7	G	0.33	$4p^c$	$4s^c$
5	168.6	168.6	2.0		G	1.91	$3d^c$	
		168.9[c]					$5s^c$	
		169.3[c]					$5p^c$	$4p^c$
		169.5[c]					$4d^c$	
6	170.0	170.0		1.8	G	1.52		$3d,5s,5p^c$
		170.6[d]			E	1.25	$IP_{3/2}$	
		171.0		0.8				$4d$
		171.8[d]			E	1.25		$IP_{1/2}$
7	172.7				G	1.54		
8	176.1				G	5.13		
9	180.9				G	4.45	$2e^-$	
		191.0	-20.4	-19.2			$^f\sigma^*$	

[a]Ref. [WB74]
[b]G = Gaussian profile, E = error function edge shape
[c]All energies were established by calibrating the S $2p \rightarrow 4\pi^*$ transition to this value [WB74]
[d]Ref. [AGA&72]
[e]Ref. [KGM77]
[f]Ref. [NHD&88]

CS_2, while the peak observed at 165.5 eV (peak 2) would be associated with the promotion of S $2p_{1/2} \rightarrow \pi^*$ state. The distance between these first two peaks is ~1.3 eV which is close to the S $2p$ spin-orbit splitting [AGA&72]. The same distance is found between the second peak at 165.5 eV and the third peak at 166.8 eV [KGM77] as they may have contributions from the promotion of a S $2p$ electron to the $4\pi(\pi)^*$ and also to the $10\sigma^*$ orbitals.

The other higher energy discrete features located at 168.1 eV (peak 4), 168.6 eV (peak 5), and 170.0 eV (peak 6) are associated with Rydberg transitions, which converge to the S $2p$ ionization limit ($IP_{3/2}$ = 170.6 eV and $IP_{1/2}$ = 171.8 eV [AGA&72]).

The broad band around 178 eV is $3d$ (Σ) resonance while the sharper line at 180 eV (peak 9) is consistent with multi-electron excitation features. Transitions to the second σ^* orbital are probably located around 191 eV [NHD&88].

7.2.2.3. Oxygen 1*s* Excitation

Figure 7.6 shows examples of O 1*s* energy loss spectra of COS recorded under small and large momentum transfer conditions. The experimental and literature energies and assignments for the O 1*s* spectral features are presented in **Table 7.5**. The O 1*s* EELS spectrum acquired under dipole condition [WB74] and the photoabsorption spectrum [YK87] have been previously reported and analyzed.

At both small and large angle, the O 1*s* spectrum is dominated by the O $1s \rightarrow \pi^*$ transition at 533.7 eV (peak 1). Next there is a weak band at 535.9 eV (peak 2) which is attributed to a $3s$ Rydberg transition. The feature at 541 eV (peak 3) is attributed to the O

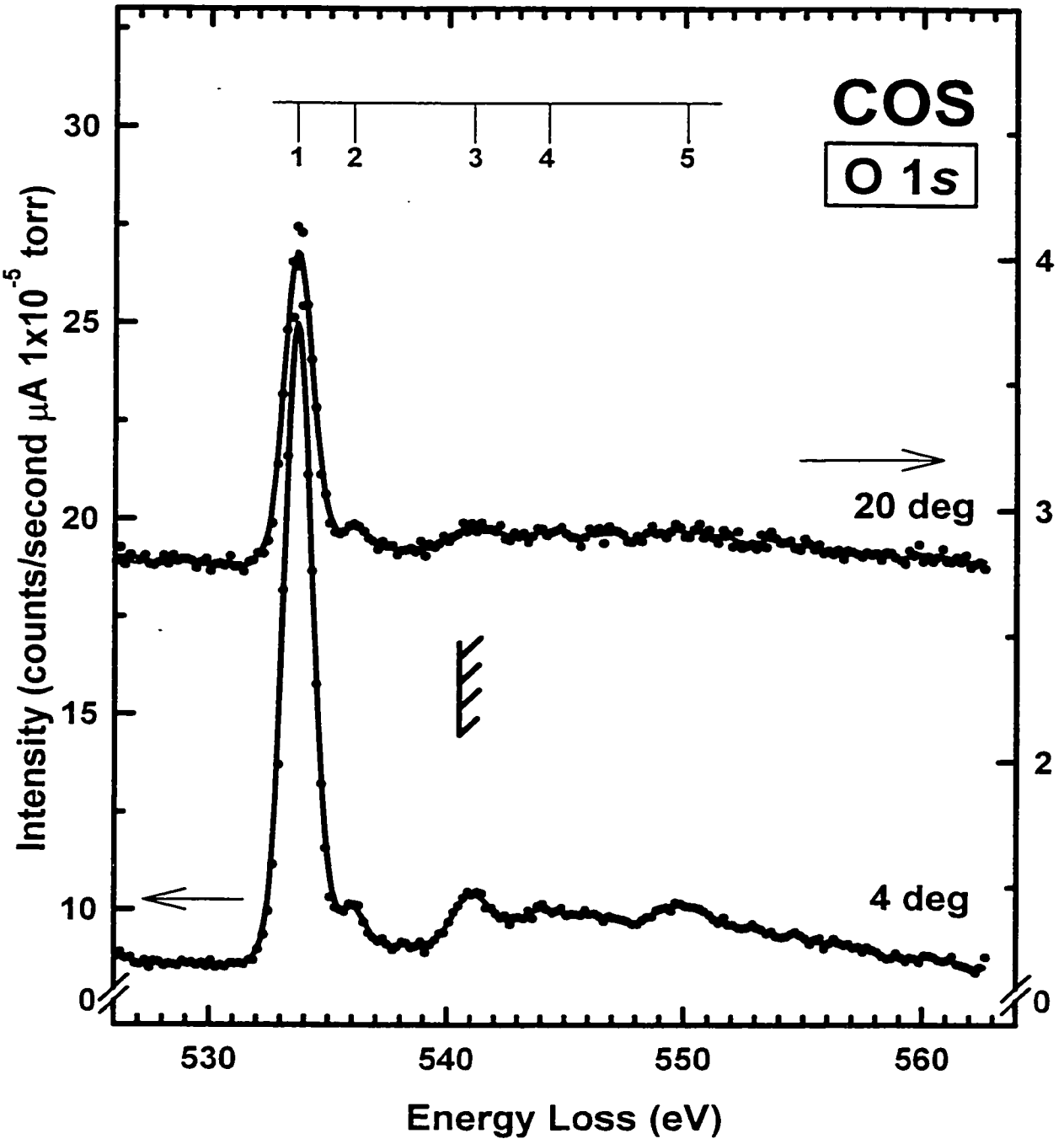

Fig 7.6 O 1*s* energy loss spectra of COS recorded using a final electron energy of 1300 eV at 4° (K^2 = 3.8 a.u.$^{-2}$) and 20° (K^2 = 17 a.u.$^{-2}$).

Table 7.5 Energies, line shapes, widths and assignments of features of the O 1*s* spectra of COS.

Peak	Energy (eV)		Term Value	Line type[b]	Width	Assignment
	This work	Literature[a]				
1	533.7	533.7[c]	6.6	G	1.37	$4\pi^*$
2	535.9		4.2	G	1.93	$3s\sigma$
3	541.0		0.2	G	1.93	$10\sigma^*$ (C-S)
		540.3[d]		E	1.50	IP
4	544.1		-4.8	G	1.93	$2e^-$
5	550.1		-10	G	1.93	$10\sigma^*$ (C-O)

[a]Ref. [HK87]
[b]G =Gaussian profile, E = error function edge shape
[c]All energies were established by calibrating the O 1*s* $\rightarrow$ $4\pi^*$ transition to this value [WB74]
[d]Ref. [AGA&72]

$1s \rightarrow 10\sigma^*$(C-S) transition, while the weak feature at 544.1eV (peak 4) could come from multi-electron excitation.

If the σ^* orbitals have a relatively localized character, one would expect the higher energy σ^*(C-O) resonance to be prominent at higher energy. This is consistent with the assignment of the O $1s \rightarrow 11\sigma^*$(C-O) transition to the band at 550 eV (peak 5).

7.3. Generalized Oscillator Strengths

7.3.1. Carbon Disulfide (CS_2)

7.3.1.1. C 1*s* GOS profiles

The GOS in the K^2 range from 1.5 a.u.$^{-2}$ to 35 a.u.$^{-2}$ for all resolved C 1*s* spectral features are presented in **Figure 7.7**. The relative GOS profiles were converted to absolute GOS profiles using the literature optical oscillator strength (OOS) for the strong C 1*s* ($2\sigma_g \rightarrow 3\pi_u^*$) $^1\Pi$ (taken as 0.11) [MHB&89]. The scaling factor for the π^* OOS was used to derive the absolute GOS from the relative GOS for all other features. There is good agreement between the results derived from **energy-scan** and **angle-scan** modes.

The GOS profile for the dipole-allowed C 1*s* ($2\sigma_g \rightarrow 3\pi_u^*$) transition decreases relatively smoothly from a maximum at $K^2 = 0$ as well as its triplet counterpart. In contrast, the GOS curve for the dipole-forbidden C 1*s* ($2\sigma_g \rightarrow 7\sigma_g^*$) transition increases with increasing momentum transfer, consistent with their assignment as the dipole-forbidden quadrupole allowed C 1*s* ($2\sigma_g \rightarrow 3s\sigma_g^*$) and C 1*s* ($2\sigma_g \rightarrow 7\sigma_g^*$) transitions.

The GOS profiles for the rest of the resolved transitions smoothly decrease as K^2 increases, consistent with their assignments as dipole allowed transitions. Note that if the

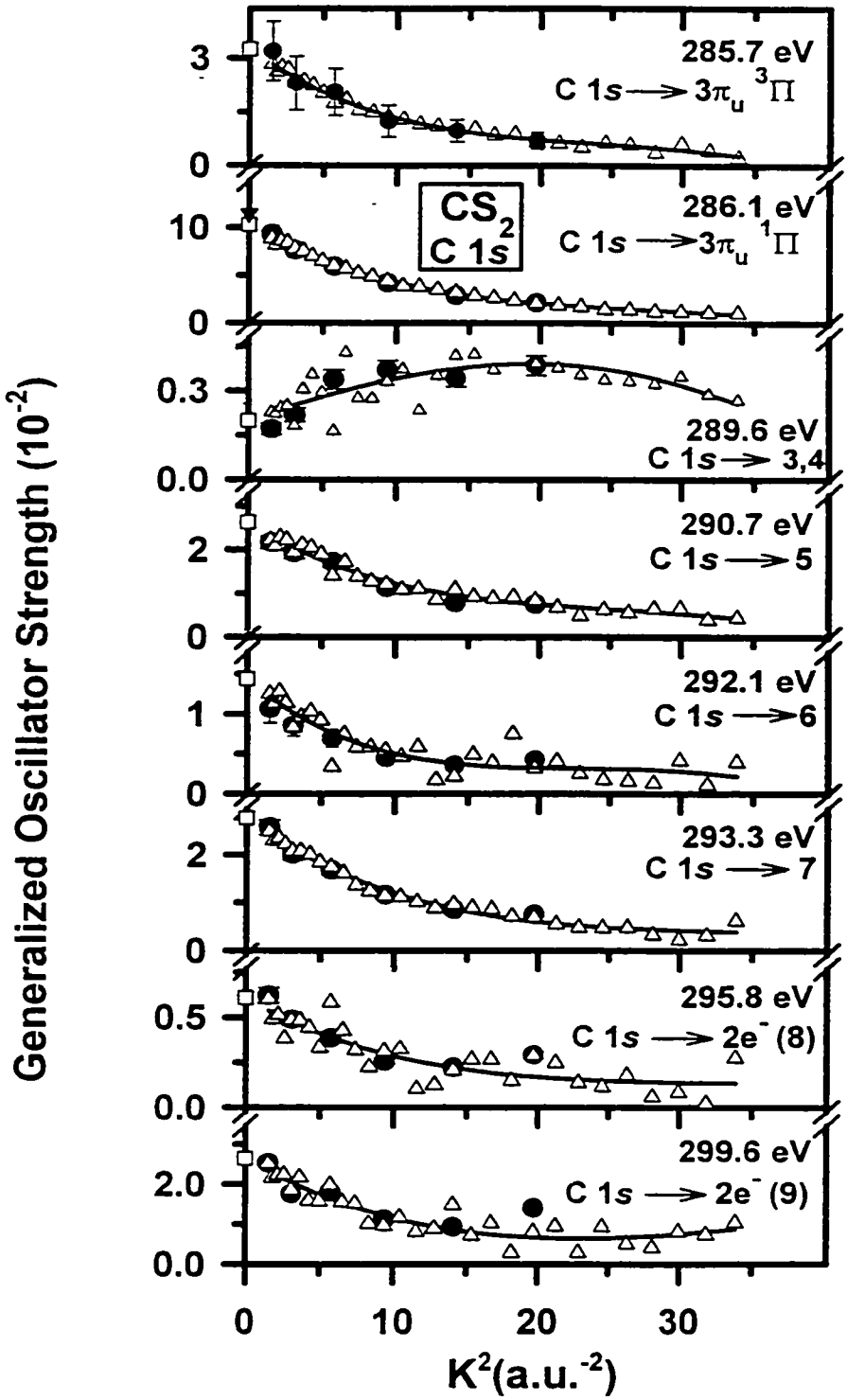

Fig. 7.7 GOS profiles for the C 1s transitions of CS_2 derived from angle dependent EELS spectra.

assignment of the 292.1 eV feature (peak 6) as a non-dipole transition would hold, there should be a curve that increases with the momentum transfer, much like what we see for peak 3,4. Since this is not the case, the non-dipole character for this transition is not confirmed by its GOS profile.

For all features, Lassettre fits [L65, DL75] are also plotted. The Lassettre parameters are summarized in **Table 7.6**. For each state, the signs of the coefficients are those expected for dipole excitations, except for the transition at 289.6 eV, which clearly shows a dipole forbidden character.

7.3.1.2. S 2*p* GOS profiles

Figure 7.8 presents the GOS profiles for all resolved features in the S 2*p* spectrum of CS_2. The absolute GOS scale for the S 2*p* region was set by matching the graphical extrapolation to $K^2 = 0$ of the relative GOS profile for the S $(2p)^{-1} \rightarrow 3\pi_u^*$ feature at 163.1 eV to the value taken as 0.0085 [MHB&89].

The GOS for all S 2*p* transitions decay relatively smoothly to higher K^2 from a maximum at $K^2 = 0$, indicating a dominant dipole-allowed process in all of them. However, the decay is less for the first two curves, which in fact show a maximum around 4 a.u.$^{-2}$. This agrees with the observation from the insert of fig. 7.3 that shows that the intensity of the first two features increase significantly with increasing momentum transfer, suggesting there is a mixture of states, some of which may be dipole forbidden. This is not surprising as the S 2*p* levels in CS_2 are of π_u, π_g, σ_g symmetry and the final orbital is of

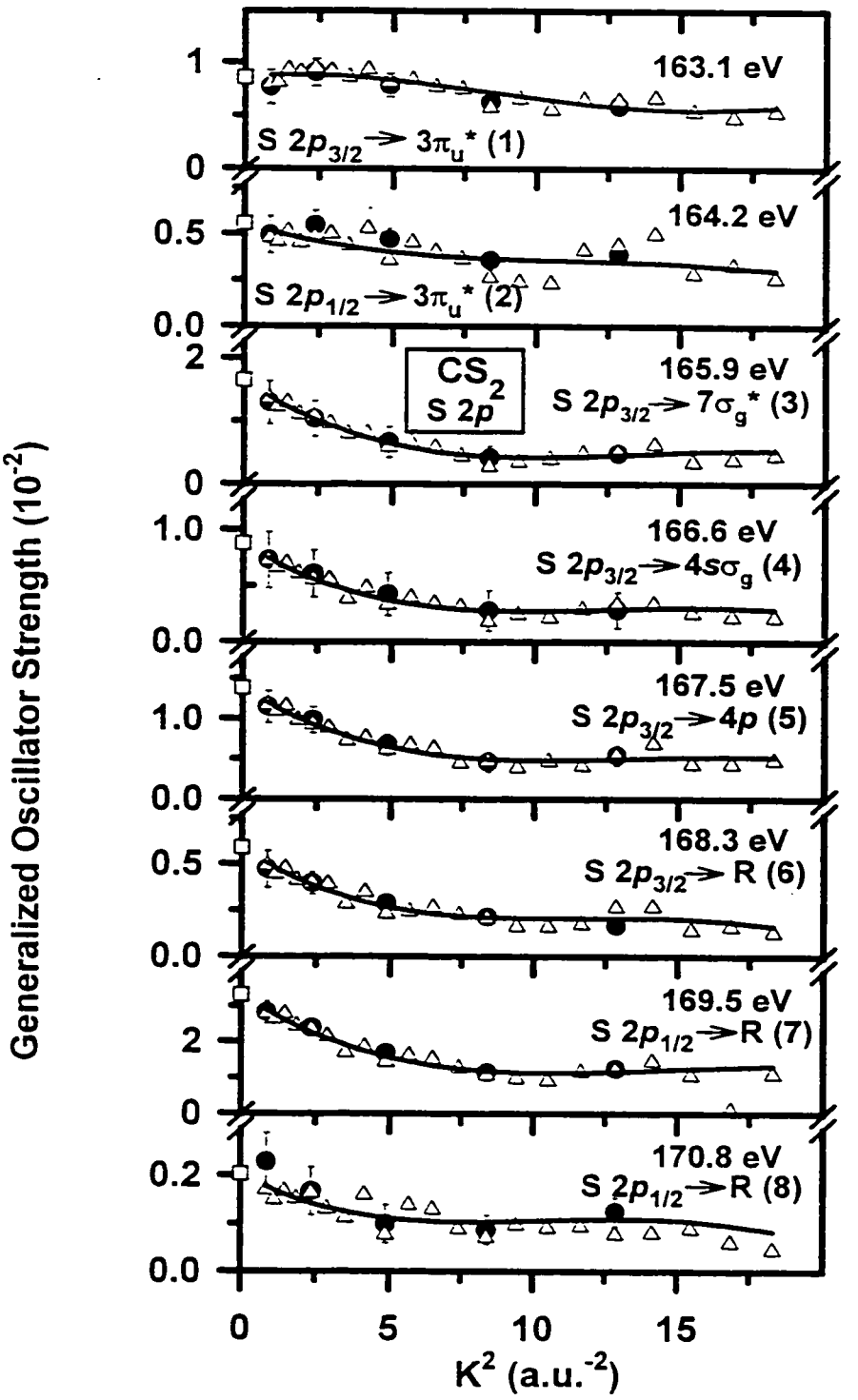

Fig. 7.8 GOS profiles for the S 2*p* transitions of CS_2 derived from angles dependent EELS spectra.

Table 7.6 Values of the Lassettre coefficients derived from fits to the GOS profiles for CS_2.

		f_0 x 10^{-2}	f_1	f_2 x 10	f_3 x 10^2	f_1/f_0 x 10	f_2/f_0 x 10^3	f_3/f_0 x 10^4
C 1*s*	$3\pi_u{}^{*3}\Pi$	3.3	-2.2	6.9	-8.0	-6.8	2.1	-2.5
	$3\pi_u{}^{*1}\Pi$	10.3	-62	17	-17	-6.2	1.7	-1.7
	"3,4"	0.2	0.1	-0.01	0.5	6.8	-0.05	2.5
	"5"	2.6	-1.4	3.7	-3.6	-5.2	1.4	-1.4
	"6"	1.4	-1.0	3.0	-3.0	-6.8	2.1	-2.1
	"7"	2.8	-1.3	2.4	-1.6	-4.5	0.9	-0.6
	"8"	0.6	-0.3	0.7	-0.5	-4.9	1.1	-0.9
	"9"	2.6	-1.5	3.6	-1.9	-5.7	1.3	-0.7
S 2*p*	$3\pi_u$*	1.1	0.3	-2.6	4.8	2.6	-2.5	4.5
	$3\pi_u$*	0.6	-0.2	0.9	-1.3	-3.7	1.6	-2.4
	$7\sigma_g$*	1.6	-1.4	5.1	-5.7	-8.4	3.1	-3.4
	4*s*	0.9	-0.7	2.7	-2.2	-7.9	3.1	-3.6
	4*p*	1.4	-0.9	3.3	-3.6	-6.8	2.4	-2.6
	R	0.6	-0.4	1.6	-1.9	-7.0	2.6	-3.2
	R	3.3	-1.9	5.4	-4.5	-5.6	1.6	-1.4
	R	0.2	-0.1	0.5	-0.7	-6.1	2.7	-3.4

π_u symmetry. According to the symmetry selection rules, it is possible to have a dipole forbidden transition increasing its intensity at higher momentum transfer.

For all features, Lassettre fits [L65, DL75] are also plotted. The Lassettre parameters are summarized in Table 7.6.

7.3.2. Carbonyl Sulfide (COS)

7.3.1.1. C 1*s* GOS profiles

GOS profiles, up to K^2 = 30 a.u.$^{-2}$ were derived for all resolved C 1*s* spectral features. They are presented in **Figure 7.9**. The relative GOS profiles were converted to absolute GOS profiles using a scaling factor obtained by exponential extrapolation of the relative GOS to K^2 = 0 followed by normalization of that extrapolated value to the literature optical oscillator strength (OOS) for the strong C 1*s* $\rightarrow 4\pi_u^*$ (taken as 0.01(3)) [MHB&89]. The scaling factor for the π^* OOS was used to derive the absolute GOS from the relative GOS for all other features. There is good agreement between the GOS curves derived from spectra acquired using **energy-scan** and **angle-scan** modes.

All GOS profiles are decaying from a maximum value at K^2 = 0, with the exception of the C 1*s* $\rightarrow 10\sigma^*$ for both the singlet and triplet states that show a clear dipole-forbidden shape.

For all features, Lassettre fits [L65, DL75] are also plotted. The Lassettre coefficients are summarized in **Table 7.7**.

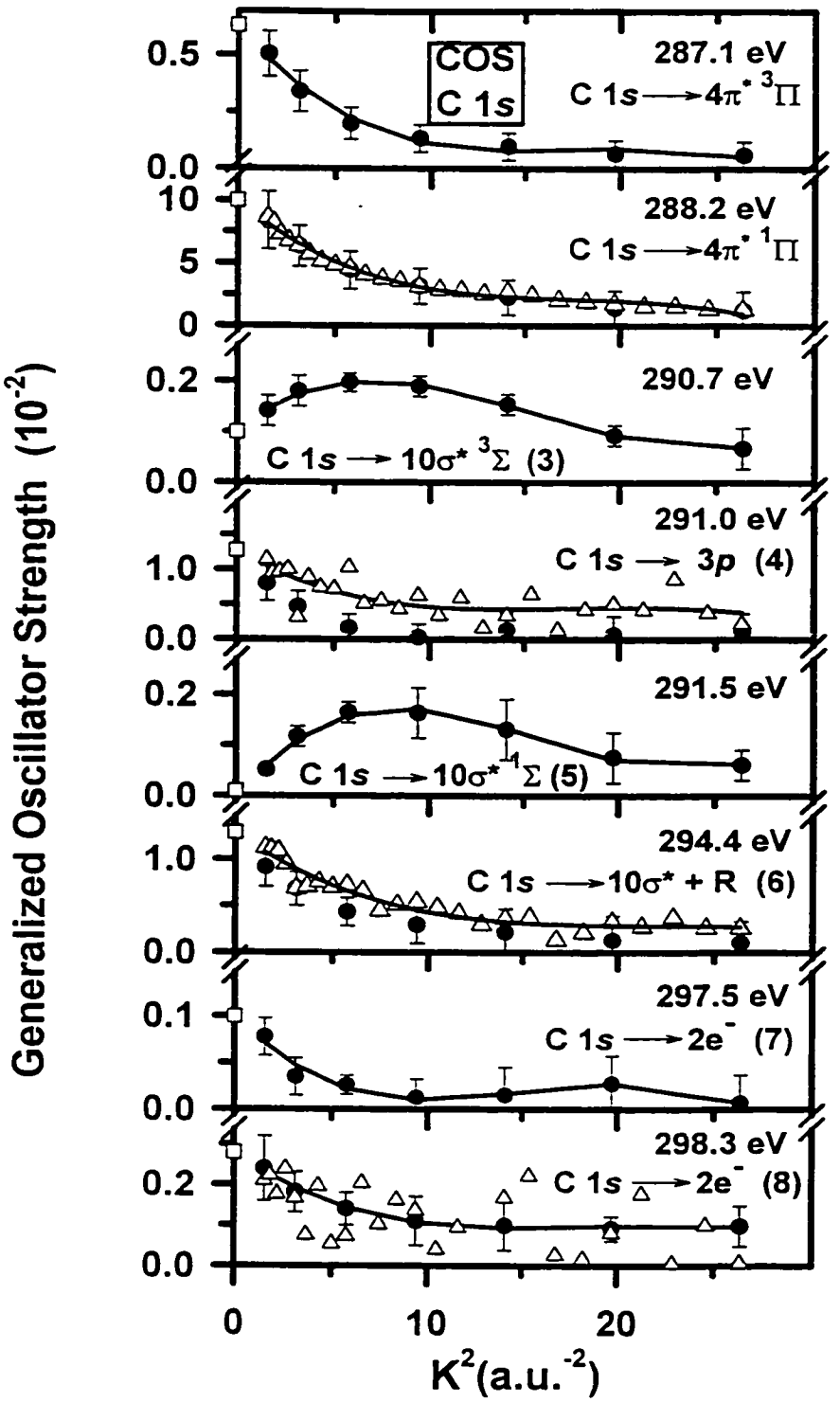

Fig. 7.9 GOS profiles for the C 1s transitions of COS derived from angles dependent EELS spectra.

Table 7.7. Values of the Lassettre coefficients derived from fits to the GOS profiles for COS.

		f_0 x 10^{-2}	f_1	f_2 x10	f_3 x10^2	f_1/f_0 x10	f_2/f_0 x10^3	f_3/f_0 x10^4
C 1*s*	$4\pi^*{}^3\Pi$	0.6	-0.8	3.9	-6.0	-13	6.2	-9.5
	$4\pi^*{}^1\Pi$	10.01	-10	46	-71	-10	4.6	-7.1
	$10\sigma^*\ {}^3\Sigma$	0.1	0.2	-1.5	2.4	-23	-15	23
	$10\sigma^*\ {}^1\Sigma$	1.3	-1.2	5.5	-8.0	-9.2	4.3	-6.3
	3*p*	0.01	0.4	-2.2	3.4	314	-182	281
	$10\sigma^*$+R	1.3	-0.9	2.9	-3.1	-7.1	2.3	-2.4
	2e	0.1	-0.2	0.9	-1.4	-15	8.3	-13
	2e	0.3	-0.2	1.0	-1.3	-8.4	3.6	-4.6
S 2*p*	$4\pi^*$	1.1	-0.3	0.6	-0.5	-3.4	0.5	-0.4
	$4\pi^*/10\sigma^*$	2.1	-1.2	3.0	-2.3	-5.7	1.4	-1.1
	$4s/10\sigma^*$	1.5	-1.1	4.5	-5.8	-7.4	2.9	-3.8
	R	1.7	-0.7	1.0	-0.2	-4.1	0.6	-0.1
	R	1.5	-0.7	1.3	-0.7	-4.8	0.9	-0.4

7.3.1.2. S 2*p* GOS profiles

Generalized oscillator strength profiles are shown for all S 2*p* resolved transitions of COS in **Figure 7.10**. The absolute GOS scale for the S 2*p* region was set by matching the graphical extrapolation to $K^2 = 0$ of the relative GOS profile for the S $(2p)^{-1} \rightarrow 4\pi_u^*$ feature at 164.2 eV to 0.011 [MHB&89].

The GOS for all transitions decay relatively smoothly to higher K^2 from a maximum at $K^2 = 0$, indicating a dominant dipole-allowed process in all of them. For all features, Lassettre fits [L65, DL75] are also plotted. The Lassettre parameters are summarized in Table 7.7.

7.3.1.3. O 1*s* GOS profiles

Generalized oscillator strength profiles are shown for all O 1*s* resolved transitions of COS in **Figure 7.11**. The absolute GOS scale for the O 1*s* region was set by matching the graphical extrapolation to $K^2 = 0$ of the relative GOS profile for the O $(1s)^{-1} \rightarrow 4\ \pi_u^*$ feature at 533.7 eV to 0.052 [MHB&89]. Analogous to the C 1*s* and S 2*p* GOS profiles, the agreement between the sets of results obtained from both, the **energy scan** and **angle scan**, acquisition modes is good. The GOS for all transitions decay relatively smoothly to higher K^2 from a maximum at $K^2 = 0$, indicating a dominant dipole-allowed process in all of them. For all features, Lassettre fits [L65, DL75] are also plotted.

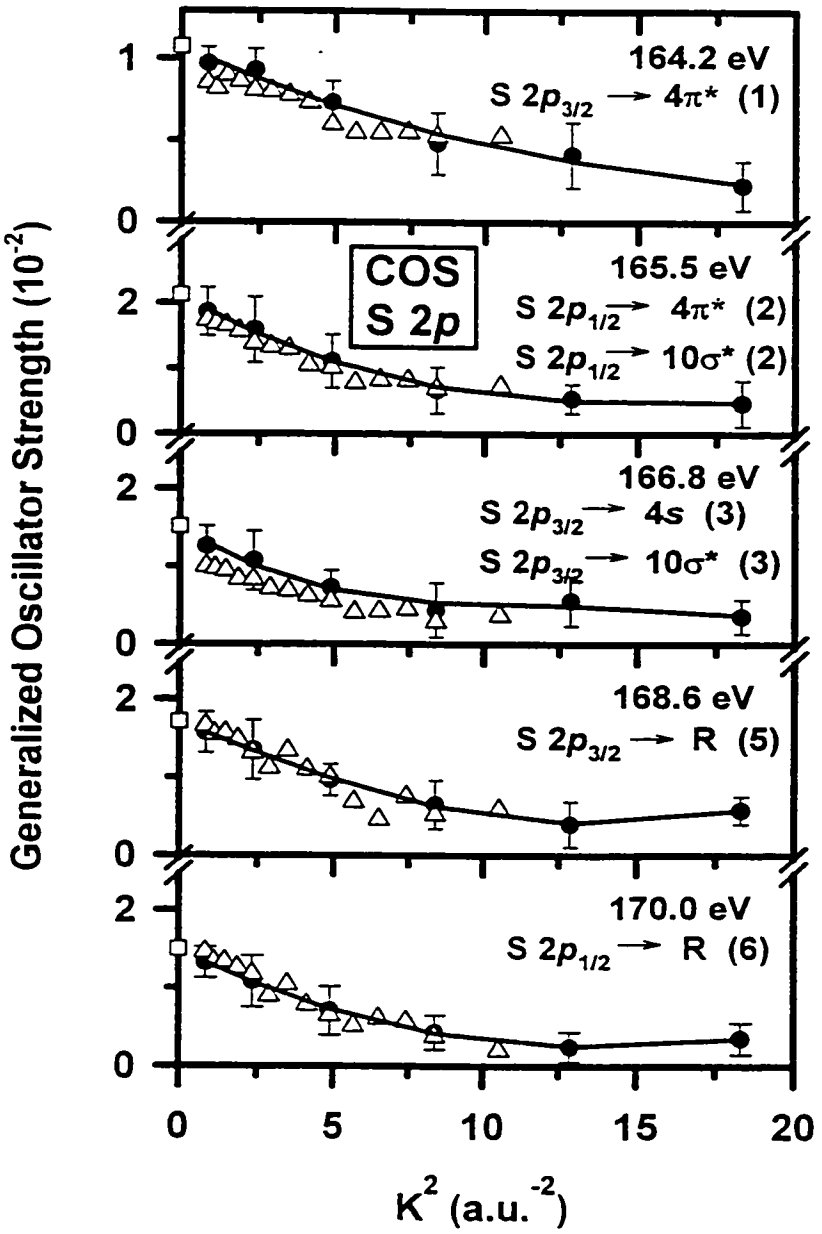

Fig. 7.10 GOS profiles for the S 2*p* transitions of COS derived from angles dependent EELS spectra.

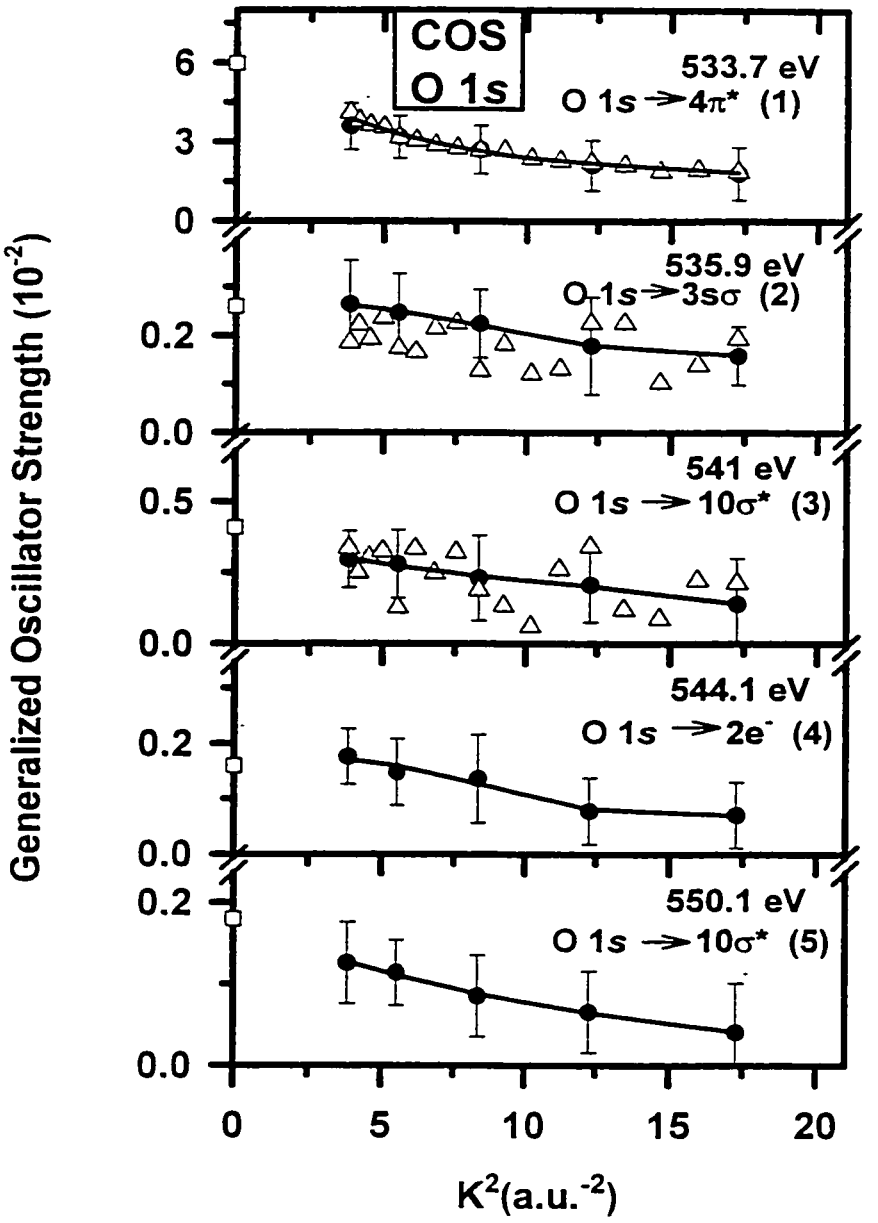

Fig. 7.11 GOS profiles for the O 1*s* transitions of COS derived from angles dependent EELS spectra.

7.4. Summary

Energy loss spectra of CS_2 and COS recorded under dipole and strongly non-dipole conditions in the region of S $2p$, C $1s$ and O $1s$ excitation have been obtained. For the first time absolute experimental GOS curves have been derived for all resolved C $1s$ and S $2p$ features in CS_2 and C $1s$, S $2p$ and O $1s$ features in COS over an extended range of transferred momentum.

Chapter 8

CONCLUSIONS

This thesis has presented extensive results dealing with the measurement and interpretation of inner-shell electron energy loss spectra and generalized oscillator strengths at high momentum transfer. This chapter summarizes the rest of the thesis and provides suggestions for future work.

After an introduction to the theory of energy loss spectroscopy as applied to inner-shell excitation studies, the spectrometer that was used for all measurements presented here was examined in detail. Two experimental setups were presented. The original one used the monochromator. The configuration used for GOS determination does not use the monochromator. It is described in detail as significant changes were made relative to the monochromated design in order to achieve the higher signal rates needed for systematic studies at higher scattering angles. These changes included: a differential pumping system, a gas cell, a different electron gun, re-mounting of the monochromator, mounting the unmonochromated gun, and an improved rotation mechanism. A detailed description was presented of the experimental operating

procedures and the algorithm used to convert the recorded spectral data into absolute generalized oscillator strength profiles. Step-by-step examples were provided.

Chapter 5 presented the inner-shell electron energy-loss spectroscopy of SF_6 at very high momentum transfer together with the GOS for all inner-shell excited states. A non-dipole excitation at 181 eV was observed to become the dominant S $2p$ spectral feature in EELS spectra recorded at large momentum transfer ($K^2 \sim 113$ a.u.$^{-2}$). A variable impact energy, fixed-K study showed that the first Born approximation breaks down under low impact energy conditions ($E_o < 700$ eV). The generalized oscillator strength (GOS) profiles for S $2p$, S $2s$ and F $1s$ excitation of SF_6 up to very high momentum transfer were presented. The GOS profiles for F $1s$ were reported for the first time. A paper describing the instrumentation and the results on SF_6 has been accepted for publication in Chemical Physics [EFT&99].

Chapter 6 presented the results of a combined experimental and theoretical study of C $1s$ and O $1s$ excitation in CO_2. Electron energy loss spectra were recorded over a wide range of momentum transfer values (K^2 up to 70 a.u.$^{-2}$). The dipole forbidden C $1s \rightarrow \sigma_g^*$ transition was detected for the first time. The GOS profiles for all resolved C $1s$ and O $1s$ transitions were determined. The experimentally derived GOS profiles for the discrete C 1s and O 1s excitations were compared to the theoretical GOS profiles computed using high level *ab initio* methods by Alexandre Rocha and Carlos Bielschowsky (Universidade Federal do Rio de Janeiro). Overall, there was good agreement between the experimental and theoretical results indicating that the first Born approximation holds to a surprisingly large momentum transfer for the core excitations

studied. A paper describing the experimental and theoretical results on CO_2 has been accepted for publication in Physical Review A [ETH&99].

Chapter 7 presented the complementary results for the related molecules CS_2 and COS. There are relatively few studies of these common triatomic species and there are discrepancies in the literature, in particular for positions of the core $\rightarrow \sigma^*$ excitations. The GOS profiles for all edges of all resolved features were determined for the first time. A more complete interpretation of these results is under development. Theoretical calculations provided by the group in Rio de Janeiro will be made in the following months and a joint publication will be prepared.

There are a number of original contributions to the knowledge of mankind made by my thesis. First, it has produced a large number of high quality GOS profiles up to very large momentum transfer values, for high symmetry small molecules which are considered benchmarks for spectroscopic studies. My results roughly double the number of inner-shell GOS profiles known to date in the literature. An effective theory-experiment partnership was established, one that will continue in the future. Finally, I made significant improvements to the McVAHRES spectrometer. These will allow a wide range of related measurements to be made in the future.

Currently, the spectrometer is being further improved by the addition of a resistive anode, position sensitive parallel detector (Quantar 3300). The first studies with this system, indicate there is an ~40-fold enhancement in signal rates over the single channel detection that was used for the work reported in this thesis. This improved detection efficiency will enhance the capabilities of the spectrometer. It will allow use of

the monochromated configuration for high energy resolution studies of inner shell excitation at large momentum transfer, a regime which, until now, has been inaccessible on account of the very low signal rates (often < 1 cps with serial detection). A whole new generation of measurements are now possible. These could include:

- derivation of the GOS profiles for various highly symmetric molecules (e.g., hydrogen cyanide HCN, cyanogen C_2N_2, or formaldehyde H_2CO)
- extending GOS profile determinations to even higher values of momentum transfer. For example, although a heroic study was made at 62° to show the extremely large changes that occur in the S 2*p* edge of SF_6 I was only able to measure systematically out to 40°. The parallel detector will allow measurements at all experimental geometries accessible mechanically and electronically.
- investigating the dipole forbidden N 1*s* ($\sigma_g \rightarrow \pi_g^*$) transition in N_2. The GOS profile for the N 1*s* $\rightarrow \pi^*$ signal of N_2 has been studied experimentally (CFP&87, BIB93) and theoretically (RP85, BNH92) but only at low energy resolution. The theory - experiment comparison suggests indirectly there is a rather significant contribution from the dipole forbidden N 1*s* ($\sigma_g \rightarrow \pi_g$) transition, which in fact parallels our observations for O 1*s* $\rightarrow \pi_g^*$ excitation in CO_2. If the N_2 study could be repeated at < 100 meV energy resolution it may be possible to see signals from the (N 1*s* σ_u^{-1},π_u) $^1\Pi_g$ quadrupole state directly. A better understanding of this system would answer questions concerning core hole localization, a subject of considerable importance in the field of inner-shell spectroscopy.

Another future development on the instrumental side would be to extend the impact energy capabilities of the spectrometer to higher energy. This would be very useful to expand the range over which one could test for break down of the first Born approximation. Impact energies up to 4 keV would also allow one to explore the experimental GOS of the O $1s \rightarrow \pi^*$ transition in CO_2, at low momentum transfer. Extending the GOS profile down to 1 $a.u^{-2}$ would allow one the see if the theoretically predicted GOS are correct. This is quite important since, from the experimental side, it appears there is only dipole allowed transitions, whereas the theoretical work suggests that, outside the low-K^2 region, there are roughly equal contributions from transitions to the dipole allowed (O $1s\ \sigma_g^{-1}$, π_u) and the quadrupole allowed (O $1s\ \sigma_u^{-1}$, π_u) states.

PUBLICATIONS of I.G. Eustatiu (as of March 2000)

1. F. Motte-Tollet, I. G. Eustatiu and D. Roy, *Resonant vibrational excitation of furan by low energy electron impact*, J. Chem. Phys., 105 (1996) 7448.

2. I. G. Eustatiu, B. Huo, S. G. Urquhart and A. P. Hitchcock, *Isomeric Sensitivity of the C 1s spectra of xylenes*, J. Electron Spectrosc., 94(1998) 243-252.

3. A. P. Hitchcock, I. G. Eustatiu, J. T. Francis and C. C. Turci, *Electron Impact Core excitation of molecules: Non-dipole spectroscopy and generalized oscillator strengths*, J. Electron Spectrosc., 88-91 (1998) 77-82.

4. I. G. Eustatiu, T. Tyliszczak and A. P. Hitchcock, *Inner-shell electron energy-loss spectroscopy of SF_6 at very high momentum transfer*, Chem. Phys. Lett., 300 (1999) 676-680.

5. I. G. Eustatiu, J. T. Francis, T. Tyliszczak, C. C. Turci, A. L. D. Kilcoyne and A. P. Hitchcock, *A high-performance electron energy loss spectrometer: generalized oscillator strengths for inner-shell excitation of SF_6* , Chem. Phys. (2000) (accepted Mar-00)

6. I. G. Eustatiu, T. Tyliszczak, A. P. Hitchcock, C. C. Turci, A. B. Rocha and C. E. Bielschowsky, *Experimental and theoretical study of generalized oscillator strengths for C 1s and O 1s excitation in CO_2*, Physical Review A (accepted Dec-99)

Appendix

SOFTWARE USED

1. McVSpec

McVSpec is a DOS-based data acquisition program, written in FORTRAN, used to acquire the data presented in this thesis.

2. BAN

BAN is a general purpose data analysis program produced and distributed by Tolek Tyliszczak (McMaster University, tel. 905-525-9140, ext. 24864). It is used in all raw data processing, like spectra calibration and background subtraction.

3. BGAUSS

BGAUSS is a line-shape and edge-shape fitting program, also written by Tolek Tyliszczak. It is used to first perform the fitting on a low angle energy spectrum and to establish the fit model to be used later when all energy and angle spectra are combined.

4. MGAUSS

MGAUSS is a multiple file line-shape and edge-shape fitting program created by Tolek Tyliszczak. It is similar to BGAUSS with the difference that it allows to fit up to

50 files with up to 500 parameters simultaneously, using a common fit parameters file. The input file is created using BGAUSS, then adapted to include all spectra that are needed to be fit together. The output file provides the area of all considered features.

5. Microsoft Excel 97

The spreadsheet program (by Microsoft) was used to organize the data by file names, apply all the geometrical and kinematic corrections and record the Lassettre coefficients. Each Excel file used for GOS purposes represents the electronic version of the data analysis book.

5. Sigma Plot 4.0

Sigma Plot 4.0 (by Jandel Scientific) was used in all graphical representations.

6. IDL 5.2.

IDL 5.2 (by Research System Inc.) was used for fig. 4.2.

References

[AGA&72] C. J. Allan, U. Gelius, D. A. Allison, G. Johansson, H. Siegbahn and K. Siegbahn, *J. Electron Spectrosc.*, 1 (1972/73) 131.

[AKS&95] J. Adachi, N. Kosugi, E. Shigemasa and A. Yagishita, *J. Chem. Phys.*, 102 (1995) 7369.

[AM73] L. H. Auer and D. Mihalas, *Astrophys. J.*, 184 (1973) 151.

[ATH&92] P. Aebi, T. Tyliszczak, A. P. Hitchcock, K. M. Baines, T. K. Sham, T. E. Jackman, J.-M. Baribeau and D. J. Lockwood, *Phys. Rev. B*, 45 (1992) 13579.

[B30] H. Bethe, *Ann. Physik (Leipzig)*, 5 (1930) 325.

[B79] R. A. Bonham, in *Electron Spectroscopy: Theory, Techniques and Applications*, vol. 3, Academic Press, 1979.

[BB92] R. S. Barbieri and R. A. Bonham, *Phys. Rev. A*, 45 (1992) 7929.

[BBS91] H. M. Boechat Roberty, C. E. Bielschowsky and G. G. B. de Souza, *Phys. Rev. A*, 44 (1991) 1694.

[BGH62] H. Boersch, J. Geiger and H. Hellwich, *Phys. Lett.*, 3 (1962) 64.

[BGR68] H. Boersch, J. Geiger and H. J. Reich, *Z. Phys.*, 161 (1968) 296.

[BH81] C. E. Brion, A. Hamnett, *Adv. Chem. Phys.*, 45 (1981) 1.

[BHK&72] D. Blechschmidt, R. Haensel, E. E. Koch, U. Nielsen and T. Sagawa, *Chem. Phys. Lett.*,14 (1972) 33.

[BIB93] R. A. Bonham, M. Inokuti and R. S. Barbieri, *J. Phys. B*, 26 (1993) 3363.

[BNH92] C. E. Bielschowsky, M. A. C. Nascimento and E. Hollauer, *Phys. Rev. A*, 45 (1992) 7942.

[BSS95] J. D. Bozek, N. Saito and I. H. Suzuki, *Phys. Rev. A*, 40 (1995) 4563.

[BT81] R. T. Brinkmann and S. Trajmar, J. Phys. E, 14 (1981) 245.

[C71] F. A. Cotton, *Chemical Applications of Group Theory* (Interscience, New York, 1971).

[C71a] L. G. Christophorou, *Atomic and Molecular Radiation Physics* (Wiley-Interscience, London, 1971).

[CCB91] W. F. Chan, G. Cooper and C. E. Brion, *Phys. Rev A*, 44 (1991) 186.

[CCG&92] W. F. Chan, G. Cooper, X. Guo and C. E. Brion, *Phys. Rev A*, 45 (1992) 1420; W. F. Chan, G. Cooper, X. Guo, G. R. Burton and C. E. Brion, *Phys. Rev A*, 46 (1992) 149.

[CFP&87] R. Camilloni, E. Fainelli, G. Petrocelli and G. Stefani, *J. Phys. B.: At. Mol. Phys.*, 20 (1987) 1839.

[CLL75] S. Chung, C. C. Lin and E. T. P. Lee, *Phys. Rev. A*, 12 (1975) 1340.

[CNK74] D. di Chio, S. V. Natali and C. E. Kuyatt, *Rev. Sci. Inst.*, 45 (1974) 559.

[D72] J. L. Dehmer, *J. Chem. Phys.*, 56 (1972) 4496.

[D76] J. L. Dehmer, *J. Chem. Phys.*, 65 (1976) 5327.

[DD75] J. L. Dehmer, D. Dill, *Phys. Rev. Lett.*, 35 (1975) 213.

[DD76] J. L. Dehmer, D. Dill, *J. Chem. Phys.* 65 (1976) 5327.

[DDH82] W. R. Daasch, E. R. Davidson and A. U. Hazi, *J. Chem. Phys.*, 76 (1982) 6031.

[DL75] M. A. Dillon and E. N. Lassettre, *J. Chem. Phys.*, 62 (1975) 2373.

[DPS87] J. L. Dehmer, A. C. Parr and S. H. Southworth, *Handbook on Synchrotron Radiation*, edited by G. V. Marr (North-Holland, Amsterdam, 1987), Vol. 2, Chap. 5.

[DTH90] C. Dezarnaud, M. Tronc and A. P. Hitchcock, *Chem. Phys.*, 142 (1990) 455.

[E90] R. C. Elton, *X-ray Lasers* (Academic Press, Orlando, 1990).

[EFT&99] I. G. Eustatiu, J. T. Francis, T. Tyliszczak, C. C. Turci, A. L. D. Kilcoyne and A. P. Hitchcock, *Chem. Phys.*, (2000) in press (accepted March 2000).

[EHU&98] I. G. Eustatiu, B. Huo, S. G. Urquhart and A. P. Hitchcock, *J. Electron Spectrosc.*, 94 (1998) 243.

[ETH99] I. G. Eustatiu, T. Tyliszczak and A. P. Hitchcock, *Chem. Phys. Lett.*, 300 (1999) 676.

[ETH&99] I. G. Eustatiu, T. Tyliszczak, A. P. Hitchcock, C. C. Turci, A. B. Rocha and C. E. Bielschowsky, *Phys. Rev. A*, (2000) in press (accepted December 1999).

[ETH&00] I. G. Eustatiu, C. C. Turci, T. Tyliszczak and A. P. Hitchcock, in preparation

[F54] U. Fano, *Phys. Rev.*, 95 (1954) 1198.

[F95] J. T. Francis, *Non-Dipole and Dipole Electron Energy Loss Spectroscopy*, Ph. D. Thesis, McMaster University, 1995.

[FCM96] I. W. Fomunung, Z. Chen and A. Z. Msezane, *Phys. Rev. A*, 53 (1996) 441.

[FEL&94] J. T. Francis, C. Enkvist, S. Lunell and A. P. Hitchcock, *Can. J. Phys.*, 72 (1994) 879.

[FH14] J. Franck, G. Hertz, Verh. *Dtsch. Phys. Ges.*, 16 (1914) 10.

[FKH94] J. T. Francis, N. Kosugi and A. P. Hitchcock, *J. Chem. Phys.*, 101 (1994) 10429.

[FLK84] J. -H Fock, H. -J. Lau and E. E. Koch, *Chem. Phys.*, 83 (1984) 377.

[FTT&95] J. T. Francis, C. C. Turci, T. Tyliszczak, G. G. B. de Souza, N. Kosugi and A. P. Hitchcock, *Phys. Rev. A*, 52 (1995) 4665.

[GGL72] F. A. Gianturco, C. Guidotti and U. Lamanna, *J. Chem. Phys.*, 57 (1972) 840.

[GGS&98] K. Gunnelin, P. Glans, P. Skytt, J.-H. Guo, J. Nordgren and H. Ågren, *Phys. Rev. A*, 57 (1998) 864.

[H71] D. W. O. Heddle, *J. Phys. E.*, 4 (1971) 589.

[H71a] R. D. Hudson, *Reviews of Geophys. and Space Physics*, 9 (1971) 305.

[H78] A. P. Hitchcock, *Molecular Inner Shell Excitation Studied by Electron Impact*, Ph. D. Thesis, University of British Columbia, 1978.

[H79] W. M. Huo, *J. Chem. Phys.*, 71 (1979) 1593.

[H86] I. Harrison, Ph. D. thesis, University of Manchester, 1986.

[H87] R. G. Hayes, *J. Chem. Phys.*, 86 (1987) 1683.

[H90] A. P. Hitchcock, *Phys. Scripta*, T31 (1990) 159.

[HAK&84] S. Huzinaga, J. Andzelm, M. Klobukowski, E. Radzio-Andzelm, Y. Sakai, H. Tatewaki, *Gaussian Basis Sets for Molecular Calculation*, Physical Sciences Data, Vol.16 (Elsevier, Amsterdam, 1984).

[HB78] A. P. Hitchcock and C. E. Brion, *Chem. Phys.*, 33 (1978) 55.

[HBV78] A. P. Hitchcock, C. E. Brion and M. J. Van der Wiel, *J. Phys. B.*, 11 (1978) 3245.

[HEF&98] A. P. Hitchcock, I. G. Eustatiu, J. T. Francis and C. C. Turci, *J. Electron Spectrosc.*, 88 (1998) 77.

[HHS86] A. P. Hitchcock, J. A. Horsley and J. Stöhr, *J. Chem. Phys.*, 85 (1986) 4835.

[HK86] I. Harrison and G. C. King, *J. Phys. B.*, 19 (1986) L447.

[HK87] I. Harrison and G. C. King, *J. Electron Spectrosc.*, 43 (1987) 155.

[HM94] A. P. Hitchcock and D. C. Mancini, *J. Electron Spectrosc.*, 67 (1994) 433. (updates available)

[HR68] I. V. Hertel and K. L. Ross, *J. Phys. B*, 1 (1968) 697.

[HR69] I. V. Hertel and K. L. Ross, *J. Phys. B*, 2 (1969) 285.

[HR75] E. Harting and F. H. Read, *Electrostatic Lenses* (Elsevier Scientific, Amsterdam, 1975).

[HS87] A P. Hitchcock and J. Stöhr, *J. Chem. Phys.*, 87 (1987) 3255.

[HSD&93] E. Hudson, D. A. Shirley, M. Domke, G. Remmers, A. Puschmann, T. Mandel, C. Xue and G. Kaindl, *Phys. Rev. A*, 47 (1993) 316.

[I71] M. Inokuti, *Rev. Mod. Phys.*, 43 (1971) 297.

[IIT71] M. Inokuti, Y. Itikawa, J. Turner, *J. Rev. Mod. Phys.*, 43 (1971) 176.

[IIT78] M. Inokuti, Y. Itikawa, J. Turner, *Rev. Mod. Phys.*, 50 (1978) 23.

[ILMH&87] I. Ishii, R. McLaren, A. P. Hitchcock, M. B. Robin, *J. Phys. Chem.*, 87 (1987) 4344.

[JBE84] W. L. Jolly, K. D. Bomben and C. J. Eyermann, *At. Data Nucl. Data Tables*, 31 (1984) 7.

[JS73] W. L. Jorgensen, L. Salem, *The Organic Chemist's Book of Orbitals* (Academic, New York 1973).

[K68] C. E. Kuyatt in B. Bederson and W. L. Fite (editors), *Methods of Experimental Physics*, 7A (1968) 1, Academic Press, New York, 1968.

[K72] Y.-K. Kim, *Phys. Rev. A*, 6 (1972) 666.

[K85] S. F. A. Kettle, *Symmetry and Structure* (Wiley, New York, 1985).

[K96] N. Kosugi, *J. Electron Spectrosc.*, 79 (1996) 351.

[KEH&98] A. Karawajczyk, P. Erman, P. Hatherly, E. Rachlew, M. Stankiewicz and Y. Franzen, *Phys. Rev. A*, 58 (1998) 314.

[KGM77] A. A. Krasnoperova, E. S. Gluskin and L. N. Mazalov, *Zhurnal Strukturnoi Khimii*, 18 (1977) 255.

[KI68] Y. K. Kim and M. Inokuti, *Phys. Rev.*, 175 (1968) 176.

[KM69] M. Krauss and S. R. Mielczarek, *J. Chem. Phys.*, 51 (1969), 5241.

[L59] E. N. Lassettre, *Rad. Res. (Supp.)*, 1 (1959) 530.

[L65] E. N. Lassettre, *J. Chem. Phys.*, 43 (1965) 4479.

[L74] E. N. Lassettre, in *Chemical Spectroscopy and Photochemistry in the Vacuum Ultraviolet*, eds. C. Sandorfy, P. J. Ausloos and M. B. Robin (Reidel, Boston, 1974).

[L77] J. S. Lee, *J. Chem. Phys.*, 67 (1977) 3998.

[LCS89] P. Letardi, R. Camilloni and G. Stefani, Phys. Rev. B., 40 (1989) 3311.

[LDW79] A. Lahmam-Bennani, A. Duguet and H. F. Wellenstein, *Chem. Phys. Lett.*, 60 (1979) 405.

[LDW&80] A. Lahmam-Bennani, A. Duguet, H. F. Wellenstein and M. Rouault, *J. Chem. Phys.*, 72 (1980) 6398.

[LKS64] E. N. Lassettre, M. E. Krasnow and S. Silverman, *J. Chem. Phys.*, 40 (1964) 1242.

[LM82] R. R. Luchese and V. McKoy, *Phys. Rev. A*, 26 (1982) 1406.

[LS74] E. N. Lassettre and A. Skerbele, *Meth. Exp. Phys.*, 3B (1974) 868.

[LSD69] E. N. Lassettre, A. Skerbele and M. Dillon, *J. Chem. Phys.*, 50 (1969) 1829.

[M75] K. J. Miller, *J. Chem. Phys.*, 62 (1975) 1759.

[MB93] M. P. de Miranda and C. E. Bielschowsky, *J. Mol. Struct. (Theochem)*, 282 (1993) 71.

[MBB&94] M. P. de Miranda, C. E. Bielschowsky, H. M. Boechat Roberty and G. G. B. de Souza, *Phys. Rev. A*, 49 (1994) 2399.

[MBN95] M. P. de Miranda, C. E. Bielschowsky, and M.A.C. Nascimento, *J. Phys. B*, 28 (1995) L15.

[MCI&87] R. McLaren, S. A. C. Clark, I. Ishii and A. P. Hitchcock, *Phys. Rev. A*, 36 (1987) 1683.

[MCM&91] Y. Ma, C. T. Chen, G. Meigs, K. Randall and F. Sette, *Phys. Rev. A*, 44, 1848 (1991).

[MHB&89] P. Millie, A. P. Hitchcock, S. Bodeur and I. Nenner, unpublished.

[MKT85] J. N. Murrell, S. F. A. Kettle, J. M. Tedder, *The Chemical Bond* (Wiley, New York, 1985).

[MMK69] K. J. Miller, S. R. Mielczarek and M. Krauss, *J. Chem. Phys.*, 51 (1969) 26.

[N70] V. I. Nefedov, *Zh. Strukt. Khim.*, 11 (1970) 292; *J. Struct. Chem.*, 11 (1970) 272.

[NHD&88] I. Nenner, M. J. Hubin-Franskin, J. Delwiche, P. Morin and S. Bodeur, J. of Molec. Struct., 173 (1988) 269.

[P60] L. Pauling, *The Nature of the Chemical Bond* (Cornell University Press, Ithaca, NY, 1960).

[PL84] R. C. C. Perera and E. Lavilla, *J. Chem. Phys.*, 81 (1984) 3375.

[PLF&87] M. N. Piancastelli, D. W. Lindle, T. A. Ferret and D. A. Shirley, *J. Chem. Phys.*, 87 (1987) 3255.

[RBB98] A. B. Rocha, I. Borges Jr. and C. E. Bielschowsky, *Phys. Rev.*, 57 (1998) 4394.

[RCI&74] F. H. Read, J. Comer, R. E. Imhof, J. N. H. Brunt and E. Harting, *J. Electron Spectrosc.*, 4 (1974) 293.

[RDK93] G. Remmers et al., *Phys. Rev. A*, 47 (1993) 3085.

[RDP&92] G. Remmers et al., *Phys. Rev. A*, 46 (1992) 3935.

[RO85] T. N. Rescigno and A. E. Orel., *Lect. Notes in Chem.*, 35 (1985) 215.

[S92] J. Stöhr, *NEXAFS Spectroscopy*, Springer Series in Surface Sciences, (Springer-Verlag, Heidelberg, 1992), Vol. 25.

[SAV&84] V. N. Sivkov, V. N. Akimov, A. S. Vinogradov and T. M. Zimkina, *Opt. Spectrosc. USSR*, 57 (1984) 160.

[SB76] W. H. E. Schwarz and R. J. Buenker, *Chem. Phys.*, 13 (1976) 153.

[SB84] R. N. S. Sodhi and C. E. Brion, *J. Electron Spectrosc.*, 34 (1984) 363.

[SB85] R. N. S. Sodhi and C. E. Brion, *J. Electron Spectrosc.*, 37 (1985) 125.

[SBT&88] K. H. Sze, C. E. Brion, M. Tronc, S. Bodeur and A. P. Hitchcock, *Chem. Phys.*, 121 (1988) 279.

[SCT73] R. W. Shaw Jr., T. X. Caroll and T. D. Thomas, *J. Am. Chem. Soc.*, 95 (1973) 5870.

[SKD70] E. N. Lassettre, A. Skerbele and M. A. Dillon, *J. Chem. Phys.*, 52 (1970) 2797.

[SKR&82] D. A. Shaw, G. C. King, F. H. Read and D. Cvejanovic, *J. Phys. B.*, 15 (1982) 1785.

[SL64] S. M. Silverman and E. N. Lassettre, *J. Chem. Phys.*, 40 (1964) 1265.

[SS88] A. C. A. de Souza and G. G. B. de Souza, *Phys. Rev. A*, 38 (1988) 4488.

[SSH84] F. Sette, J. Stöhr and A. P. Hitchcock, *J. Chem. Phys.*, 81 (1984) 4906.

[STR&93] J. Schirmer, A. B. Trofimov, K. J. Randall, J. Feldhaus, A. M. Bradshaw, Y. Ma, C. T. Chen and F. Sette, *Phys. Rev. A*, 47 (1993) 1136.

[SYK&89] T. K. Sham, B. X. Yang, J. Kirz and J. S. Tse, *Phys. Rev. A*, 40 (1989) 652.

[T83] W. Thiel, *J. Electron Spectrosc.*, 31 (1983) 151.

[TAP79] M. Tronc, R. Azria and R. Paineau, *J. Phys.*, (Paris) 40 (1979) L 323.

[TFT&95] C. C. Turci, J. T Francis, T. Tyliszczak, G. G. B. de Souza and A. P. Hitchcock, *Phys. Rev. A*, 52 (1995) 4678.

[TKR79] M. Tronc, G. C. King and F. H. Read, *J. Phys. B*, 12 (1979) 137.

[UOC&95] K. Ueda, M. Okunishi, H. Chiba, Y. Shimizu, K. Ohmori, Y. Sato, E. Shigemasa and N. Kosugi, *Chem. Phys. Lett.*, 236 (1995) 311.

[UT83] L. Ungier and T. D. Thomas, *Chem. Phys. Lett.*, 96 (1983) 247.

[V70] M. J. Van der Wiel, *Physica*, 49 (1970) 411.

[V71] M. J. Van der Wiel and G. Wiebes, *Physica*, 53 (1971) 225; M. J. Van der Wiel and G. Wiebes, *Physica*, 54 (1971) 411.

[YDM&93] J. F. Ying, T. A. Daniels, C. P. Mathers, H. Zhu and K. T. Leung, *J. Chem. Phys.*, 99 (1993) 3390.

[YK87] B. Yang and J. Kirz, J. Phys. Col., 47 (1987) C8-585.

[YL94] J. F. Ying and K. T Leung, *J. Chem. Phys.*, 100 (1994) 7120; J. F. Ying and K. T Leung, *J. Chem. Phys.*, 100 (1994) 1011; J. F. Ying and K. T

Leung, *J. Chem. Phys.*, 101 (1994) 8333; J. F. Ying and K. T Leung, *J. Chem. Phys.*, 101 (1994) 7311.

[YML93] J. F. Ying, C. P. Mathers and K. T. Leung, *Phys. Rev. A*, 47 (1993) R5.

[YML&93] J. F. Ying, C. P. Mathers, K. T. Leung, H. P. Pritchard, C. Winstead and V. McKoy, *Chem. Phys. Lett.*, 212 (1993) 289.

[YML94] J. F. Ying, C. P. Mathers and K. T. Leung, *Phys. Rev. A*, 101 (1994) 7311.

[WB74] G. R. Wight and C. E. Brion, *J. Electron Spectrosc.*, 4 (1974) 25; G. R. Wight and C. E. Brion, *J. Electron Spectrosc.*, 3 (1974) 191; G. R. Wight and C. E. Brion, *J. Electron Spectrosc.*, 4 (1974) 335.